UNIVERSITY OF SOUTHAMPTON

FACULTY OF ENGINEERING AND THE ENVIRONMENT

School of Engineering Sciences

Modelling and Simulation of All-Vanadium Redox Flow Batteries

by

Hassan Abdul-Zehra Abdul-Yima Al-Fetlawi

Thesis for the degree of Doctor of Philosophy

November 2010

Abstract

Properties and applications of all-vanadium redox flow batteries are discussed and a two-dimensional model is developed. The model, which is based on a comprehensive description of mass, charge, energy and momentum transport and conservation, is combined with a global kinetic model for reactions involving vanadium species. Gas evolving reactions are then incorporated into the modelling frame work. Bubble formation as a result of evolution at the negative/positive electrode is included in the model, taking into account the attendant reduction in the liquid volume and the transfer of momentum between the gas and liquid phases, using a modified multiphase-mixture approach. Comparisons to simulations with negligible gas evolution demonstrate the effect of gas evolution on the efficiency of the battery. The effects of reactant concentration, flow rate, applied current density and gas bubble diameter on gas evolution are investigated. Significant variations in the gas volume fraction and the bubble velocity are predicted, depending on the operating conditions. The construction of a cell and charge/discharge experiments are described. Numerical simulations are compared to experimental data for different vanadium concentrations and mean linear electrolyte flow rates, demonstrating good agreement. Numerical simulations demonstrate the effect of changes in the operating temperature on performance of the all-vanadium redox flow battery and the extent of oxygen evolution. It is shown that variations in the electrolyte flow rate and the magnitude of the applied current substantially alter the charge/discharge characteristics, the temperature rise and the distribution of temperature. The effects of heat losses on the charge/discharge behaviour and temperature distribution are investigated. Conditions for localised heating and membrane degradation are discussed.

Contents

List of Figures

List of Tables

DECLARATION OF AUTHORSHIP

I, HASSAN ABDUL-ZEHRA ABDUL-YIMA AL-FETLAWI declare that the thesis entitled:

MODELLING AND SIMULATION OF ALL-VANADIUM REDOX FLOW BATTERIES

and the work presented in the thesis are both my own, and have been generated by me as the result of my own original research. I confirm that:

- this work was done wholly or mainly while in candidature for a research degree at this University;
- where any part of this thesis has previously been submitted for a degree or any other qualification at this University or any other institution, this has been clearly stated;
- where I have consulted the published work of others, this is always clearly attributed;
- where I have quoted from the work of others, the source is always given. With the exception of such quotations, this thesis is entirely my own work;
- I have acknowledged all main sources of help;
- where the thesis is based on work done by myself jointly with others, I have made clear exactly what was done by others and what I have contributed myself;
- parts of this work have been published as:

  1. H. Al-Fetlawi, A.A. Shah, F.C. Walsh, "Non-Isothermal Modelling of the All-Vanadium Redox Flow Battery", *Electrochim. Acta*, vol. (55) issue (1) pp. 78−89 (2009).
  2. A.A. Shah, H. Al-Fetlawi, F.C. Walsh, "Dynamic Modelling of Hydrogen Evolution Effects in the All-vanadium Redox Flow Battery", *Electrochim. Acta*, vol. (55) issue (3) pp. 1125−1139 (2010).

3. H. Al-Fetlawi, A.A. Shah, F.C. Walsh, "Modelling the effects of Oxygen Evolution in the All-vanadium Redox Flow Battery", *Electrochim. Acta*, vol. (55) issue (9) pp. 3192−3205 (2010).

4. H. Al-Fetlawi, A.A. Shah, F.C. Walsh, "A Dynamic Modelling of the All-vanadium Redox Flow Battery", In, *The 217th ECS Meeting, Vancouver, Canada*, April 25−30, 2010, B3−00890.

5. H. Al-Fetlawi, A.A. Shah, F.C. Walsh, "Modelling All-Vanadium Redox Flow Battery", In, *61st Annual Meeting of the International Society of Electrochemistry,Nice, France*,September 26th - October 1st, 2010, s04−P-001.

6. R. Tangirala, M.J. Watt-Smith, H. Al-Fetlawi, P. Ridley, R.G.A. Wills, A.A. Shah, F.C. Walsh, " The effects of mass transfer on the performance of Vanadium Redox Flow Battery", *J. Electrochem. Soc.*, in preparation.

Signed:

Date:

Acknowledgement

I am indebted to Dr. Akeel Shah for suggesting the project, supervision, continuous guidance, his utmost efforts and interest throughout the work which contributed to its completion.

My respectful regards to Professor Frank Walsh for advising and providing the research facilities.

My deepest gratitude and regretful thanks to all my Friends for their help and encouragement.

I am thankful as well to my Family for their patience during my study.

Dedication

To
My Family

with
Deep Love

and
Affection

Nomenclature

Roman Symbol	Definition	Unit
A	Cross sectional area	m^2
a	Surface area	m^{-1}
C	Specific heat capacity at constant pressure	J kg^{-1} K^{-1}
C_D	Drag coefficient	Dimensionless
C_{dl}	Constant capacity	C V^{-1}
c	Concentration	mol m^{-3}
D	Diffusion coefficient	m^2 s^{-1}
d	Thickness	m
d_f	Mean pore diameter	m
d_g	Bubble diameter	m
E	Potential	V
E_{cell}	Cell voltage	V
E^{eq}	Equilibrium potential	V
E_0	Open circuit voltage	V
F	Faraday's constant	C mol^{-1}
h	Height	m
I	Current	A
j	Current density	A m^{-2}
K	Kozeny-Carman constant	Dimensionless
k	Reaction rate constants	m s^{-1}
k_m	Mass transport coefficient	m s^{-1}
L	Thickness/width	m
M	Molar mass	kg mol^{-1}
m	Amount of material	mol

N	Flux density	mol m^{-2} s^{-1}
Nu	Nusselt number	Dimensionless
n	Number of electrons	Dimensionless
$\vec{n}$	Unit outer normal	Dimensionless
p	Pressure	Pa
Q	Heat source	W m^{-3}
q	Amount of electrical charge	C
R	Molar gas constant	J mol^{-1} K^{-1}
Re	Reynolds number	Dimensionless
S	Source/sink flux term	mol m^{-3} s^{-1}
T	Temperature	K
t	Time	s
U	Mobility	m^2 mol J^{-1} s^{-1}
u	The x component of the velocity	m s^{-1}
$\vec{u}$	Phase velocity	m s^{-1}
V	Volume	m^3
v	The y component of the velocity	m s^{-1}
$\vec{v}$	Average velocity	m s^{-1}
x	x-coordinate	m
y	y-coordinate	m
z	Charge number	Dimensionless

Greek

Symbol	Definition	Unit
α	Transfer coefficient	Dimensionless
β	Volume fraction	Dimensionless
ΔG	Change in Gibbs free energy	J mol^{-1}
ΔH	Change in enthalpy	J mol^{-1}
ΔS	Change in entropy	J mol^{-1} K^{-1}
δ	Distance	m
ϵ	Porosity	Dimensionless
ϕ	Electrostatic potential	V
ϕ_e	Ionic potential	V
ϕ_s	Electronic potential	V
γ	Diffusion rate to electrode surface (piston velocity)	m s^{-1}
η	Overpotential	V
κ	Permeability	m^2
λ	Thermal conductivity	W m^{-1} K^{-1}
μ	Dynamic viscosity	kg m^{-1} s^{-1}
μ_i	Electrochemical potential	J mol^{-1}
ρ	Density	kg m^{-3}
σ	Electronic conductivity	S m^{-1}
σ_e	Effective electrical conductivity	S m^{-1}
σ_f	Effective conductivity of the solid material	S m^{-1}
ζ	Current efficiency	Dimensionless
ξ_c	Coulombic (charge) efficiency	Dimensionless
ξ_v	Voltage efficiency	Dimensionless
ω	Flow rate	m^3 s^{-1}

Subscripts	**Meaning**
a	Anodic property
act	Activation
air	Air
app	Applied
av	Average
c	Cathodic property
cell	Cell
coll	Current collector
con	Concentration
elec	Electrode
D	Drag
dl	Double-layer
e	Electrolyte property
f	Fixed charge (in the membrane) property
g	Gas phase property
H^+	Proton property
H_2	Hydrogen property
H_2O	Water property
in	Inlet
i, j, k	Species
L	Limited property
l	Liquid phase property
m	Mixture property
mem	Membrane
O	Oxidised/reactant property
O_2	Oxygen property

ohm	Ohmic
out	Outlet
p	Hydraulic (permeability)
R	Reduced/product property
ref	Reference value
rev	Reversible
s	Solid property (electronic conducting phase)
slip	Slip
T	Total
t	Thickness
w	width
0	Initial or reference value
1	Positive electrode redox reactions
2	Negative electrode redox reactions
2, 3, 4 and 5	V(II), V(III), V(IV) and V(V), respectively
ϕ	Electrokinetic
$\pm$	Positive electrode (+) or negative electrode (−)

Superscripts	**Meaning**
eff	Effective value
eq	Equilibrium value
in	Inlet value
out	Outlet value
s	Surface value
0	Initial value
$'$	Formal property
$\rightarrow$	Vector property
$-$	Volume-averaged property

Abbreviations

BC	Before Christ
EC	Electrochemical capacitor
EDL	Electric double-layer
EIS	Electrochemical impedance spectroscopy
EMF	Electro-motive force
ESS	Energy storage system
OCV	Open-circuit voltage
PDE	Partial differential equations
PEMFC	Polymer exchange membrane fuel cell
PTFE	Polytetrafluoroethylene
RFB	Redox flow battery
SEM	Scanning electron microscope
SHE	Standard hydrogen electrode
SOC	State of charge
V(II)	Vanadium (II) species in solution (V^{2+})
V(III)	Vanadium (III) species in solution (V^{3+})
V(IV)	Vanadium (IV) species in solution (VO^{2+})
V(V)	Vanadium (V) species in solution (VO_2^+)
VRFB	Vanadium redox flow battery
VRLA	Valve-regulated lead-acid
UNSW	University of New South Wales
UPS	Uninterruptible power supplies

Chapter 1

1 Introduction

1.1 Energy Storage Systems

The delivery of electrical energy converted from renewable resources such as wind and solar, which typically suffer from intermittency problems, is highly dependent on reliable and economical energy storage systems (ESSs). ESSs provide an alternative solution to the problem of balancing the generation and consumption of power. They have the ability to store large quantities of energy to meet immediate changes in demand, allowing effective operation of base load units at high and essentially constant levels of power. They have commercial benefits of maximising operations and flexibility for buying or selling power during on-peak periods. ESS technologies employ the following methods to store/deliver energy:

- Chemical method by which coal, gasoline, diesel fuel, natural gas, liquefied petroleum gas, propane, butane, ethanol, biodiesel and hydrogen are converted to mechanical energy and then to electrical energy using heat engines (turbines or other internal combustion engines, or boilers or other external combustion engines) [1].

- Biological method, including starch and glycogen. The energy from the sun is stored and transported in plants and animals as chemical energy in the bonds between atoms in molecules. Biological energy is a sustainable technology developed to reduce the emissions of greenhouse gases and provide environmentally friendly alternatives to some industrial processes [1].

- Electrochemical method, including batteries, flow batteries and fuel cells. This method is environmentally friendly, the storage system can be located near the loads, with a consequential reduction in system losses. A disadvantage of battery storage systems is the high initial cost [1, 2].

- Electrical methods, including capacitor [1], supercapacitor [1,3–5] and superconducting magnetic energy storage [1, 6]. Electrochemical capacitors (EC) store electrical energy in the two series capacitors of the electric double layer (EDL), which is formed between each of the electrodes and the electrolyte ions. The distance over which the charge separation occurs is just a few angstroms. The capacitance and energy density of these devices is thousands of times larger than electrolyte capacitors [1].

- Mechanical method. Energy can be stored in water pumped to a higher elevation using pumped storage methods [1], in compressed air [1, 7], or in spinning flywheels [1]. Underground pumped storage, using flooded mine shafts or other cavities, are also technically possible. Open sea [8] can also be used as the lower reservoir.

- Thermal method, including ice storage, molten salt, cryogenic liquid air or nitrogen, seasonal thermal store, solar pond, hot bricks, steam accumulator, fireless locomotive and eutectic systems. Thermal storage is a temporary storage or removal of heat for later use [9].

ESSs have different characteristics, their own advantages and disadvantages depending on the area of their applications. A comparison between the traditional large scale storage systems and flow batteries is shown in Table 1 [10, 11].

1.2 Batteries

Batteries are broadly categorised into primary and secondary [2, 12, 13]:

1.2.1 Primary Batteries

Primary batteries are disposable and not rechargeable due to their irreversible electrochemical reactions. They are used in devices that have a low current drain.

Zinc-carbon batteries are the least expensive primary batteries and provide a cell voltage of 1.5 V. They are largely used in remote controls, flashlights, clocks and transistor radios. They are more likely to leak as the anode is the container. The

Storage system	Lifetime or number of cycles	% Energy efficiency	Power rating	Discharge duration	Power-related cost ($/kW)
Lead-Acid	5−10 years	85	<50MW	1min−8h	200−300
Flow batteries	1500−2500 cycles	75−85	<15MW	<20h	1200−1500
Compressed air	30 years	57−64	50−300MW	1−20h	425−517
Pumped hydro	30 years	70−85	100−4000MW	4−12h	600
Supercapacitors	10000 cycles	90−95	<100kW	<1min	300
Flywheels	20 years	90−95	<750kW	<1h	300−350

Table 1: A comparison table of flow batteries with other energy storage systems [10, 11].

zinc container becomes thinner as the cell is used due to the oxidation of zinc metal to zinc ions.

Compared to zinc-carbon batteries, alkaline batteries have a higher energy density and longer shelf-life. They have an alkaline electrolyte of potassium hydroxide, instead of the acidic ammonium chloride or zinc chloride electrolyte of the zinc-carbon batteries. They also produce 1.5 V per cell and are used in aircraft transmitters or receivers, televisions and calculators. Alkaline batteries are prone to leaking of potassium hydroxide, a caustic agent that can cause respiratory, eye and skin irritation.

Zinc-Air batteries offer good shelf life (up to 3 years) as well as high energy densities (470 Wh/kg). They are used in traffic signals, watches and electrical fences. They produce approximately 1.65 V per cell. Deep discharge below 0.5 V per cell may result in electrolyte leakage.

The high energy density (130 Wh/kg), constant cell voltage (1.35 V), good shelf life (up to 10 years) of the Zn-HgO batteries, make them applicable in photography, hearing-aids, pacemakers and sensors in military applications. A different form of mercury battery uses mercuric oxide and cadmium; it has a much lower terminal cell voltage (around 0.9 volts) and so has a lower energy density. However, it has an extended temperature range, in special designs up to 180 ^{o}C. Due to the presence of mercury, and the resulting environmental concerns, the sale of mercury batteries is banned in many countries.

For memory and electrical devices, Li-$SOCl_2$ batteries are used. They have a long shelf life, a cell voltage of 3.5 V and an energy density of about 500 Wh/kg; however, during long storage a passivation layer forms on anode, which may lead to temporary voltage delay when the cell is put into service. High cost and safety concerns limit their use in civilian applications.

1.2.2 Secondary Batteries

Secondary batteries are rechargeable since the electrochemical reactions are reversible. It is necessary to charge the battery before using it, because the components will be in a discharged state at the outset.

Lead-Acid batteries are well known examples of secondary batteries. They have high and low temperature performance, low cost, low energy density (30−40 Wh/kg), low charge retention and are used in cars and aircrafts. They have a nominal cell voltage of 2.105 V. Lead is extremely toxic. Long-term exposure to even tiny amounts of lead can cause brain and kidney damage, hearing impairment, and learning problems in children.

Ni-Cd cells have a nominal cell voltage of 1.2 V and a specific energy of (40−60 Wh/kg). They can be used in aircrafts, but as the cell temperature rises, the internal resistance falls. This can pose considerable charging problems. However, vented cell Ni-Cd batteries are used in aviation, rail and mass transit, backup power for telecoms and engine starting for backup turbines. Using vented cell Ni-Cd batteries results in a reduction in size, weight and maintenance requirements compared to other types of batteries. They have long life (up to 20 years) and operate at extreme temperatures (from $-40\ ^oC$ to $+70\ ^oC$) with a cell voltage of up to 1.71 V.

Ni-Fe batteries are often used for backup in situations where they can be continuously charged and they can last for more than 20 years. They have low specific energies (10−50 Wh/kg) and a high cost of manufacture. They have a nominal cell voltage of 1.2 V.

Ni-Zn batteries have a charge/discharge curve similar to 1.2 V Ni-Cd batteries, but with a higher 1.6 V nominal cell voltage and a specific energy of 100 Wh/kg.

They are used in bikes and military vehicles. Ni-Cd, Ni-Fe and Ni-Zn batteries have good durability (400−2000 cycles) and long shelf lives.

Li-ion batteries are used in portable electronics. The specific energy of Li-ion batteries is 100−250 Wh/kg. They have a slow loss of charge when not in use. Their nominal cell voltage is (3.6−3.7 V). They may suffer thermal runaway and cell rupture if overheated or overcharged, and overdischarge can irreversibly damage the battery.

Examples of flow batteries include:

1. The redox flow battery (RFB) (*e.g.* the vanadium redox flow battery, polysulfide bromide battery and uranium redox flow battery), in which all electroactive components are dissolved in the electrolyte [14].

2. The hybrid flow battery (*e.g.* the zinc-bromine, zinc-cerium and zinc-air flow batteries) in which one or more electroactive component is deposited as a solid layer in the system [12]. The main difference between these two types of flow battery is that the energy of the RFB can be determined fully independently of battery power, while the hybrid flow battery, similarly to a conventional battery, is limited in energy to the amount of solid material that can be accommodated on the electrodes. In practical terms this means that the discharge time of a RFB at full power can be varied from several minutes to many days, whereas the discharge time of a hybrid flow battery may be typically varied from several minutes to a few hours.

3. In contrast, the redox fuel cell [15, 16] is a flow battery which only operates to produce electricity *i.e.* it is not electrically recharged.

The potential applications of redox flow batteries are numerous, including load levelling and peak shaving, uninterruptible power supplies (UPS), emergency backup in hospitals and air-traffic control and facilitation of wind and photovoltaic energy delivery [17–19]. Table 2 lists some of large-scale RFB energy storage systems currently in operation [20].

Life cycle costs, simplicity of operation, flexibility and the state of the technology are among the factors that determine the selection of systems for storage applications.

Type	Location	Power/Energy rating
Lead-acid	Golden Vally Electric Association, Alaska	40MW/14MWh
	Puerto Rico Electric Power Company	20MW/14MWh
	Vernon, California, USA	5MW/5MWh
	Metlakatla, Alaska	4MW/2.5MWh
	ESCAR, San Augustin del Guadalix, Spain	2MW/4MWh
	Herne-Sodingen, Germany	1.2MW/1.2MWh
Sodium-Sulphur	Ohito Substation, Japan	6MW/48MWh
	Tsunashima Substation, Japan	6MW/48MWh

Table 2: Some of RFB energy storage systems currently in operation [20].

The main attractions of electrically rechargeable redox flow systems, as opposed to other electrochemical storage batteries are: simplicity of their electrode reactions; low operating temperature; long cycle life for the redox couples; electrochemically reversible reactions; high over all energy efficiency; relatively few problems during deep discharge of the system and no inversion of polarity if one cell of the system fails; an absence of heavy metals during manufacture, use and disposal.

One of the most important features of the RFB technology is that the power and energy capacity of the systems can be separated. The power of the system is determined by the number of cells in the stack and the size of the electrodes whereas the energy storage capacity is determined by the concentration and volume of the electrolyte. Both energy and power can be easily varied from just a few hours, as in emergency, UPS or load-levelling applications to several days or weeks, as needed for remote area stand-alone applications, employing photovoltaic or wind generating systems.

Many RFB storage systems use two soluble redox couples as electroactive species that are oxidised-reduced to store or deliver energy. Both the oxidised and reduced species must be soluble, with their redox potential as far apart as possible, and the

reaction must be reversible. Their costs must be reasonable and the electrolyte must be chemically stable and easy to prepare at high concentrations. The electrodes are usually separated by an ion-exchange membrane while the reactants (contained in separate storage tanks) are recirculated through the redox flow cells where the electrochemical reactions take place.

The membrane should be selective to proton transport in acid electrolytes or sodium ions in the presence of sodium salts. It must reduce the transport of reactive species between the anode and cathode compartments to a minimum rate and allow the transport of non-reactive species and water to maintain electro-neutrality and electrolyte balance. The membrane should also have low electrical resistivity, a long life span, be easy to manufacture and handle, and have a moderate cost. Major problems related to the development of redox flow cells include:

- Self-discharge shunt (bypass or leakage) currents should be minimised by increasing the ionic resistance of the flow ports, by making the length of the manifold longer or by reducing the cross-sectional area of the ports [21] (the increase in the electrolyte flow resistance demands more pumping power, complicating the cell design and increasing costs).

- The occurrence of an uneven flow distribution. The formation of stagnant zones in certain areas of the electrode surface should be minimised [22].

- The concentration of ionic species changes during the operation of the battery due to water transport across the membrane by electro-osmosis.

1.3 All-Vanadium Redox Flow Batteries

The ability of vanadium to exist in solution in four different oxidation states means that the rechargeable vanadium redox flow battery (VRFB) has just one electroactive element instead of two and hence the problem of cross contamination by diffusion of ions across the membrane can be eliminated. The use of vanadium redox couples in both half-cells had been suggested by Pissoort in 1933 [23] and by Pellegri and Spaziante in 1978 [24]. VRFB with sulfuric acid electrolyte was patented by Maria

Skyllas-Kazacos at the University of New South Wales (UNSW) in Australia in 1986 [25] and the first successful demonstration and commercial development was made by Rychcik and Maria Skyllas-Kazacos at UNSW in the 1988 [26].

The energy density of VRFB is quite low (25 Wh/kg) as compared to the lead-acid battery (30−40 Wh/kg) or the lithium-ion battery (80−200 Wh/kg). More recent research at UNSW indicates that the use of precipitation inhibitors can increase the energy density to about 35 Wh/kg, with even higher densities made possible by controlling the electrolyte temperature.

The (VRFB) contains two different electrolyte solutions, each in a separate tank. The electrolytes flow through an electrode on opposite sides of a proton exchange membrane to provide power [17,25,27–29]. VRFBs have the following advantages [30]:

- The solutions have a long life so only the mechanical components need replacement at the end of their life.
- Instant recharge is possible by replacing the spent electrolytes which makes the system attractive for electric vehicle applications.
- The system capacity can be increased by increasing the volume of solution.
- The vanadium battery can be fully discharged with few detrimental effects.
- The cost per kWh decreases as the energy capacity increases, making large scale applications cost effective.
- The capacity of the whole system can be monitored in-line by monitoring the state of charge of the electrolytes (vanadium ions have different colours: V(II) purple, V(III) green, V(IV) blue and V(V) yellow).
- The vanadium battery system is environmentally friendly since no waste products are produced.

Some applications of VRB projects are given in Table 3 [31, 32].

The principle of the VRFB is illustrated in Figure 1 and the typical values of the constants related to its structure in a laboratory are listed in Table 6 in Appendix (A).

Place	Project	Power/Energy rating
Japan	UPS	1.5 MW
Hokkaido	Wind power project	275 kW
Tasmania	Wind power project	200 kW, 800 kWh
Utah	Load levelling	250 kW, 2 MWh
Ireland	Wind power project	12 MWh
Kenya	Wind and Solar power project	5 kW

Table 3: Application projects of VRB [31, 32].

The V(II)/V(III) redox couple, which was investigated by Sum and Skyllas-Kazacos [27], is employed in the negative electrode while the positive electrode employs the V(IV)/V(V) redox couple, which was investigated by Sum *et al.* [33]. When solution crossover occurs, the vanadium half-cell solutions can be remixed and the system brought back to its original state.

On charge, the following reaction occurs at the positive electrode:

$$VO^{2+} + H_2O \rightleftharpoons VO_2^+ + 2H^+ + e^- \quad E^0 = 1.00 \text{ V} \quad \textit{vs.} \text{ SHE} \tag{1}$$

and at the negative electrode, the reaction is:

$$V^{3+} + e^- \rightleftharpoons V^{2+} \quad E^0 = \text{- } 0.26 \text{ V} \quad \textit{vs.} \text{ SHE} \tag{2}$$

There are, in addition, several known side reactions, notably the evolution of oxygen on charge at the positive electrode [34, 35]:

$$2H_2O \rightleftharpoons O_2 + 4e^- + 4H^+ \quad E^0 = 1.23 \text{ V} \quad \textit{vs.} \text{ SHE} \quad \text{Oxygen evolution} \tag{3}$$

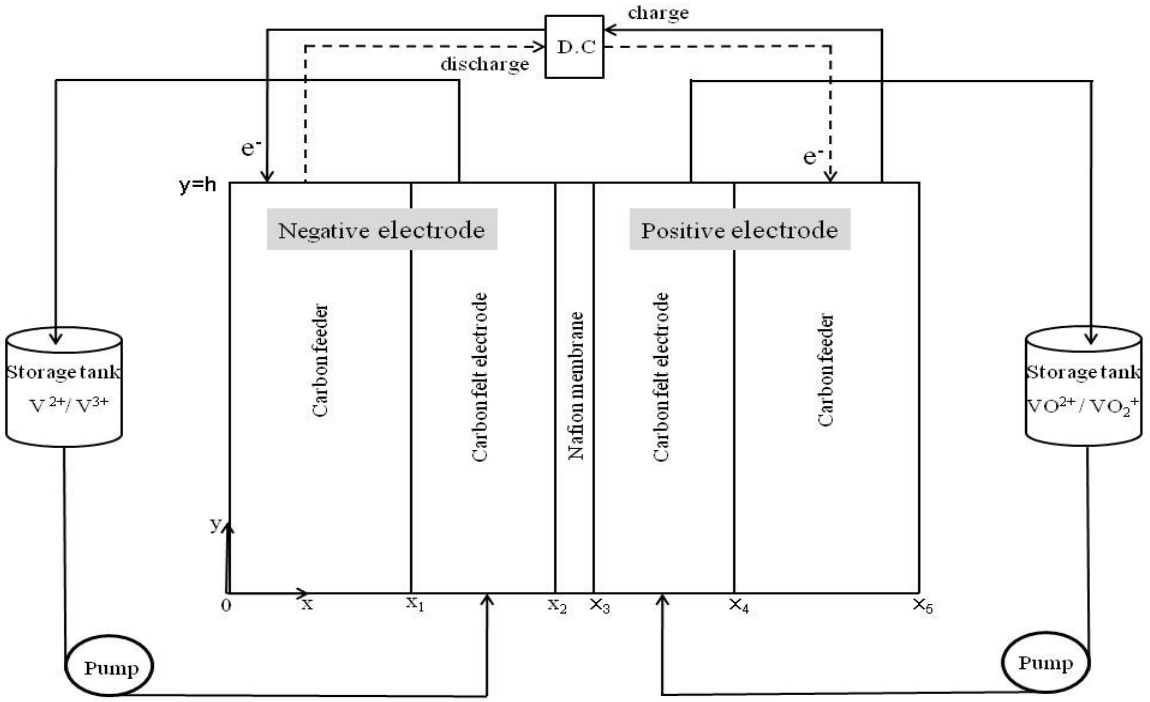

Figure 1: Principle of an all-vanadium redox flow battery.

and the evolution of hydrogen at the negative electrode [34, 36] during charge which proceeds in an acidic environment as follows:

$$2H^+ + 2e^- \rightleftharpoons H_2 \quad \text{Hydrogen evolution} \tag{4}$$

At a concentration of 1 mol L^{-1} of each of the vanadium species at 25^{o}C, the standard cell voltage is 1.26 V but under operating conditions the actual open-circuit voltage obtained at 50% state of charge (defined in equations (115) and (118)) is around 1.35 V [34, 37]. The relatively fast kinetics of the vanadium redox couples allow high coulombic and voltage efficiencies to be obtained but the value of these efficiencies also depends on the internal resistance of the cell and the strength of the side reactions.

The unit VRFB cell, as shown in Figure 2 below, is composed of positive and negative electrodes, which are separated by a membrane. The required specifications of each component are described below [38, 39]:

- In consideration of low pressure loss during electric flow and electric conductiv-

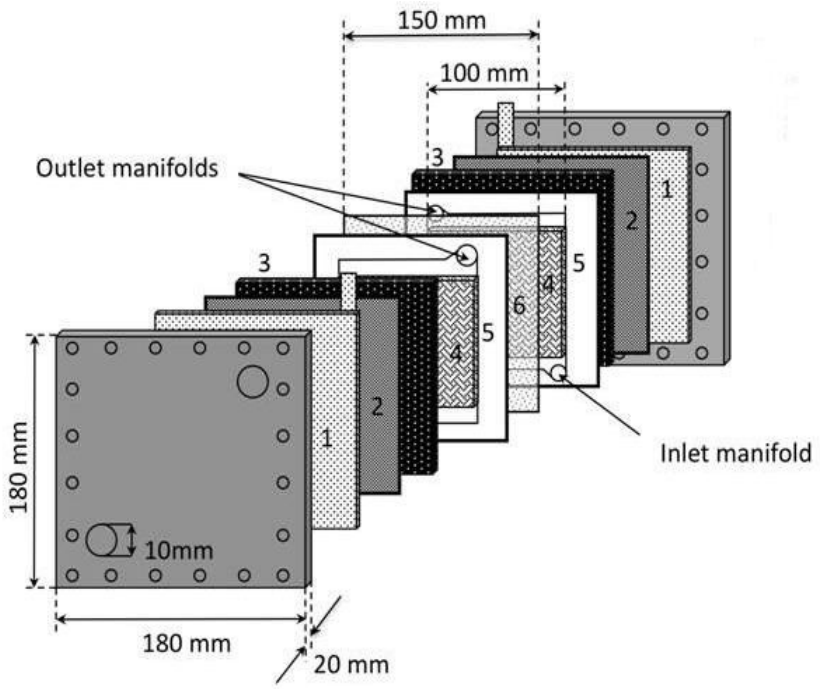

Figure 2: Components of the vanadium redox flow cell: (1) copper backplate; (2) grafoil; (3) carbon-polymer feeder; (4) carbon felt electrode; (5) PTFE gasket; (6) Nafion® membrane.

ity, a carbon felt with an activated surface is used for the electrodes (Figure 3).

- To provide electrical and vanadium ion insulation, high proton (H^+ ion) conductivity, an ion exchange membrane Nafion® 115 is used.
- To allow only electrons to pass while keeping the electrolyte fluid inside, a conductive plastic made by embedding carbon (which is electrically conductive) into plastic (which is fluid impermeable) is used with a copper plate.
- In consideration of cost, hard vinyl chloride is used for the frame.

Other battery cell stack requirements, besides lowered internal resistance, include the following:

1. Pressure loss during pumping of the electrolyte should be minimal.
2. Shunt (bypass or leakage) current loss, which is self-discharge loss through the electrolyte supply pipe, should be minimal. Keeping pressure loss during elec-

(a)

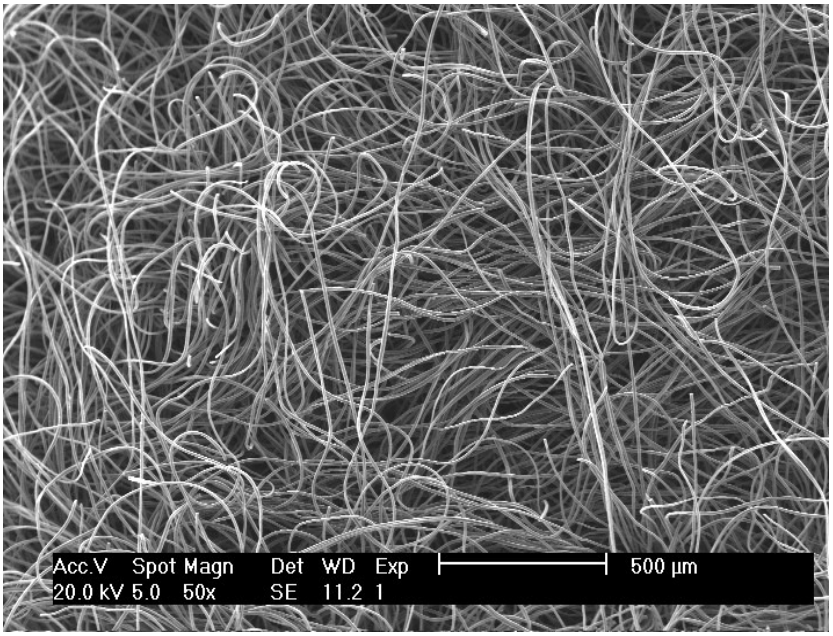

(b)

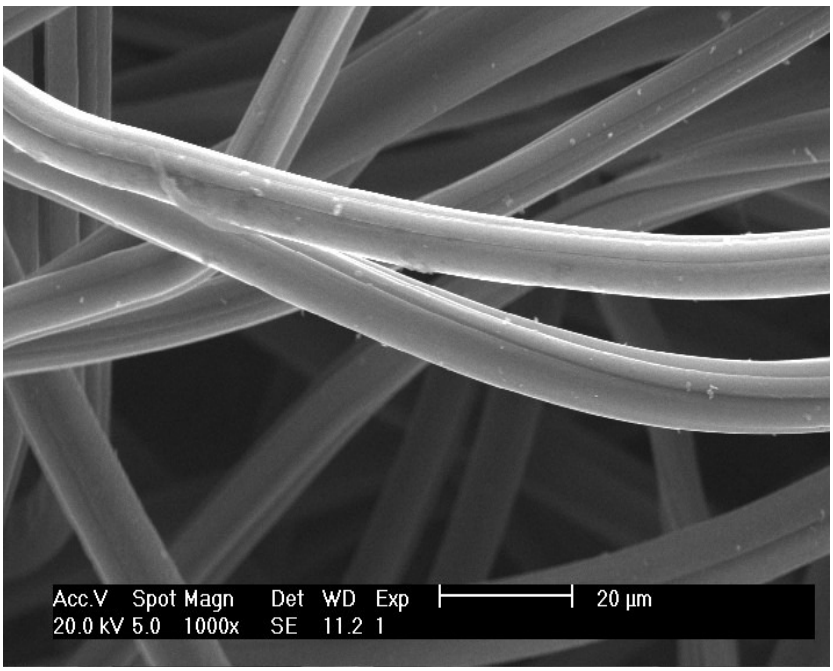

Figure 3: Scanning electron microscope (SEM) images Sigratherm® GFA5: (a) low magnification and (b) a high magnification.

trolyte pumping to a minimum helps raise system efficiency by reducing pumping power. Furthermore, although shunt current loss can be reduced using a narrower fluid route to raise electric resistance, this also increases pressure loss during fluid pumping and thereby increases the required pump power. Thus, it is important to achieve a design that minimises the sum of pump power and shunt current loss.

1.4 Motivation and Structure of the Present Work

The approaching commercialisation of a whole class of redox flow cell storage systems sets a series of new challenges to developers of this new technology, notably scale-up and optimisation (with regards to flow geometries and operating conditions), improvement in electrolyte stability, development of electrode materials resistant to oxidation, and membrane fouling. Many of these challenges are not particularly well-suited to laboratory analysis alone, by virtue of the associated financial costs and long timescales. In such cases it is beneficial to employ modelling and simulation as a means of down-selecting laboratory test scenarios so that, wherever possible, extensive laboratory experimentation can be avoided.

There are, however, few modelling studies of modern RFB systems. Notable exceptions include the models developed by Shah *et al.* [37], Li and Hikihara [40] and Vynnycky [41] for the all-vanadium system and by Scamman *et al.* [42, 43] for the bromine-polysulphide battery. In this thesis, the two-dimensional, transient model of Shah *et al.* [37] is extended considerably to incorporate the effects of changes in operating temperature and gas evolution on the performance of the all-vanadium redox flow battery.

- In chapter two, a review of the literature is presented.
- Chapter three contains details of the experimental work and the model development.
- Simulation results obtained using a non-isothermal model are presented and discussed in chapter four. The influence of the electrolyte flow rate, the magni-

tude of the applied current and heat losses on the charge/discharge behaviour and temperature distribution are investigated.

- In chapter five, the results of numerical simulations are validated against experimental data, for different vanadium concentrations and electrolyte flow rates and the effects of hydrogen evolution (in the negative electrode during charge) on the battery performance are investigated. The effects of the variations in reactant concentrations, flow rate, applied current density and gas bubble diameter on hydrogen evolution are described.

- Simulations involving oxygen evolution are presented and discussed in chapter six. The impact of oxygen evolution and gas bubble formation (in the positive electrode during charge) on the performance is discussed. Parametric studies are performed to investigate the effects of changes in the operating temperature, reactant concentrations, electrolyte flow and bubble diameter on the extent of oxygen evolution.

- Finally, conclusions and recommendations for further work are suggested in chapter seven.

Chapter 2

2 Literature Review

A brief review of the fundamental background needed to derive the mathematical models is presented below. A simplified description of the voltage loss components is also provided.

2.1 The Overall Reaction Rate of Electrode Processes

Consider an electrochemical reaction in which the species O reduces to species R, occurring at an electrode surface [13, 44, 45]:

$$\mathrm{O} + n\mathrm{e}^- \rightarrow \mathrm{R} \tag{5}$$

where n is the number of electrons. The amount of material undergoing electrochemical change, m, is proportional to the amount of electrical charge, q=It, according to Faraday's law:

$$m = \frac{It}{nF} \tag{6}$$

where I is the current, t is the time, n is the number of electrons involved in electrode reaction and F is Faraday's constant.

The rate of loss of reactant in reaction (5) is:

$$\frac{dm}{dt} = \frac{I}{nF} \tag{7}$$

At the electrode/electrolyte interface, the flux density of reactant or product species,

N, is equal to the electron flux density:

$$N = \frac{j}{nF} \tag{8}$$

where $j = I/A$ is the current density and A is the cross sectional area of the electrode.

The current efficiency, ζ_i, which is the fraction of electrical charge used for the primary (desired) reaction, can be used to accommodate for the side reactions:

$$\zeta_i = \frac{q}{q_T} \tag{9}$$

where q_T is the total electrical charge.

In the case of constant current, equation (9) becomes:

$$\zeta_i = \frac{I}{I_T} \tag{10}$$

where I_T is the total current.

Division of equation (8) by the bulk reactant concentration, c, leads to:

$$\frac{N}{c} = \frac{j}{nFc} \tag{11}$$

Under complete mass transport control, I=I_L where I_L is the current limited by the rate of convective-diffusion of reactant species to the electrode surface. Therefore, the mass transport coefficient, k_m, which is the rate constant for mass transport to the electrode is:

$$k_m = \frac{I_L}{nFAc} \tag{12}$$

2.1.1 Overpotential

The overpotential, η is the difference between the potential of the electrode, E and the theoretical reversible equilibrium potential, E^{eq}:

$$\eta = E - E^{eq} \tag{13}$$

where the reversible equilibrium potential for the reaction (5) is related to the formal potential,E_0^{eq} and is given by the Nernst equation:

$$E^{eq} = E_0^{eq} + \frac{RT}{nF} \ln\left(\frac{c_O}{c_R}\right) \tag{14}$$

The overpotential arises due to the hindrance to the overall electrode reactions. The overpotential resulting from a positive or negative current will cause a positive or negative overpotential, respectively. Naturally, there will be no overpotential in the absence of current. The voltage of the battery, E_{cell}, is approximated by:

$$E_{\text{cell}} = (E_+^{eq} \pm \eta_+) - (E_-^{eq} \mp \eta_-) - I\sum_i R_i \tag{15}$$

where E_+^{eq} and E_-^{eq} are the theoretical reversible cell potentials found from thermodynamics (Gibb's free energy change) at the positive and negative electrodes, respectively, η_+ and η_- represent the concentration and activation overpotentials in the positive and negative electrodes, respectively and $(I\sum_i R_i)$ is the ohmic losses.

In order to find the total cell voltage it may be useful to divide the voltage losses into several components (as shown in Figure 4): the concentration overpotential (mass transport limitations), activation overpotential (charge transfer limitations) and the ohmic drop (resistance to e^- and H^+ transport). The concentration overpotential appears when the supply of reactants at the electrode or the removal of the reaction products is rate-determining when current flows. The formation of the activation

overpotential is caused by the resistance to the charge transfer reaction. That is, the transport of charge carriers through the electrical double layer is hindered. This charge-transfer potential can be approximated using the Butler-Volmer law [46]. The ohmic losses, also called 'IR' drops are defined as the potential drops within the various components (resistance to e^- and H^+ transport), as well as across compartments (contact resistance). Finally, the reversible cell potential is usually not realised in practise (at zero current) due to internal currents and fuel crossover. In the case of charging, η_+ and η_- are preceded by a plus-sign and minus sign, respectively. This situation is reversed in the case of discharging. The difference in the equilibrium potentials is the electromotive force, EMF:

$$\text{EMF} = E_+^{eq} - E_-^{eq} \tag{16}$$

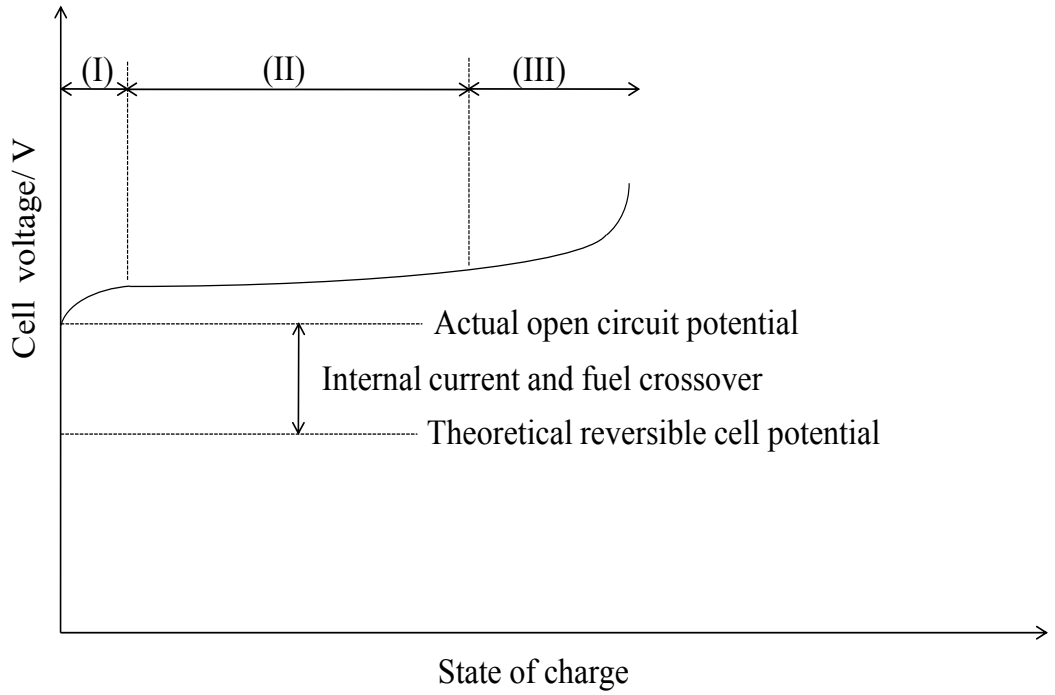

Figure 4: Characteristic cell voltage profile during charge: (I) region of dominant activation losses ; (II) region of dominant ohmic losses; (III) region of dominant mass transport losses.

2.1.2 Reaction Rate Expressions

1. Charge transfer controlled reaction

   If the reaction rate is under the electron (charge) transfer control, (*i.e.* the electrode process is occurring at a low rate compared to the rate at which reactant is supplied to the surface or product is removed), for a first order reaction (5):

$$\text{Rate of reduction} = \frac{dm}{dt} = k_c \; c_O^s \tag{17}$$

$$\text{Rate of oxidation} = \frac{dm}{dt} = k_a \; c_R^s \tag{18}$$

   where c_O^s and c_R^s are the concentrations of the reactant and product species at the electrode surface, respectively, k_c and k_a are the rate constants for the cathodic (forward) and anodic (reverse) reactions, respectively. They are related to the electrode potential, E by:

$$k_c = k_{c,0} \exp\left(\frac{-\alpha_c n F E}{RT}\right) \quad \text{for a reduction process} \tag{19}$$

$$k_a = k_{a,0} \exp\left(\frac{\alpha_a n F E}{RT}\right) \quad \text{for an oxidation process} \tag{20}$$

   where $k_{c,0}$ and $k_{a,0}$ are the rate constants for the reduction and oxidation processes at E=0, respectively. α_c and α_a are the cathodic and anodic transfer coefficients. For a simple electrode reaction *i.e.* $\alpha_c + \alpha_a$=1; they are kinetic parameters indicating the direction of electrochemical reaction due to the applied potential and signify the fraction of overpotential that affects the current density by lowering the free activation energy for the reaction at an electrode-electrolyte interface [45].

2. Mass transport controlled reaction

If the reaction rate is only restricted by the rate of mass transport of species (*i.e.* electron transport is very fast), then equations (17) and (18) become:

$$\text{Rate of reduction} = \frac{dm}{dt} = k_m \; c_O \tag{21}$$

$$\text{Rate of oxidation} = \frac{dm}{dt} = k_m \; c_R \tag{22}$$

where c_O and c_R are the bulk concentrations of the reactant and product species, respectively and k_m is the mass transport coefficient given in equation (12).

By the conservation of mass at the electrode surface, the reactant loss flux is proportional to the electron transfer flux, which is proportional to the product formation flux.

For pure diffusion transport:

$$-D_O \frac{dc_O^s}{dx} = \frac{j}{nF} = D_R \frac{dc_R^s}{dx} \tag{23}$$

where D_O and D_R are the diffusion coefficients of the reactant and product species, respectively. The current density is:

$$j \approx nF D_O \left(\frac{c_O - c_O^s}{\delta} \right) \tag{24}$$

where δ is the distance travelled from the bulk to the electrode surface (Nernst diffusion layer).

3. Mixed controlled reaction

With the contribution from both electron transfer and mass transport to the overall conversion of O to R in reaction (5), equations (17) and (18) become:

$$\text{Rate of reduction} = \frac{dm}{dt} = k_m \left(c_O - c_O^s\right) \tag{25}$$

$$\text{Rate of oxidation} = \frac{dm}{dt} = k_m \left(c_R - c_R^s\right) \tag{26}$$

Solving equations (17)and (25) for c_O^s leads to:

$$c_O^s = \frac{c_O}{1 + k_c/k_m} \quad \text{for reduction process} \tag{27}$$

Similarly, solving equations (18) and (26) for c_R^s leads to:

$$c_R^s = \frac{c_R}{1 + k_a/k_m} \quad \text{for oxidation process} \tag{28}$$

Substitute equations (27) and (28) into equations (25) and (26), respectively to get:

$$\text{Rate of reduction} = \frac{k_c \; c_O}{1 + k_c/k_m} \tag{29}$$

$$\text{Rate of oxidation} = \frac{k_a \; c_R}{1 + k_a/k_m} \tag{30}$$

Equations (29) and (30) can be used to recognise the determining step in the reaction process, *i.e.* if k_c or $k_a << k_m$, then the slow step is the charge transfer and the overall rate is electron transfer controlled and therefore, equations (29) and (30) reduced to equations (17) and (18), respectively. On the other hand, if k_c or $k_a >> k_m$, then the reactant supply or the removal of the reaction

products is the rate determining step and the overall rate is mass transport controlled and thereby, equations (29) and (30) reduced to equations (21) and (22), respectively.

2.1.3 Butler-Volmer Equation

Substitute equations (19) and (20) into equations (17) and (18), respectively, to get:

$$j_c = nFk_{c,0}c_O^s \exp\left(\frac{-\alpha_c nFE}{RT}\right) \quad \text{for reduction process} \tag{31}$$

$$j_a = nFk_{a,0}c_R^s \exp\left(\frac{\alpha_a nFE}{RT}\right) \quad \text{for oxidation process} \tag{32}$$

The surface concentration of species will be very close to that in bulk solution, since the surface reaction occurs at a low rate [45]. Therefore, the net (observed) current density, j can be obtained from equations (31) and (32):

$$j = j_a + j_c = nFk_{a,0}c_R \exp\left(\frac{\alpha_a nFE}{RT}\right) - nFk_{c,0}c_O \exp\left(\frac{-\alpha_c nFE}{RT}\right) \tag{33}$$

At some value of E^{eq}, the rate of the cathodic reaction equals the rate of anodic reaction and the net rate of reaction, j is zero, therefore:

$$j_0 = j_a = -j_c \tag{34}$$

and therefore, equation (33) becomes:

$$nFk_{a,0}c_R \exp\left(\frac{\alpha_a nFE^{eq}}{RT}\right) = nFk_{c,0}c_O \exp\left(\frac{-\alpha_c nFE^{eq}}{RT}\right) \tag{35}$$

Noting that $\alpha_a + \alpha_c$=1, rearrange equation (35) to get:

$$E^{eq} = \frac{RT}{nF} \ln \left(\frac{k_{c,0} c_O}{k_{a,0} c_R} \right) \tag{36}$$

Substituting equations (13) and (36) into (33) leads to Butler-Volmer equation which relates the current density to overpotential:

$$j = j_0 \left[\exp \left(\frac{\alpha_a nF\eta}{RT} \right) - \exp \left(\frac{-\alpha_c nF\eta}{RT} \right) \right] \tag{37}$$

where the exchange current density, j_0 depends on the concentrations of reactants and products, temperature, the nature of the electrode-electrolyte interface and impurities that may contaminate the surface:

$$j_0 = nF \; k_{a,0}^{\alpha_c} \; k_{c,0}^{\alpha_a} \; c_R^{\alpha_c} \; c_O^{\alpha_a} \tag{38}$$

Four cases of electron transfer control may be distinguished according to the magnitude and sign of the overpotential as shown in Figure 5:

- By taking decadic logarithms of equation (39), manipulation leads to the cathodic Tafel slop$=-2.3RT/\left(\alpha_c nF\right)$ which has the value of -118 mV at 298 K for one electron change and α_c=0.5.

  At a very negative value of η (region 1), $j \approx j_c$, $E << E^{eq}$ and $\eta < -118/n$ mV. Equation (37) reduces to:

$$j \approx j_c = -j_0 \exp \left(\frac{-\alpha_c nF\eta}{RT} \right) \tag{39}$$

- At a very positive value of η (region 2), $j \approx j_a$, $E >> E^{eq}$ and $\eta >118/n$ mV. Equation (37) reduces to:

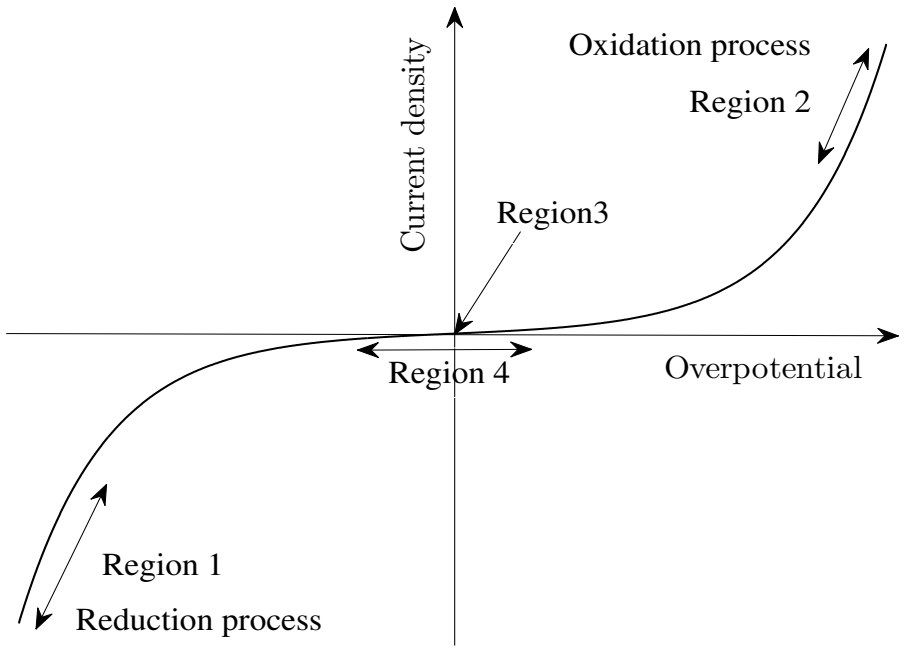

Figure 5: Current density *vs* overpotential curve for a charge transfer controlled reaction.

$$j \approx j_a = j_0 \exp\left(\frac{\alpha_a n F \eta}{RT}\right) \tag{40}$$

and the anodic Tafel slope=$2.3RT/(\alpha_a nF)$ which has the value of 118 mV at 298 K for one electron change and α_a=0.5.

- At equilibrium (region 3), η=0, j=0, $j_0 = j_c = -j_a$ and $E = E^{eq}$ from equation (13).

- At very small value of η, $|\eta|$<10 mV (region 4), equation (37) reduces to:

$$j = j_0 \left(\frac{nF\eta}{RT}\right) \tag{41}$$

2.2 Transport Processes in Electrolyte Solutions

An electric field is created by applying a potential difference to an electrode. This driving force, $\vec{E}$, for reaction is related to the ionic potential, ϕ_e, by:

$$\vec{E} = -\nabla\phi_e \tag{42}$$

The current density, $\vec{j}$, is related to the ionic potential by Ohm's law:

$$\vec{j} = -\sigma\nabla\phi_e \tag{43}$$

where σ is the electronic conductivity.

Applying an electric field across an ionic solution produces a driving force for ionic current given by:

$$\vec{j} = \sum_i z_i F \vec{N}_i \tag{44}$$

where z_i is the charge number of species i in the solution.

Mass transfer arises either from the differences in electrical or chemical potential or from the movement of a volume element of the solution. It can occur due to [13]:

- Migration which is the movement of a charged body due to an electric field, *i.e.*, an electrical potential gradient. The flux density of a species i in the solution due to its migration is equal to its velocity multiplied by its concentration:

$$\vec{N}_{i,migration} = -z_i U_i c_i F \nabla\phi_e \tag{45}$$

  where U_i and c_i are the mobility and concentration of the species i in the solution, respectively.

- Diffusion which is the movement of a species due to a gradient of chemical potential, *i.e.*, a concentration gradient. The flux density of a species i due to its diffusion into the solution is given by:

$$\vec{N}_{i,diffusion} = -D_i \nabla c_i \tag{46}$$

where D_i is the diffusion coefficient of species i.

- Convection results from an imbalance of forces on the solution. The convection flux density of species i in the solution is given by:

$$\vec{N}_{i,convection} = c_i \vec{u} \tag{47}$$

where $\vec{u}$ is the velocity of the bulk fluid.

2.3 Dilute Solution Theory

A dilute solution contains a relatively small quantity of solute compared with the amount of solvent. This solution consists of a non-ionised solvent, ionised electrolytes and uncharged minor components. In dilute solutions, the bulk velocity is essentially the same as the velocity of the solvent. Also, the interaction or friction force of a solute species with the solvent is considered while interactions with other solutes are neglected. Furthermore, the activity and concentration gradients of extremely dilute solutions are identical. In addition, for multicomponent diffusion, each species diffuses independently according to its own concentration gradient and diffusion coefficient. However, the solute species do not diffuse independently even in the absence of a current. The diffusing ions will interact with the established diffusion potential [13].

2.4 Concentrated Solution Theory

In contrast to dilute solution theory which assumes interaction of ions with the solvent only and not with other ions, the concentrated solution theory includes interactions among all species present in the solution. Furthermore, the activity coefficients of species and solvent are not unity in concentrated solution theory (dilute solution theory assumes all activity coefficients are unity [13]).

The foundation of concentrated solution theory is the Stefan-Maxwell multi-component diffusion equation:

$$c_i \nabla \mu_i = RT \sum_j \frac{c_i c_j}{c_T D_{ij}} (\vec{v}_j - \vec{v}_i) \tag{48}$$

where μ_i is the electrochemical potential, $\vec{v}_i$ is the average velocity of species i and D_{ij} is the diffusion coefficient describing the interaction of species i and j. The total concentration, c_T of the species i and the solvent is:

$$c_T = \sum_i c_i \tag{49}$$

2.5 Binary Electrolyte Solutions

A binary electrolyte contains a single salt composed of one kind of cation and one kind of anion (written 1−1 electrolytes; for example, KCl). This implies a symmetric electrolyte, which dissociates into equal numbers of anions and cations. In such solution, the mobilities and the diffusion coefficients can be assumed constant. In the case of a binary-electrolyte, concentrated solution theory is straightforward but becomes cumbersome when numerous species are involved [47].

2.6 Porous Electrodes

Many authors have discussed porous electrodes [48–52]. In most cases the porous electrodes are modelled as consisting of small pores (rectangular, cylindrical or spherical) in which a diffusion or diffusion-convection problem has to be solved. Porous elec-

trodes consists of porous matrices of a single reactive electronic conductor or mixtures of solids that include essentially nonconducting reactive and electronic conductors. Physical structure, conductivity of the matrix, conductivity of the electrolyte and catalytic activity are among the factors that affect the distribution of the range of reaction rate within the pore at a given time. The electroneutrality (defined in chapter (3)) is applicable within porous electrode because it requires a large electric force to create a noticeable separation of charge over a noticeable distance. Porous electrodes have numerous industrial applications by providing a large interfacial area per unit volume, thereby increasing the rates of electrochemical reactions.

2.7 Electrical Double Layer

The excess of charge on the electrode surface is counterbalanced by the accumulation of ions, of opposite charge, on the solution side of the interface. Therefore, the transfer of charge across the electrode surface causes a charge separation. The layer across which this charge separation occurs is called the electrical double layer, and is extremely thin compared with the width of the electrolyte and electrodes [53]. In many models, the presence of this electrical double layer is neglected. This can be justified by arguing that the electrical double layer is extremely thin and is built up within microseconds, whereas the charging process takes thousands of seconds.

The Helmholtz model describes the double layer as a parallel plate capacitor with a small plate separation as shown in Figure 6. In this model, the potential changes linearly from the electrode potential ϕ_s to the electrolyte potential ϕ_l in a thin layer of thickness d. This layer is referred to as the Helmholtz layer and can be described by a constant capacitance C_{dl} [53].

The Gouy-Chapman or Gouy-Chapman-Stern model [54], includes the presence of another thicker layer of charge at the solution side of the double layer, consisting of both positive and negative charges. This layer is called the diffuse layer because the concentration profiles slowly diffuse to the bulk concentration. However, for highly concentrated solutions, the effect of this diffuse layer is less pronounced.

At the beginning of the charging process, most of the total current is used for

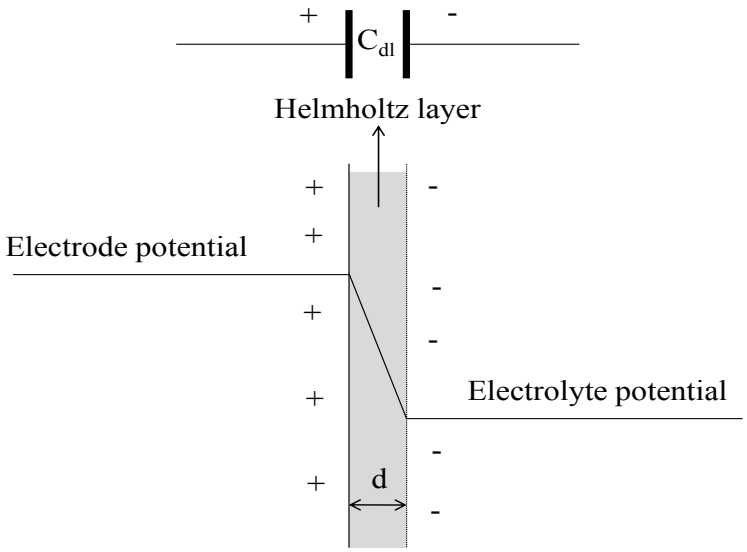

Figure 6: Electrical double layer as a parallel plate capacitor with capacitance C_{dl}. The electrode is assumed to be positively charged.

charging the double layer and thus the current used for the charge-transfer reactions will be very small. However, on a longer time-scale, after the double layer is fully charged, most of the current will be used for the charge-transfer reactions and will approximate the total current, *i.e.*, the double layer current is small [53].

2.8 Modelling of Electrochemical Cells

The first known battery is that in the form of the so-called Baghdad battery from sometime between 250 BC and 250 [55]. However, Luigi Galvani, lecturer in anatomy at the University of Bologna in 1790, and Alessandro Volta, professor of physics at Pavia University in 1800 initiated the study of the science and development of many types of batteries.

The modelling of electrochemical processes has improved over the past 50 years to analyse problems involving multiple reactions, temperature variations, and physical property variations. The mathematical description of batteries plays an important role in the design, control and monitoring of batteries. Modelling can reduce the design time and provide a fundamental understanding of the chemical and physical processes that occur in batteries [56–60]. It can also be used to monitor and control

battery performance during use. Various battery models found in the literature are presented below.

2.8.1 Models of Rechargeable Batteries

Fan and White [57] proposed a mathematical model for a sealed nickel-cadmium cell to predict the cell performance during charge, discharge, reset and cycling and the sensitivity of the model to those parameters. The model applied the theory of concentrated binary electrolyte solutions. The sensitivity analysis showed that the cell performance was affected primarily by the product of the exchange current density and the specific surface area. The model suggested that the discharge process is under activation control. Although the performance of nickel-cadmium batteries is affected by the presence of oxygen, the model ignored the existence of the oxygen in the gas phase.

Wang *et al.* [60] developed a general micro-macroscopic coupled model for advanced batteries and fuel cells, incorporating phase-interaction terms under interfacial nonequilibrium conditions. The model used a lumped approach to describe solid-state diffusion of the reactants and an electrical resistance to represent the ohmic drop inside the active material, rather than using exact differential equations. The model suggested that good approximations can be achieved by assuming spherically shaped particles. Gu *et al.* [61] used this model to predict the charge/discharge behaviour of nickel-cadmium and nickel-metal hydride cells (Ni-MH). Porous nickel oxyhydroxide was used as the active material for the positive electrode in both Ni-Cd and Ni-MH cells. Good agreement was obtained by comparing the predicted results with the reported experimental results available in the literature. A further development to this model was made by Gu *et al.* [62] by incorporating proton diffusion in the nickel active material, the hydrogen diffusion in the metal-hydride particles and the oxygen reactions. Results were validated against charge and discharge experiments, with good agreement. Gu and Wang [63] extended this model to incorporate the heat generation and temperature-dependent physiochemical properties. The resulting multidimensional thermal-electrochemical coupled model was used to predict the

average cell temperature and the temperature distribution inside the cell.

The isothermal electrochemical model for a galvanostatic discharge of Li/Li-ion batteries (based on theory of concentrated binary electrolyte solutions) proposed by Doyle *et al.* [64] was used by many researchers to investigate the behaviour of these batteries. Concentrated solution theory was applied by Fuller *et al.* [56] to develop a general model of a lithium-ion cell based on the physical properties and system parameters. Results suggested that at high discharge rate the utilisation of the positive electrode was limited by the availability of lithium ions in the electrolyte solution. A steady-state mathematical model for lithium-ion rechargeable batteries was described and applied by Doyle *et al.* [65]. The model included a double-layer charging current. Gomadam *et al.* [66] has reviewed and discussed mathematical models of Li/Li-ion, nickel and nickel hydroxide cells developed at the University of South Carolina. The development of a non-isothermal, three-dimensional model for lithium-ion batteries was presented by Kim *et al.* [67]. The model investigated the effects of nonuniform temperature distributions and localised heating or cooling on the battery performance.

The development of lead-acid battery models began in the fifties [68]. Newman and Tiedemann [69] reviewed the development in the theory of flooded porous electrodes (where the pores were considered to be filled with electrolyte) prior to 1975. Tiedemann *et al.* [70] proposed a one-dimensional model to describe the discharge behaviour of the lead-acid battery system using flooded electrode.

Bernardi *et al.* [71] applied the theory of concentrated binary electrolyte solutions and used an approach that involved explicitly solving the governing model equations of Tiedemann *et al.* [70] in two dimensions to predict substantial variations in the current density and sulfuric acid concentration along the cell height and thickness. Free convection was not included in the model and the cell voltage averaged over the cell height was found by using a one-dimensional model. Further developments to the model were made by Gu *et al.* [72] by applying Darcy's law to describe the fluid dynamics in porous media. The model incorporated acid stratification due to convection. The concentration profiles and flow velocities were compared with

measured data. Gu *et al.* [73, 74] extended their approach by using a simple, single-step reaction model with a function for the electrode morphology, leading to greater accuracy. Results showed that the surface overpotential was increased when the rate of change in the active specific area for electrode reaction was increased.

Gu *et al.* [75] proposed a time- and temperature-dependent, one-dimensional model to describe the behaviour of lead-acid cells during discharge, rest and charge. Concentrated binary electrolyte theory was used. Use of a thin positive electrode was found to reduce the time for discharge by approximately 50 % due to the depletion of acid. For the same reason, increasing the porosity of the positive electrode led to a decrease in the time for discharge by approximately 35 %. Dimpault-Darcy *et al.* [76] proposed a two-dimensional model of a single porous electrode based on concentrated binary electrolyte theory to simulate a lead oxide electrode by assuming a uniform current density at the face of the electrode, which led to insignificant variations along the electrode height.

Simonsson *et al.* [77] and Ekdunge and Simonsson [78, 79] developed a new electrode reaction model for the porous lead electrode in the lead-acid battery by applying dilute-solution theory. The charge transfer was found to be the rate-limiting step at high overvoltages, while reactant diffusion was the rate-limiting step at lower overvoltages. Landfors *et al.* [80] applied this model to measure and predict the acid concentration distribution in the cell, and demonstrated good agreement with experimental data. Liaw and Bethune [81] extended the work of Wang *et al.* [61] to include gas evolution effects in the overcharge regime of a valve-regulated lead-acid (VRLA) battery. Cell physical properties (dimensions, porosity and effective surface area), kinetic data reported in the literature and the oxygen and hydrogen evolution exchange current densities obtained experimentally from the cell were used to simulate the gas evolution reactions.

Bernardi and Carpenter [82] developed a two-phase model (dissolved oxygen through the liquid film within the lead electrode), assuming a binary electrolyte solution, to describe cell voltage degradation due to oxygen evolution during charge in a lead-acid cell. The gas formation processes were analysed with an isothermal, one-

dimensional model which showed that the formation of lead sulfate from the reaction of oxygen with lead cannot lead to a voltage maximum. However, the oxygen cycle was unaffected by the electrolyte saturation level in the separator due to the assumption of rapid transport of oxygen across the separator. The description of oxygen generation in a lead-acid battery was also modelled by Newman and Tiedemann [83], again assuming a binary electrolyte solution. Their model can be extended to all recombinant battery chemistries. The model did not capture the effects of transport properties and separator design on the internal gas cycle due to the simplifications made in the model by ignoring the distributions of current and species concentrations. The gas formation processes were also analysed in [84] with a two-dimensional model. The results showed that thermal runaway can be avoided by using materials with large heat transfer coefficients. Operating the battery at high ambient temperature was found to increase the possibility of thermal runway. The rate of heat generation was found to vary non-linearly with the local temperature and was distributed non-uniformly among the electrodes.

A one-dimensional model with a comprehensive description of the physical and chemical processes within a lead-acid battery, based on a macroscopic description of the porous electrodes and concentrated solution theory to characterise species transport in the electrolyte, was developed and combined with the vehicle simulation package ADVISOR by Harb *et al.* [85]. Simulations were performed with a set of parameters given by Bernardi *et al.* [82] and Newman *et al.* [83]. Results demonstrated the feasibility of using the model for the simulation of hybrid vehicle performance.

The effects of corrosion on the performance of a lead-acid battery were modelled by Boovaragavan *et al.* [86] using binary-electrolyte theory. The corrosion process that occurs at the interface between the active mass and grid material of the positive plate was considered as a side reaction. This made the model more suitable for studying the effect of corrosion on the performance of the battery, since it is able to predict the losses in the charge or discharge voltage.

2.8.2 Models of Flow Batteries

A steady-state model was developed by Trainham and Newman [87] to investigate the effects of the direction of the applied current on the performance of a general redox flow battery. A comparison was made between the flow-by electrode configuration, in which current was applied perpendicularly to the fluid flow and the flow-through, in which the current was applied parallel to the fluid flow. Applying the current perpendicularly to the fluid flow was found to exhibit a worse performance due to the requirement of very low flow rates (Re <0.001). It is worth mentioning that some researchers have used a different definition of the terms 'flow-by' and 'flow-through'. A flow-by electrode configuration is defined as a planner, two-dimensional electrode with electrolyte flowing past or 'by' the electrode, while a flow-through is defined as a porous, three-dimensional electrode with electrolyte flowing 'through' the electrode. Fedkiw and Watts [88] extended the model in [87] to incorporate the effects of nonlinear kinetics, temperature variations, multi-electrode reactions at each half cell, electrode length and variations in the current flow direction on the performance of an iron-chromium redox flow battery. Optimum values for the electrode length and thickness, cell voltage and electrolyte flow rate were suggested (to maximise the cell current and charge efficiency). Results suggested that increasing the battery operating temperature enhances the reaction rates and increase the conductivities of the electrolyte and membrane, reducing the time to charge and hence increasing the cycle energy efficiency.

Models of the zinc-bromine flow battery were reviewed and used by Evans and White [89] to investigate the effects of design parameters on battery performance. The influence of porous electrode thickness on the performance of the zinc-bromine battery was modelled by Evans and White [90]. However, the model ignored effects associated with the reaction of zinc ions with bromide, a second bromine-rich phase, time dependence, and the reservoirs. Simpson and White [91] developed an isothermal model based on a set of ordinary differential equations to describe the performance of a parallel flow zinc-bromine cell. The assumption of laminar flow in a dilute solution was made. Simpson and White [92] later extended this work to include the external

storage tanks and time-variations effects on the performance of a zinc-bromine flow cell.

Scamman *et al.* [42] developed a one-dimensional model to investigate the effects of the operating conditions on the performance of a general redox flow battery. The model was based on mass transport from the electrolyte bulk to the electrode surface and reaction kinetics followed the Butler-Volmer equation, with first-order reaction rates and equal rate constants for anodic and cathodic processes. Temperature effects were neglected. The authors used the model to optimise the current density and to investigate the influence of the model parameters on the performance of a bromide-polysulphide redox flow battery [43].

Although a dynamic model describing the transient characteristics of the all-vanadium redox flow battery was presented by Li and Hikihara [93], the model ignored the electrolyte recirculation. A comprehensive isothermal dynamic model of an all-vanadium redox flow battery was developed by Shah *et al.* [37]. However, the model ignored the effects of temperature variations and gas evolution. The effects of electrode porosity, applied current density, electrode thickness and local mass transfer coefficients on the behaviour of the cell were discussed in the steady-state model developed by You *et al.* [94], which was based on the model of Shah *et al.* [37]. The authors neglected the charge transfer due to the electrical potential gradient and the time dependent terms in the mass conservation equation. Al-Fetlawi *et al.* extended the model in [37] by incorporating variations in the operating temperature as well as hydrogen and oxygen evolution [95–97]. These models and the results will be described in detail in the following chapters, representing the bulk of the thesis.

2.8.3 Models of Fuel Cells

The physical processes inside a polymer electrolyte membrane fuel cell (PEMFC) have been extensively investigated using modelling and simulation tools [98–104]. Recently, Shah *et al.* [105] reviewed PEMFC models in detail. Only models for transport in the PEMFC, which are relevant to the present work are discussed. Springer *et al.* [98] proposed an isothermal, one-dimensional, steady-state model for PEMFC to

describe water and proton transport in the Nafion® membrane based on a dilute-solution approximation. The model incorporate electro-osmotic (potential gradients and transport coefficient incorporating osmotic and mechanical drag) and diffusion (concentration gradients and the back diffusion from the cathode to anode) to describe the water and proton movement in the cell (water molecules form clusters attached to a proton). Transport parameters were considered to be functions of the water content and temperature (based on equilibrium conditions between the membrane water and electrode water vapour at the membrane/electrode interface).

Bernadi and Verbrugge [99, 100] replaced the back diffusion mode of transport in [98] with a hydraulic mode, which is more accurate at fully liquid-saturated conditions, when the water may be considered bulk-like. The model was based on the Nernst-Planck and Schlögl [106] equations, and assumed a two phase flow in a porous membrane fully saturated with liquid water. Since the VRFB electrodes are flooded, the formulation of Bernadi and Verbrugge [99, 100] is used in the model developed in chapter (3) of this thesis (more details are given in section 3.3).

2.8.4 Equivalent-Circuit Models

Although not a focus of this thesis, the equivalent-circuit approach, which is used extensively to model electrochemical systems and can have advantages for certain applications is briefly described in this section. Equivalent-circuit models are based on a description of the battery as a circuit network composed of a capacitor, resistors, and a constant voltage source, as shown in Figure 7 [107–112]. Based on the equivalent-circuit approach, the cell voltage is given by:

$$E_{\text{cell}} = E^{eq}_{\text{cell}} - \eta_{act} - \eta_{con} - \eta_{ohm} - \eta_{dl} \tag{50}$$

where E^{eq}_{cell} is the theoretical, reversible open circuit voltage (OCV), η_{act} is the activation overpotential obtained by inverting either a Tafel or Butler-Volmer equation, η_{con} is the concentration overpotential, η_{ohm} is the ohmic losses and η_{dl} is the overpotential due to transient double-layer effects, which is usually introduced as a capacitor

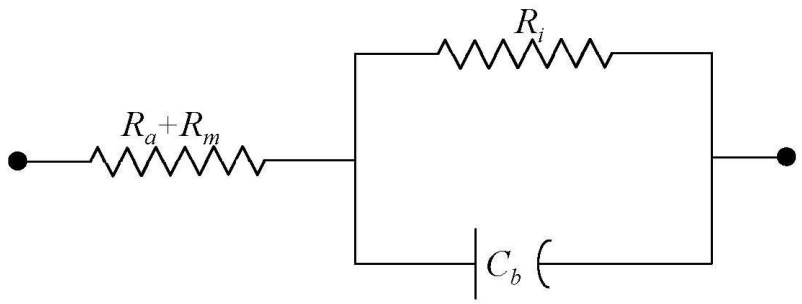

Figure 7: An equivalent-circuit diagram for a battery. R_a is the resistance of the electrochemical path including the electrolyte and the separator, R_m is the resistance of the metallic path through the battery including the terminals, electrodes and interconnections, R_i is the contact resistance between the plate or electrode and the electrolyte and C_b is the capacitance of the parallel plates that form the electrodes of the battery.

in the equivalent-circuit [113]. Various equivalent-circuit battery models found in the literature were used to estimate these voltage losses by treating the various sources of loss as resistances in an electrical circuit. Some equivalent-circuit models can be found in [114–119].

The electrochemical impedance spectroscopy (EIS) technique experimentally measures the impedance of an electrochemical system over a range of frequencies to obtain the frequency response of the system. The combination of EIS with the equivalent-circuit models can be used to design and analyse electrochemical systems and stacks with minimal computational effort since they are quick and relatively simple to devise. Such models can form the basis for control algorithms and stack models. In comparison to the detailed models, equivalent-circuit models lack fundamental detail and are not therefore suitable for cell design [120]. Furthermore, there are many difficulties in distinguishing between the various resistances when using EIS [105].

Chapter 3

3 Model Development

A transient, two-dimensional model based on conservation principles, incorporating the fundamental modes of transport and a kinetic model for reactions involving vanadium species, was developed in [37] for the all-vanadium RFB. In this thesis, the model is extended considerably to include an energy balance and gas evolution (with bubble formation), fully coupled to the conservation laws of mass, charge and momentum. Heating by activation losses, electrochemical reaction and ohmic resistance are incorporated. The effects associated with gas (hydrogen and oxygen) evolution on the performance of VRBs are also included in the model. Gas evolving reactions are parasitic, consuming a portion of the current density applied to the cell and, therefore, lowering its efficiency. The bubbles lead to partial occlusion of the liquid electrolyte in the electrode, reducing the active surface area for reaction, the effective diffusion coefficients and the effective ionic and thermal conductivities. In addition, the presence of the bubbles affects the liquid velocity field, further impacting mass transport/transfer; the buoyancy of the bubbles can enhance the flow rate and turbulence can enhance mixing [121].

The formation and effects of gas bubble evolution on planar electrodes, particularly from hydrogen evolution, has been investigated fairly extensively [122–128]. Analytical and numerical models have been developed, notably by Dahlkild and coworkers [129, 130], Ziegler and Evans [126] and Mat and Aldas [131], all based on the multi-phase mixture (often referred to as the 'drift-diffusion') or similar model [132, 133]. The same approach towards bubble formation and gas/liquid transport is adopted in this chapter.

The kinetics associated with oxidation and reduction of vanadium species are known to be highly complex [34,134]. The transport of each species participate in the electrode reactions: V(II), V(III), V(IV), V(V), H_2O, H^+, HSO_4^-, H_2, O_2 and SO_4^-, by diffusion, migration and convection, contributes to the current and affects the

performance. The fullest description of the battery system involves highly nonlinear terms and coefficients in a complex system of partial differential equations (PDE) that couples the fluid dynamics and electrochemical phenomena.

3.1 Model Assumptions

In order to formulate a manageable problem, certain simplifying assumptions are adopted.

1. The dilute-solution approximation is used [13], and the flow is considered laminar and incompressible, due to the fact that the bulk of the electrolyte is water. Laminar flow regime in porous media is valid for low Reynolds number, well within the values of the parameters used in this study with an electrolyte of density $\sim$ 1000 kg m^{-3}, an average pore diameter of 170 μm and electrolyte velocities on the order of a few cm s^{-1}.

2. The overall momentum equation for the gas bubbles and electrolyte is approximated by that of the liquid since the liquid volume fraction and density are much larger than those of the gas bubble.

3. The gas forms spherical bubbles that maintain their shape when detaching from the electrode surface and do not coalesce. [96,125,127,129]. Small bubbles remain spherical as a result of high surface tension and their coalescence can be neglected [135]. This is believed to be a result of repulsive electrical forces acting between the bubbles [136].

4. The gas-phase and liquid-phase pressures are equal, which is a good approximation for non-expanding bubbles [137, 138].

5. The liquid and solid phases in the electrodes attain the same temperature. This assumption is equivalent to an infinite rate of heat transfer between the two phases and, therefore, instant relaxation to the same temperature [95].

6. The volume change resulting from the transfer of water between the electrodes through the membrane over charge-discharge cycles can be neglected but over

very long times would have to be taken into account.

In the general case these assumptions depend primarily on the number of species considered and their relative concentrations. The dilute-solution approximation can be employed in the case of a dominant component, or concentrated solution theory (based on the Maxwell-Stefan equations [139]) for a completely dissociated salt in a binary solution [13].

3.2 Conservation Principles in the Porous Carbon Electrode

The evolved hydrogen and oxygen gases are assumed to generate bubbles in the liquid electrolyte. The bubbles are dispersed, *i.e.* do not form a continuous phase, and move with the flow of the liquid phase (denoted with a subscript 'l'). The volume fraction of the gas bubbles, β_g and the volume fraction of the electrolyte, β_l, in the pore space must satisfy volume conservation:

$$\beta_l + \beta_g = 1 \tag{51}$$

In the multiphase mixture model [133], the mixture density and mixture velocity (velocity of the mass centre), ρ_m and $\vec{u}_m$ are defined as follows:

$$\begin{aligned} \rho_m &= \rho_l \beta_l + \rho_g \beta_g \\ \vec{u}_m &= \frac{\rho_g \beta_g \vec{u}_g + \rho_l \beta_l \vec{u}_l}{\rho_m} \end{aligned} \tag{52}$$

where ρ_l and ρ_g are the liquid and gas phase densities and $\vec{u}_l = (u, v)$ and $\vec{u}_g = (u_g, v_g)$ are the liquid and gas phase velocities, respectively. It is assumed, however, that the liquid phase dominates, so that the overall momentum equation is approximated by that of the liquid phase: The velocity $\vec{u}_l$ is given by Darcy's law for flow through a porous medium, combined with the Kozeny-Carman law for the hydraulic conductivity [140]:

$$\vec{u}_l = -\frac{d_f^2}{K\mu_l}\frac{\epsilon^3(1-\beta_g)^3}{(1-\epsilon(1-\beta_g))^2}\nabla p \tag{53}$$

where ϵ is the porosity of the electrode, $\vec{u}_l$ is the superficial electrolyte velocity, p is the liquid phase pressure, μ_l is the dynamic viscosity of the liquid, d_f is a mean fibre diameter and K is the Kozeny-Carman constant for a fibrous medium. Except in the case of expanding bubbles, where surface tension effects are significant, it is customarily assumed that the gas phase and liquid phase pressures are equal [137, 138]:

$$p_l = p_g = p \tag{54}$$

The overall mixture continuity is replaced with the incompressibility constraint (continuity equation for the liquid phase):

$$\nabla \cdot \vec{u}_l = 0 \tag{55}$$

These assumptions are valid for small gas volume fractions and are consistent with an assumption that the flow is dominated by the flow of the liquid, with departures in the bubble velocity from the bulk velocity induced by drag forces, equal in magnitude to the buoyancy force exerted on the bubbles.

In practise, the liquid phase velocity is eliminated in favour of the pressure using the continuity equation and Darcy's law, and the following parabolic equation is solved:

$$-\nabla \cdot \left(\frac{d_f^2}{K\mu_l}\frac{\epsilon^3(1-\beta_g)^3}{(1-\epsilon(1-\beta_g))^2}\nabla p\right) = 0 \tag{56}$$

The continuous and dispersed phase velocities are related by the slip (relative) velocity $\vec{u}_{\text{slip}} = (u_{\text{slip}}, v_{\text{slip}})$ in the following manner:

$$\vec{u}_{\text{slip}} = \vec{u}_g - \vec{u}_l \tag{57}$$

An equation for the slip velocity can be derived by performing a force balance on a bubble [133] (without turbulence):

$$\frac{1}{2}\rho_l C_D |\vec{u}_{\text{slip}}| \vec{u}_{\text{slip}} = \frac{V_g}{A_g} \nabla p \tag{58}$$

where V_g and A_g are the volume and cross-sectional area of the bubble, respectively, and C_D is the drag coefficient. Equation (58) is derived on the fact that the pressure forces on the bubble are balanced by the viscous drag, *i.e.*, negligible virtual mass, Basset (boundary layer development), interfacial-pressure and lift forces [141]. For spherical bubbles the volume to cross sectional area becomes:

$$\frac{V_g}{A_g} = \frac{2}{3} d_g \tag{59}$$

where d_g is the bubble diameter. For bubbles with diameter less than 2 mm, the following expression (Stoke's law) for the drag coefficient is valid [141, 142]:

$$C_D = \frac{24}{Re_g}; \quad Re_g = \frac{d_g \rho_l |\vec{u}_{\text{slip}}|}{\mu_l} \tag{60}$$

where Re_g is the bubble Reynolds number. Stoke's law is valid for Reynolds number below approximately 1000, well within the regime of gas bubbles in the electrolyte of density ~ 1000 kg m^{-3}, with typical diameters less than 100 μm and velocities on the order of a few cm s^{-1}. The final form of the slip velocity is, therefore:

$$\vec{u}_{\text{slip}} = \frac{d_g^2}{18\mu_l} \nabla p \tag{61}$$

which, using equation (57), yields the gas (bubble) velocity once the continuous phase velocity is known.

To complete the bubble flow model, an equation for the gas phase volume fraction is required. A mass balance, taking into account gas evolution by the electrochemical reaction, gives:

$$\epsilon\rho_g \frac{\partial \beta_g}{\partial t} + \epsilon\rho_g \nabla \cdot (\beta_g \vec{u}_g) = -S_g \tag{62}$$

where S_g is the rate of gas evolution, defined in Table 4 and derived below.

Source term	Positive Electrode	Negative Electrode
S_g (O_2 or H_2 volume fraction equation)	$-M_{O_2}\nabla \cdot \vec{j}_{O_2}/F$	n/a
	n/a	$-M_{H_2}\nabla \cdot \vec{j}_{H_2}/F$
S_2 (V(II) concentration equation)	n/a	$-\nabla \cdot \vec{j}/F$
S_3 (V(III) concentration equation)	n/a	$\nabla \cdot \vec{j}/F$
S_4 (V(IV) concentration equation)	$\nabla \cdot \vec{j}/F$	n/a
S_5 (V(V) concentration equation)	$-\nabla \cdot \vec{j}/F$	n/a
S_{H_2O} (water concentration equation)	$\nabla \cdot \vec{j}/F$	n/a
S_{H^+} (proton concentration equation)	$-2\nabla \cdot \vec{j}/F$	n/a

Table 4: Sources and sinks for the liquid and gas phases in equations (62) and (63a).

Let c_i denote the concentration of species i = 2, 3, 4, 5, H_2O, H^+, HSO_4^-, OH^-, O_2 and H_2 (the notation 2, 3, 4, and 5 are used for the vanadium species: V(II), V(III), V(IV) and V(V), respectively). A volume-averaged mass balance in the porous regions is expressed in the following form:

$$\frac{\partial}{\partial t}\left(\epsilon(1-\beta_g)c_i\right) + \nabla \cdot \vec{N}_i = -S_i \tag{63a}$$

where S_i is the source term for species i, defined in Table 4 and discussed in section 3.6. The concentration flux is given by the Nernst-Planck equation [13, 143] which accounts for charged species transport by diffusion, convection and migration (as discussed in section 2.2):

$$\vec{N}_i = -D_i\epsilon^{3/2}(1-\beta_g)^{3/2}\nabla c_i - \frac{z_i c_i D_i F}{RT}\nabla\phi_e + \vec{u}_l c_i \tag{63b}$$

The diffusion coefficient is subject to a Bruggemann correction [144] to account for the tortuosity of the flow path.

The electrolyte is considered electrically neutral and is, therefore, governed by the condition:

$$\sum_i z_i c_i = 0 \tag{64}$$

At all points, including the boundaries, the ionic and electronic currents satisfy the condition of charge conservation (the charge entering the electrolyte, $\vec{j}_e$, is balanced by the charge leaving the solid phase, $\vec{j}_s$) yields:

$$\nabla \cdot \vec{j}_e + \nabla \cdot \vec{j}_s = 0 \tag{65}$$

The total current density transferred from the solid phase to the electrolyte,

$$\nabla \cdot \vec{j} = \nabla \cdot \vec{j}_e = -\nabla \cdot \vec{j}_s \tag{66}$$

is equal to the net (volumetric) rate of electrochemical reaction (redox reaction + gas evolution reactions) multiplied by Faraday's constant.

Following the usual practise in PEMFC modelling a pseudo-steady state for proton and electron transport is assumed [145–148]. Invoking electroneutrality condition, the total current density in the electrolyte satisfies (applying equations (43) and (44)) :

$$\vec{j} = \sum_i \vec{j_i} = -\sigma_e \nabla \phi_e - F \sum_i z_i D_i \nabla c_i \tag{67}$$

where the effective conductivity, σ_e, is given by:

$$\sigma_e = \frac{F^2}{RT} \sum_i z_i^2 D_i c_i \tag{68}$$

Taking the divergence of equation (67) yields the final form of the equation for the ionic potential:

$$-\nabla \cdot \left(\sigma_e \nabla \phi_e + F \sum_i z_i D_i \nabla c_i \right) = \nabla \cdot \vec{j} \tag{69}$$

The current density $\vec{j}$ has two components, one from the vanadium redox reactions and the second arising from the gas evolution reaction. An expression for $\vec{j}$ is derived below. The electronic potential in the porous carbon electrode is given by Ohm's law:

$$-\sigma_s \nabla^2 \phi_s = -\nabla \cdot \vec{j} \tag{70}$$

where conservation of charge, as expressed by equation (65), is imposed. The effective conductivity of the porous carbon electrode, σ_s, obtained from the value for the solid material, σ_f, subject to a Bruggemann correction:

$$\sigma_s = (1-\epsilon)^{3/2}\sigma_f \tag{71}$$

3.3 Equations in the Membrane

Nafion is a sulfonated tetrafluoroethylene copolymer discovered in the late 1960s by Walther Grot [149]. Nafion's unique ionic properties are a result of incorporating perfluorovinyl ether groups terminated with sulfonate groups onto a tetrafluoroethylene (Teflon) backbone [150–154]. Nafion's superior properties allowed for broad applications, including fuel cells and other electrochemical devices. The high conductivity to cations, high permeability to water and resistance to chemical attack makes Nafion suitable to use as a membrane for proton exchange membrane (PEM) fuel cells to permit hydrogen ion transport while preventing electron conduction.

Microscopic models examine molecular-level and pore-level effects. There have been many microscopic models based on statistical mechanics [155], molecular dynamics [156], and macroscopic phenomena applied to the microscopic structure of the membrane [157]. These models provide some fundamental understanding of processes such as diffusion and conduction in the membrane at pore level but are unsuitable for system-level modelling.

Macroscopic models of Nafion-type membranes are often empirical and focus on describing the transport and relevant parameters of the membrane in a macrohomogeneous fashion. The membrane system is assumed to have three main components: membrane, protons and water, neglecting all other kind of ions in the membrane and assuming no hydrogen or oxygen crossover; such crossover results in only a small inefficiency if the membrane remains intact and does not significantly influence proton or water transport [103]. Weber and Newman [103] developed a model to investigate variations in the Nafion membrane structure with the water content (moles of water per mole of sulfonic acid sites). Increasing the water content led to the formation of micelles in the polymer matrix, connected to each other by a network of open 'channels'. In the physical model of transport in Nafion, there are two separate 'states' of the membrane depending on whether the water at the boundary is in vapour or liquid

form; these are termed vapour-equilibrated or liquid-equilibrated, respectively. The main difference between the two is that, in the vapour-equilibrated membrane the channels are collapsed, while in the liquid-equilibrated membrane they are expanded and filled with water [103]. Transport of proton and water in the membrane is described using formulation of Bernadi and Verbrugge [99, 100], developed for PEMFC applications. The alternative phenomenological model of Springer *et al.* [98] specific to Nafion® is less accurate under liquid-saturated conditions [158]. An electroneutrality condition is enforced, with the fixed charge sites in the membrane structure (sulfonic acid groups in the case of Nafion®) taken as the negatively and positively charged species, respectively. The concentration of water dissolved in the membrane, $c_{\mathrm{H_2O}}$, satisfies the following mass balance, taking into account bulk and dissipative (diffusive) transport:

$$\frac{\partial c_{\mathrm{H_2O}}}{\partial t} - \nabla \cdot (D_{\mathrm{H_2O}} \nabla c_{\mathrm{H_2O}}) + \nabla \cdot (\vec{u}_l c_{\mathrm{H_2O}}) = 0 \tag{72}$$

in which $D_{\mathrm{H_2O}}$ is the effective diffusion coefficient for water through the membrane. The driving forces for the bulk flow are potential and pressure gradients; the liquid velocity $\vec{u}_l$ is given by Schlögl's equation [106]:

$$\vec{u}_l = -\frac{\kappa_\phi}{\mu_{\mathrm{H_2O}}} F c_{\mathrm{H^+}} \nabla \phi_e - \frac{\kappa_p}{\mu_{\mathrm{H_2O}}} \nabla p \tag{73}$$

for electrokinetic permeability κ_ϕ, hydraulic permeability κ_p, water viscosity $\mu_{\mathrm{H_2O}}$, and proton concentration $c_{\mathrm{H^+}}$. An incompressibility condition is used to derive the continuity equation for the liquid water in the membrane equation (55).

From the electro-neutrality condition the proton concentration satisfies:

$$c_{\mathrm{H^+}} = -z_f c_f \tag{74}$$

where c_f is the fixed charge site concentration in the membrane and z_f is the fixed site charge. The value of c_{H^+} is, therefore, constant. Since protons are the only mobile ions, the equation for current conservation can be derived using equation (73) and equation (55):

$$0 = \nabla \cdot \vec{j} = \nabla \cdot \vec{j}_+ = -\frac{F^2}{RT} D_{\mathrm{H}^+} c_{\mathrm{H}^+} \nabla^2 \phi_e \tag{75}$$

where D_{H^+} is the effective diffusion coefficient for the protons. Since the ionic potential satisfies Laplace's equation, $\nabla^2 \phi_e = 0$, the pressure equation reduces to:

$$-\frac{\kappa_p}{\mu_{\mathrm{H_2O}}} \nabla^2 p = 0 \tag{76}$$

3.4 Equations in the Current Collectors

The electronic potential in the current collectors is given by Ohm's law:

$$-\sigma_s \nabla^2 \phi_s = 0 \tag{77}$$

where $\sigma_s = \sigma_{\mathrm{coll}}$ is the electronic conductivity of the collectors. As a reasonable approximation, its value is taken to be constant.

3.5 Pump Approximation and Inlet Conditions

The movement of the electrolyte solution through the electrode and pump alters the concentrations at the inlet boundaries with time. Invoking conservation of volume, the volumetric flow at the outlet boundary, with cross-sectional area $A = L_t L_w$, is $\omega = v_{\mathrm{in}} \epsilon A$, where L_t is the electrode thickness and L_w is the electrode width (see Table 6 in Appendix (A) for values). From the calculated average concentration at the outflow boundaries,

$$c_i^{\text{out}} = \frac{1}{L_t} \int_{y=h} c_i \, dx \tag{78}$$

the inlet concentrations are approximated in the following manner, which assumes instantaneous mixing and negligible reaction in the reservoir of volume V.

The change in number of moles of species i in the reservoir in a time Δt is equal to the difference between the number of moles of species i added to the reservoir and the number of moles of species i leaving the reservoir:

$$\Delta n = c_i^{\text{out}} \omega - c_i^{\text{in}} \omega \tag{79}$$

where c_i^{in} and c_i^{out} are the electrodes inlet and outlet concentrations of species i, respectively. The change in concentration of species i in the reservoir is, therefore,

$$\frac{\Delta c_i^{\text{in}}}{\Delta t} = \frac{\Delta n}{V} \tag{80}$$

In the limit $\Delta t \to 0$,

$$\frac{dc_i^{\text{in}}}{dt} = \frac{\omega}{V} \left(c_i^{\text{out}} - c_i^{\text{in}} \right); \quad c_i^{\text{in}}(0) = c_i^0 \tag{81}$$

where c_i^0 is the initial concentration of species i (water, vanadium species, protons and anions). The total volume of electrolyte on each side of the battery, V_T, is the sum of the electrode and the reservoir volumes, $\epsilon h A$ and V respectively, where h is the height of the porous carbon electrode. It is assumed that the volume in the pipes is negligible.

3.6 Reaction Kinetics

The reversible redox reactions taking place on the solid surfaces of the porous carbon electrode are described using the Butler-Volmer expression for the transfer current densities, j_+ and j_-, in the positive and negative electrode compartments, respectively (as discussed in section 2.1.3). The precise multi-step reaction mechanism is not known, but it has previously been demonstrated that the reversible redox features are well captured by the Bultler-Volmer formulae given below [37]:

$$\begin{aligned} j_+ &= \nabla \cdot \vec{j}_+ \\ &= a\epsilon(1-\beta_g)Fk_1 \left(c_4^s\right)^{\alpha_{a,+}} \left(c_5^s\right)^{\alpha_{c,+}} \left[\exp\left(\frac{F\alpha_{c,+}\eta_+}{RT}\right) - \exp\left(-\frac{F\alpha_{a,+}\eta_+}{RT}\right)\right] \\ j_- &= \nabla \cdot \vec{j}_- \\ &= a\epsilon(1-\beta_g)Fk_2 \left(c_3^s\right)^{\alpha_{a,-}} \left(c_2^s\right)^{\alpha_{c,-}} \left[\exp\left(\frac{F\alpha_{c,-}\eta_-}{RT}\right) - \exp\left(-\frac{F\alpha_{a,-}\eta_-}{RT}\right)\right] \end{aligned} \tag{82}$$

for the positive and negative electrodes, respectively. In these expressions j_+ and j_- are the volumetric current density in the positive and negative electrode compartments, respectively, a is the specific active surface area of the porous carbon electrode (solid-liquid interface); k_1 and k_2 are the standard rate constants for reactions (1) and (2), respectively; $\alpha_{a,\pm}$ and $\alpha_{c,\pm}$ are the anodic and cathodic transfer coefficients, respectively (one electron transfer); and η_+ and η_- are the overpotentials in the positive and negative electrode, respectively. The porosity of the electrode is multiplied by a factor $1-\beta_g$ to give the volume fraction of the liquid phase, taking into account the presence of the bubbles. The common assumption $\alpha_{a,\pm} = \alpha_{c,\pm} = 1/2$ is made. The overpotentials are defined as follows:

$$\eta_\pm = \phi_s - \phi_e - E_{0,\pm} \tag{83}$$

where $E_{0,+}$ and $E_{0,-}$ are the open circuit potentials for reactions (1) and (2), re-

spectively, estimated from Nernst equations (the pH dependence for reaction (1) is neglected for simplicity):

$$\begin{aligned} E_{0,+} &= E'_{0,+} + \frac{RT}{F}\ln\left(\frac{c_5}{c_4}\right) \\ E_{0,-} &= E'_{0,-} + \frac{RT}{F}\ln\left(\frac{c_3}{c_2}\right) \end{aligned} \tag{84}$$

The formal potentials $E'_{0,+}$ and $E'_{0,-}$ are given in Table 8 in Appendix (A).

The quantities c_i^s are vanadium-species concentrations at the liquid-solid interfaces in the porous regions, which are generally different from the bulk values due to additional transport resistance (from the bulk solution to the interfaces). They can be related to the bulk values, c_i, by approximately balancing the rate of reaction with the rate of diffusion of reactant to (or from) the electrode surface at steady state (as discussed in section 2.1.2). For this purpose it is convenient to re-write the Butler-Volmer terms in a form that indicates linear dependence on the surface concentrations (using equation (84) in equation (82)). For the positive electrode during charge, the balance is:

$$\begin{aligned} \frac{D_4}{d_f}(c_4 - c_4^s) &= \epsilon(1-\beta_g)k_1\left(c_4^s e^{F(\phi_s-\phi_e-E'_{0,+})/(2RT)} - c_5^s e^{-F(\phi_s-\phi_e-E'_{0,+})/(2RT)}\right) \\ \frac{D_5}{d_f}(c_5 - c_5^s) &= -\epsilon(1-\beta_g)k_1\left(c_4^s e^{F(\phi_s-\phi_e-E'_{0,+})/(2RT)} - c_5^s e^{-F(\phi_s-\phi_e-E'_{0,+})/(2RT)}\right) \end{aligned} \tag{85}$$

where d_f is the average fibre diameter in the porous carbon electrode and D_i is the diffusion coefficient for species i in solution. The quantities D_i/d, measuring the rate of reactant delivery to or from the surfaces by diffusion from the bulk, are the piston velocities (in $\mathrm{m\,s^{-1}}$). Using equation (82) and solving the resulting simultaneous equations for c_4^s and c_5^s gives:

$$
\begin{aligned}
c_4^s &= \frac{c_4 + \epsilon(1-\beta_g)k_1 e^{-F(\phi_s-\phi_e-E'_{0,+})/(2RT)}\left(\dfrac{c_4}{\gamma_5}+\dfrac{c_5}{\gamma_4}\right)}{1+\epsilon(1-\beta_g)k_1\left(\dfrac{1}{\gamma_5}e^{-F(\phi_s-\phi_e-E'_{0,+})/(2RT)}+\dfrac{1}{\gamma_4}e^{F(\phi_s-\phi_e-E'_{0,+})/(2RT)}\right)} \\
c_5^s &= \frac{c_5 + \epsilon(1-\beta_g)k_1 e^{F(\phi_s-\phi_e-E'_{0,+})/(2RT)}\left(\dfrac{c_4}{\gamma_5}+\dfrac{c_5}{\gamma_4}\right)}{1+\epsilon(1-\beta_g)k_1\left(\dfrac{1}{\gamma_5}e^{-F(\phi_s-\phi_e-E'_{0,+})/(2RT)}+\dfrac{1}{\gamma_4}e^{F(\phi_s-\phi_e-E'_{0,+})/(2RT)}\right)}
\end{aligned}
\tag{86}
$$

where $\gamma_4 = D_4/d$ and $\gamma_5 = D_5/d$ are the piston velocities. Similar equations apply to the species at the negative electrode.

There are several known side reactions, notably the evolution of oxygen in the positive electrode [34, 35] (equation (3)) and evolution of hydrogen in the negative electrode [34, 36] (equation (4)). The volumetric current density associated with the gas evolution reactions (3) and (4), which takes place predominantly during charge at the positive/negative electrode, is approximated by the Tafel relationship:

$$
j_{\mathrm{g}} = \nabla \cdot \vec{j}_{\mathrm{g}} = \pm a\epsilon(1-\beta_g) j_{0,\mathrm{g}} \exp\left(\pm\frac{F\alpha_{\mathrm{g}}\eta_{\mathrm{g}}}{RT}\right) \tag{87}
$$

where $j_{0,\mathrm{g}}$ and η_{g} are the exchange current density and overpotential for the gas evolution reactions, respectively:

$$
\eta_{\mathrm{g}} = \phi_s - \phi_e - E_{0,\mathrm{g}} \tag{88}
$$

in which $E_{0,\mathrm{g}}$ is the formal potential of the reaction. The dependence on water concentration is not incorporated since its value changes by small amounts, relative to the initial concentration.

The total current density in the negative electrode is the sum of the hydrogen gas evolution and redox reaction current densities

$$\nabla \cdot \vec{j} = \nabla \cdot \vec{j}_{-} + 2\nabla \cdot \vec{j}_{\mathrm{H_2}} \tag{89}$$

which is used in equation (69) and equation (70).

Similarly, the total current density in the positive electrode is the sum of the oxygen gas evolution and redox reaction current densities

$$\nabla \cdot \vec{j} = \nabla \cdot \vec{j}_{+} + 4\nabla \cdot \vec{j}_{\mathrm{O_2}} \tag{90}$$

which is used in equation (69) and equation (70).

3.7 Energy Balance

The energy balance takes into account heat conduction, convective heat transport and heat generation by reaction and ohmic resistance. As a reasonable first approximation it is assumed that the liquid and solid phases in the electrodes attain the same temperature. The energy balance is thus:

$$\frac{\partial}{\partial t}(\overline{\rho C_p} T) + \nabla \cdot (\vec{u}\rho_l C_l T) - \overline{\lambda}\nabla^2 T = \sum_k Q_k \tag{91}$$

where ρ_l and C_l are the density and specific heat capacity of the liquid, respectively, $\overline{\lambda}$ is the volume-averaged thermal conductivity and $\overline{\rho C_p}$ is the volume-averaged thermal capacitance given by:

$$\overline{\lambda} = \begin{cases} \epsilon\beta_l\lambda_l + \epsilon\beta_g\lambda_g + (1-\epsilon)\lambda_{\text{elec}}, & \text{Porous electrode} \\ \lambda_{\text{mem}} & \text{Membrane} \\ \lambda_{\text{coll}} & \text{Current collectors} \end{cases} \tag{92}$$

$$\overline{\rho C_p} = \begin{cases} \epsilon\beta_l\rho_l C_l + \epsilon\beta_g\rho_g C_g + \rho_{\text{elec}}C_{\text{elec}}(1-\epsilon), & \text{Porous electrode} \\ \rho_{\text{mem}}C_{\text{mem}} & \text{Membrane} \\ \rho_{\text{coll}}C_{\text{coll}} & \text{Current collectors} \end{cases}$$

where C_j and λ_j are the specific heat capacities (at constant pressure) and thermal conductivities of the individual phases: the subscripts 'g', 'l', 'elec', 'mem' and 'coll' refer to the gas phase, liquid electrolyte, electrode, membrane and current collector, respectively. The thermal property values used in the simulations are given in Table 10 in Appendix (A). The value of the specific heat capacity of the membrane was also estimated by the value for water (since the bulk of the membrane is liquid water). The thermal conductivity and specific heat capacity of the external environment are approximated by values for air.

In the membrane, the only form of heat transport is conduction. The heat generation terms Q_k are defined in Table 5: they represent heating by activation losses, reaction and ohmic resistance. As a simplification, the ohmic heating in the electrolyte solution in the electrodes is based only on the term containing σ_e in equation (67), which would be expected to be the main contributor. This permits a simpler form for the corresponding Q_k value.

In Table 5, $-\Delta S_{0,1}$ is the standard entropy associated with the reaction in the positive electrode and $-\Delta S_{0,2}$ is the standard entropy associated with the negative-electrode reaction. These standard reaction entropies are given by:

$$\Delta S_{0,j} = \left(\sum_{\text{products}} S_{0,j}^{\text{products}} \right) - \left(\sum_{\text{reactants}} S_{0,j}^{\text{reactants}} \right) \tag{93}$$

Term	Membrane	+ve electrode	-ve electrode	Current collector
Q_{act}	0	$\eta_1 \nabla \cdot \vec{j}_1$	$\eta_2 \nabla \cdot \vec{j}_2$	0
Q_{rev}	0	$\Delta S_1 T \nabla \cdot \vec{j}_1 / F$	$-\Delta S_2 T \nabla \cdot \vec{j}_2 / F$	0
Q_{ohm}	$\sigma_{\text{mem}}^{\text{eff}} \lvert\nabla \phi_e\rvert^2$	$\sigma_s^{\text{eff}} \lvert\nabla \phi_s\rvert^2 + \sigma_e^{\text{eff}} \lvert\nabla \phi_e\rvert^2$	$\sigma_s^{\text{eff}} \lvert\nabla \phi_s\rvert^2 + \sigma_e^{\text{eff}} \lvert\nabla \phi_e\rvert^2$	$\sigma_{\text{coll}} \lvert\nabla \phi_s\rvert^2$

Table 5: Sources and sinks for the energy equation (91). They are, from top to bottom, heating by activation losses, electrochemical reaction and ohmic resistance.

where $S_{0,j}^{\text{products}}$ ($S_{0,j}^{\text{reactants}}$) are the standard entropies of formation of the products (reactants) in reactions ($j = 1, 2$ and 3). Their values at 298.15 K are listed in Table 11 in Appendix (A). For each reaction j, the standard reaction entropy is related to the standard Gibbs free energy change of the reaction, $\Delta G_{0,j}$, and the standard enthalpy change of reaction, $\Delta H_{0,j}$, by the thermodynamic relation:

$$\Delta G_{0,j} = \Delta H_{0,j} - T \Delta S_{0,j} \tag{94}$$

Using equation (94) and the relation $\Delta G_{0,j} = -nFE_{0,j}$, where $E_{0,j}$ is the standard potential of reaction j, the temperature dependence of $\Delta S_{0,j}$ is obtained:

$$-nF \frac{\partial \Delta E_{0,j}}{\partial T} = \frac{\partial \Delta G_{0,j}}{\partial T} = \Delta S_{0,j} \tag{95}$$

The standard potentials $E_{0,1}$, $E_{0,2}$ and E_{0,O_2} are functions of temperature. The measured temperature dependence can be found in [159]:

$$\begin{aligned} E_{0,1} &= E_1^0 - 9 \times 10^{-4} \times (T - 298.15) \\ E_{0,2} &= E_2^0 + 1.5 \times 10^{-3} \times (T - 298.15) \\ E_{0,\text{O}_2} &= E_{\text{O}_2}^0 - 8.5 \times 10^{-4} \times (T - 298.15) \end{aligned} \tag{96}$$

where E_1^0 , E_2^0 and $E_{O_2}^0$ are the standard potentials at $T = 298.15$ K for reactions (1), (2) and (3), respectively.

The reaction constants, k_1 and k_2 are also temperature-dependent. They can be written in Arrhenius form as follows [160]:

$$\begin{aligned} k_j &= k_{\text{ref,j}} \exp\left(-\frac{\Delta G_{0,j}}{R}\left[\frac{1}{T_{\text{ref,j}}} - \frac{1}{T}\right]\right) \\ &= k_{\text{ref,j}} \exp\left(\frac{nFE_{0,j}}{R}\left[\frac{1}{T_{\text{ref,j}}} - \frac{1}{T}\right]\right) \end{aligned} \tag{97}$$

for $j = 1, 2$. $\Delta G_{0,j} = -nFE_{0,j}$ is the standard Gibbs free energy change for the respective reaction and the constant $k_{\text{ref,j}}$ is the values of k_i at a reference temperature $T_{\text{ref,j}}$.

Similarly, the oxygen evolution exchange current density, j_{0,O_2}, dependence on temperature is given by:

$$\begin{aligned} j_{0,O_2} &= j_{0,(O_2,\ \text{ref})} \exp\left(-\frac{\Delta G_{0,O_2}}{R}\left[\frac{1}{T_{\text{ref}}} - \frac{1}{T}\right]\right) \\ &= j_{0,(O_2,\ \text{ref})} \exp\left(\frac{nFE_{0,(O_2,\ \text{ref})}}{R}\left[\frac{1}{T_{\text{ref}}} - \frac{1}{T}\right]\right) \end{aligned} \tag{98}$$

3.8 Initial and Boundary Conditions

For the discussion on the boundary conditions, Figure 1 is recalled. At the interfaces between the membrane and porous carbon electrode regions the species fluxes (excluding protons and water) and electron flux are considered to be negligibly small. At all external boundaries except at the inlets and outlets the same conditions applies to the species fluxes:

$$\vec{N_i} \cdot \vec{n} = 0 \quad \begin{cases} x = x_1,\ x = x_4 \\ x = x_2,\ x = x_3 \text{ (except water/protons)} \\ y = 0,\ y = h \text{ (except inlet/outlet)} \end{cases} \tag{99}$$

$$\nabla\phi_s \cdot \vec{n} = 0 \quad \begin{cases} x = x_2,\, x = x_3 \\ y = 0, y = h \end{cases} \tag{100}$$

The proton flux at the interfaces between the current collectors and porous carbon electrode is zero, and similarly at all external boundaries in the membrane:

$$\begin{gathered} -\nabla \cdot \left(\sigma_e \nabla\phi_e + FA \sum_i z_i D_i \nabla c_i \right) \cdot \vec{n} = 0 \quad x = x_1,\, x = x_4 \\ -\nabla\phi_e \cdot \vec{n} = 0 \quad y = 0,\, y = h \text{ (membrane)} \end{gathered} \tag{101}$$

At all boundaries of the domain of integration of the pressure equation (except at the inlets and outlets) a Neumann condition is applied:

$$\nabla p \cdot \vec{n} = 0 \quad \text{(except inlets/outlets)} \tag{102}$$

At the inlets, the reactants (including protons) and water enter with a prescribed bulk velocity and concentrations that depend on the pump rate:

$$c_i = c_i^{\text{in}}(t) \quad v_y = v_{\text{in}} \quad \text{(inlets)} \tag{103}$$

At the outlets, the liquid pressure is prescribed and all diffusive fluxes except that for pressure are set to zero (fully developed flow condition):

$$\nabla c_i \cdot \vec{n} = 0; \quad p = p_{\text{out}} \quad \text{(outlets)} \tag{104}$$

Along the electrode/current collector interfaces a no-slip condition is enforced on the

liquid velocity:

$$\vec{u} = 0; \quad x = x_1,\, x = x_4 \tag{105}$$

At the outlet, the gas phase flows outwards with the gas velocity negating the need for a boundary condition. At the inlet it is assumed that the electrolyte is free of bubbles, yielding the condition:

$$\beta_g = 0; \quad y = 0 \tag{106}$$

The boundary conditions on the electronic potential depend on whether the battery is operated in potentiostatic or galvanostatic mode. For the present galvanostatic case the current is assumed to enter or leave uniformly through the current collectors, manifested through the following flux conditions (during charge):

$$-\sigma_{\text{coll}} \nabla \phi_s \cdot \vec{n} = \begin{cases} -\dfrac{I_{\text{app}}}{A}; & x = x_1 \\ \dfrac{I_{\text{app}}}{A}; & x = x_4 \end{cases} \tag{107}$$

where I_{app} is the current and A is the projected area to which the current is applied (the area of the current collector/porous electrode interface). For discharge conditions the signs are reversed.

Consistent initial conditions are prescribed for the concentrations and potentials as follows:

$$\begin{aligned} &c_i(t=0) = c_i^0; \quad \phi_s(t=0) = E_{0,+}(t=0); \quad \phi_e(t=0) = 0; \quad \text{Positive electrode} \\ &c_i(t=0) = c_i^0; \quad \phi_s(t=0) = E_{0,-}(t=0); \quad \phi_e(t=0) = 0; \quad \text{Negative electrode} \end{aligned} \tag{108}$$

For the temperature, a combination of boundary conditions is considered for the external surfaces. The default boundary condition is a zero heat flux (corresponding to adiabatic conditions), except at the inlets and outlets:

$$-\overline{\lambda}\nabla T \cdot \vec{n} = 0 \tag{109}$$

A non-zero heat flux at the current collector surfaces, $x = 0$ and $x = x_5$ (corresponding to cooling or heating as a consequence of a fixed external temperature) is investigated in section 4.4 :

$$-\overline{\lambda}\nabla T \cdot \vec{n} = \frac{\lambda_{\text{air}} Nu}{h}(T - T_a) \tag{110}$$

where T_a is the (fixed) temperature of the environment, λ_{air} is the thermal conductivity of the surrounding fluid (taken to be air), h is the electrode height and Nu is the Nusselt number associated with the heat transfer.

The temperature at the inlets is given separately as:

$$T = T^{\text{in}} \tag{111}$$

where T^{in} is defined below. At the outlets the conductive heat flux is zero.

The initial temperature is uniform throughout the cell:

$$T(t = 0) = T_0 = T^{\text{in}} \tag{112}$$

3.9 Numerical Details and Parameters

3.9.1 Parameters

In the experiments, the cell voltage is measured from the potential difference across the test cell, *i.e.*, with conditions pertaining to the outlets. In the simulations, the cell voltage was measured with respect to the potentials at the intersections between the current collectors and electrodes along the outlet, $y = h$ in Figure 1. In the simulations, as in the experiments, cut-off values for the open-circuit voltage of 1.5 V during charge and 1.3 V during discharge were set. The cell was maintained at OCV for 120 s between consecutive charge and discharge phases.

The default set of parameter values for the simulations is given in Appendix (A). These values were used unless otherwise stated. The current collector properties were based on values for stainless steel. Where available, values for Sigratherm® GFA5 were used for the porous carbon electrode. The quoted[1] resistivity of Sigratherm® GFA5 is anisotropic, approximately 3.5 Ωmm in the transverse direction and 2 Ωmm in the longitudinal direction. These values were averaged to give an isotropic resistivity value. The average pore diameter of the porous carbon foam or felt electrodes is typically in the range (100−800) μm [161]. Two reported values for the Sigratherm family of electrodes are 152 μm [162] by Vatistas *et al.* and 172 μm [163] by Carta *et al.* . In the absence of an exact value for GFA5, the value reported by Carta *et al.* was used. The bubble diameter depends on various factors, including the electrolyte composition, current density and flow rate. A wide range of diameter values has been reported [122, 125, 126], from 25 μm to 100 μm. In this thesis, a range of bubble diameter are considered.

The rate constant for the reaction at the positive electrode was determined by Gattrel *et al.* [34], while the rate constant for the negative electrode reaction was derived through a fitting procedure in [37]. Diffusion coefficients for the reactants through the electrolyte were determined by Yamamura *et al.* [164]. Literature values for the H_2 evolution rate on bare carbon electrodes, particularly the Sigratherm family, were found to be scarce. Values of the H_2 evolution exchange current density, j_{0,H_2},

[1] www.sglcarbon.com.cn/gs/pdf/weichfilz_e.pdf. Last accessed 30 May 2009.

the O_2 evolution exchange current density, j_{0,O_2} and the transfer coefficient, α_{H_2} and α_{O_2} were initially taken from [35], for bare reticulated vitreous carbon. The value of $j_{0,H_2} = 2 \times 10^{-4}$ A cm^{-2} and $j_{0,O_2} = 1 \times 10^{-9}$ A cm^{-2}, however, lead to non-physical values for the H_2 and O_2 volume fraction, which reached unity in a short period of time in many calculations. In order to achieve reasonable results approximately 10 % for the volume fraction of gas, a value of $j_{0,H_2} = 1.4 \times 10^{-9}$ A m^{-2} and $j_{0,O_2} = 1 \times 10^{-9}$ A m^{-2} were instead used.

The membrane parameter values were based on water. In particular, the following phenomenological relationship for the diffusion coefficient of water was used [165]:

$$D_{H_2O} = 4.17 \times 10^{-8} \lambda (1 + 161 e^{-\lambda}) \exp\left(-\frac{2436}{T}\right) \quad \text{in m}^2\ \text{s}^{-1} \tag{113}$$

Here, $\lambda = 22$ is the water content of a liquid-saturated membrane. The initial proton concentration was set equal to the fixed charged site concentration in the membrane, c_f, and the initial concentration of the bisulfate ions HSO_4^- was assumed to be equal to that of the protons. The initial concentrations of the vanadium species were based on a 5 % initial state of charge. The initial concentration of SO_4^{2-} ions was then determined by the condition of electroneutrality (equation (64)).

The cell voltage can be decomposed into several components, representing the various resistances in the cell as given by equation (15). The majority of the components in this equation were explicitly included in the model but in order to match the experimental results, it was found necessary to include an additional lumped resistance. The fitting procedure in the base case (a charge-discharge of 63 min with an electrolyte flow rate of, $\omega = 1$ mL s^{-1}, reactant concentration of, $c_3^0 = c_4^0 = 1080$ mol m^{-3}, an operating temperature of, $T_0 = 298$ K, porosity of, $\epsilon = 0.68$, an average bubble diameter of, $d_g = 50$ μm, a fibre diameter of, $d_f = 172$ μm and an applied current of, $I_{\text{app}} = 10$ A) yielded a value of 131 mV. All cell voltage curves were shifted vertically downwards by this value. The origin of this lumped parameter is likely to be contact resistance, although mass-transfer resistance in the tubing, stagnant regions in the electrode and leaks could also play a role. Relatively minor differences between

the simulation and experimental results were still seen, and these can be attributed to the same causes. The primary aim, however, is to capture the correct qualitative trends with the fewest fitting parameters.

3.9.2 Numerical Implementation

The modelling process consists of six main steps in COMSOL Multiphysics® package.

1. Drawing the model geometry based on a two-dimensional slice as depicted in Fig 1.

2. Selecting the appropriate application mode: PDE general-form for potentials, the liquid pressure and temperature, the convection and diffusion form for V (II), V (III), V (IV), V (V), H_2O and H^+ concentrations.

3. Setting up the subdomain equations and boundary conditions.

4. Meshing the geometry by creating a free mesh consisting of triangular elements.

5. Solving the non-linear model using the backward Euler method for 4100 s with a maximum time step of 25 s.

6. Postprocessing the results.

The methodology used to develop and solve the model is illustrated in Figure 8. It consisted of:

- Consideration of different parameters and operating conditions, *e.g.* applied current density, power rating, operating temperature, species concentration and electrolyte velocity.

- Evaluation of mass transport and reaction kinetics.

- Estimation of the variations in concentrations, overpotentials, current densities, temperature, gas volume fraction, gas velocity, electrolyte velocity, the slip velocity, the ionic and electronic potentials and the cell voltage by solving the system of differential equations using the COMSOL Multiphysics® package.

- Postprocessing the results by using the MATLAB® R2009a package.

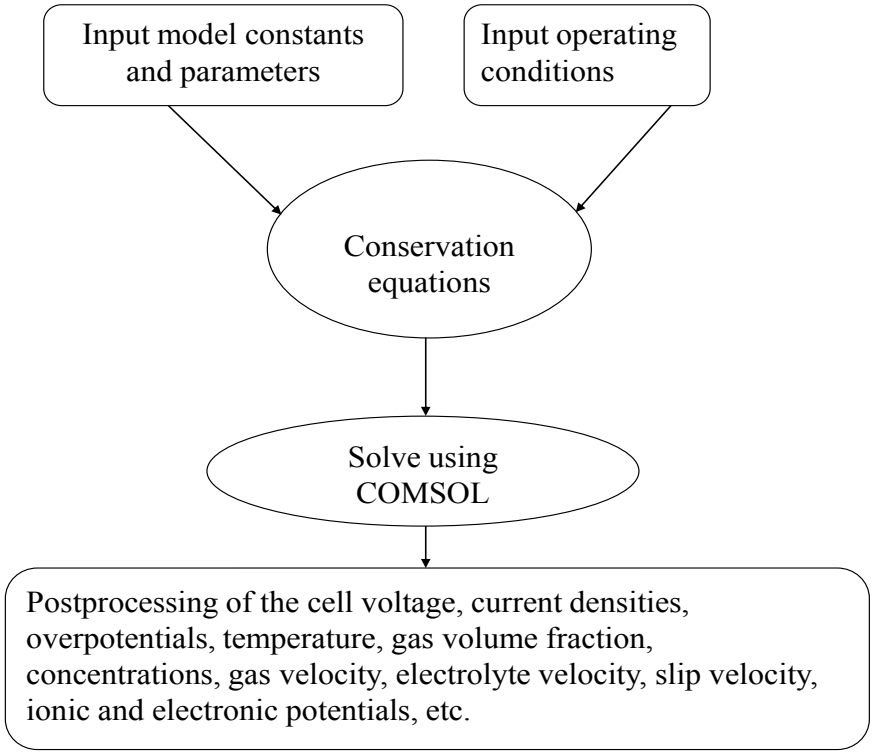

Figure 8: Flowchart depicting the simulation of the VRFB.

The implemented COMSOL Multiphysics® package is based on the finite-element method; a quadratic basis was used in all of the simulations, together with a minimum of 2548 elements and a maximum of 7256 elements, based on grid dependency checks that compared the times to SOC for successively more refined meshes. This measure was found to be a good indicator of convergence. The relative error tolerance was set to 1×10^{-6}. The base case calculation took 33 min on a Viglen Intel(R) xeon(R) CPU, 64-bit desktop with 4 Gb RAM. The long times can be attributed to the large number of elements required to obtain converged solutions with acceptable levels of accuracy. At the end of the charge period, 2 min of operation at zero current followed by discharge were simulated in each calculation.

3.10 Experimental Details

Experiments were carried out at the electrochemical engineering laboratory (led by M.J. Watt-Smith, a member of the Energy Technology Research Group).

The body of the redox flow battery was constructed in polyvinyl chloride polymer. The positive and negative electrode compartments were 10 cm x 10 cm x 0.4 cm in size. The compartments, which were divided by a Nafion® 115 cation exchange membrane, were filled by porous and layered carbon felt electrodes (Sigratherm® GFA5). The effective volumetric porosity of the felt electrodes was 68±7 %.

Electrolyte was circulated through each half-cell compartment through a glass reservoir (volume 250 mL, with a nitrogen gas atmosphere) and peristaltic pump circuit. The electrolyte contained a total vanadium concentration in the range 1.0−1.5 mol dm^{-3}, as a V(III) and V(IV) mixture, in 4.0 mol dm^{-3} H_2SO_4, at a temperature of 297±2 K. The volumetric flow rate was in the range 60−180 cm^3 min^{-1}, corresponding to a mean linear flow velocity of 0.37−1.1 cm s^{-1} through the carbon felt electrodes.

The cell was charged and discharged at a constant current (typically in the range 2−10 A, corresponding to a current density of 20−100 mA cm^{-2}, based on the projected area of each electrode). Typically, the charge and discharge parts of a cycle were each 30−40 minutes in duration. Up to 30 cycles were used.

An in-house personal computer and interface was used to monitor cell voltage. In addition, a cell (divided by a Nafion® 115 cation exchange membrane) was used to monitor the cell open-circuit voltage between carbon rod electrodes (8 mm diameter carbon rods). This cell effectively measured the differential redox potential between the half-cell electrolytes, which provided an indication of the state of charge. The cell current was also monitored.

Chapter 4
Effects of Temperature on the Battery Performance

4 Non-Isothermal Modelling

The effects temperature have on the model developed in chapter three are discussed below by ignoring the gas evolution effects, *i.e.* setting β_g=0 in equations (63a and 63b). Simulations are performed to study the effects of temperature variations on the charge/discharge characteristics of the cell. The roles played by heat losses, the electrolyte flow rate and the magnitude of the applied current on the charge/discharge behaviour and the distribution of temperature are investigated. The implications of localised heating and membrane degradation are discussed.

For a constant-current charge/discharge process, the voltage and coulombic efficiencies are defined as:

$$\xi_v = \frac{\int_{t_c}^{t_d} E_{\text{cell}}\, dt}{\int_0^{t_c} E_{\text{cell}}\, dt} \times 100\% \quad \text{and}$$
$$\xi_c = \frac{t_d}{t_c} \times 100\% \tag{114}$$

respectively, where t_c is the time to charge and t_d is the time to discharge.

4.1 Variations in the System Temperature

Figure 9 shows the evolutions of the cell voltage during a charge/discharge cycle for three initial temperatures, $T_0 = 303$ K, 318 K and 333 K. The other parameter values are as in Appendix (A). In all three cases the system is assumed to be adiabatic. In each case, charging was terminated at the equivalent SOC, which was estimated by the residual V(III) reactant concentration:

$$\mathrm{SOC} = 1 - \frac{c_{3,\mathrm{av}}}{c_3^0} \tag{115}$$

A zero SOC corresponds to no charge and unity to a fully charged. The quantity $c_{3,\mathrm{av}}$ is the average V(III) concentration in the negative half-cell, including both the electrode and reservoir volumes. It is calculated from a volume average. A value of SOC = 0.7 was used in all calculations in this chapter. The charge time was within 5 seconds of 1752 seconds for each of the three temperatures.

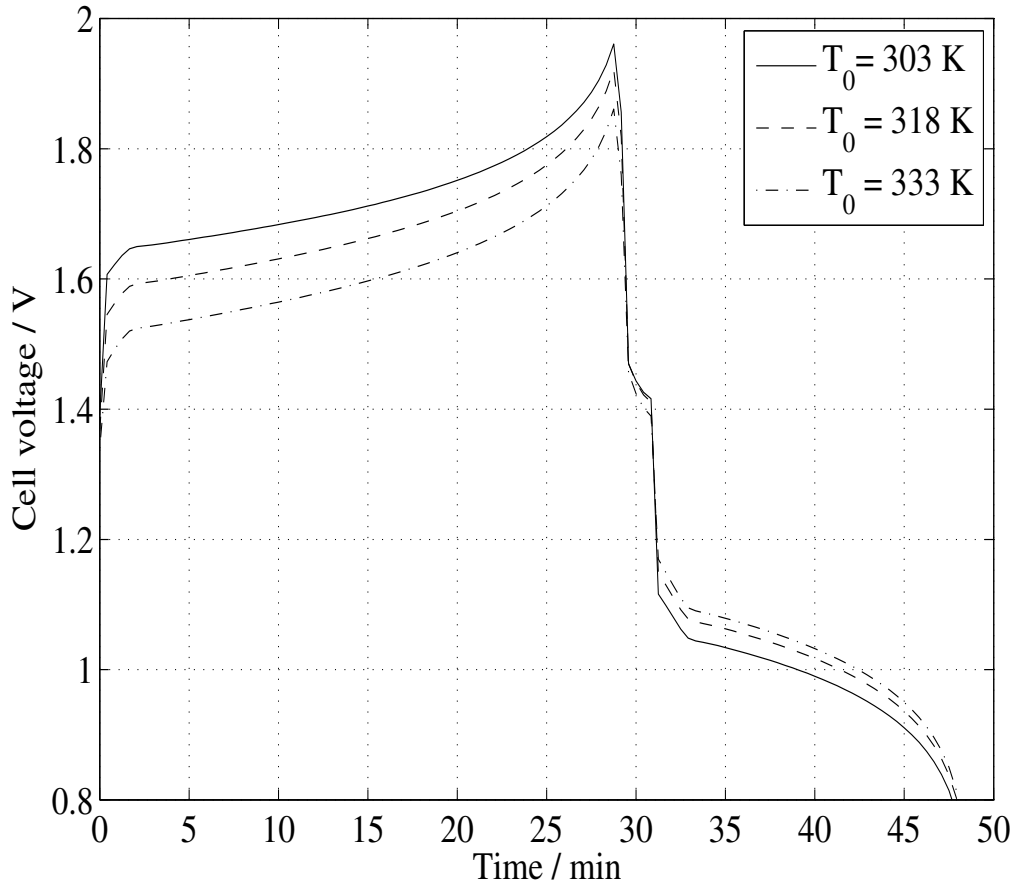

Figure 9: Simulated charge-discharge curves for three initial temperatures: $T_0 = 303$ K, 318 K and 333 K. The times to charge and discharge are approximately 29.2 min and 45.2 min in each case, respectively. Two minutes at zero current were simulated before discharge. The other parameter values are given in Appendix (A).

The capacity of the battery (proportional to time since the discharge current is constant) increases mildly with increased temperature. During charge, there is a clear decrease in the cell voltage as the temperature is raised and during discharge the cell voltage is increased, *i.e.*, the deviation of the cell voltage from the equilibrium value decreases as the temperature is increased. The decreasing deviation of the cell voltage from the equilibrium value with increasing temperature is due to several factors. Firstly, the equilibrium potentials given by equation (84) and equation (96) decrease in magnitude for fixed initial concentrations of the reactants. This is evident from the downward trend in the cell voltage value near $t = 0$ in Figure 9 as the temperature is increased. An increased temperature also increases the rate constants, k_i, given in equation (97).

Figure 10 shows contours of the overpotential in the negative electrode at the end of the charge phase for the two cases $T_0 = 303$ K and $T_0 = 333$ K in Figure 9. As the temperature increases, the magnitude of the overpotential decreases, by more than 10 mV at the intersection between the outlet and the membrane, $x = 10.3$ mm, $y = 10$ cm. For lower temperatures, the decreased reaction rate constant leads to an increase in the magnitude of the overpotential, as is seen from the Butler-Volmer equation (82). Indeed, Figure 11 shows that the V(III) concentration values at the end of charge for the two temperatures are very close. The other vanadium species concentrations also change little as the temperature is varied. Along any horizontal line, the depletion of V(III) during charge increases as the current collector surface ($x = 6.3$ mm) is approached - the current enters along this surface. The overpotential drops sharply in order to maintain the current, particularly in the upper half of the electrode as the membrane ($x = 10.3$ mm) is approached.

Near $x = 6.3$ mm, $y = 10$ cm, reaction is severely limited by the low V(III) concentration, so that the drop in overpotential is less steep. Note that the potential-dependent exponential in the Butler-Volmer equations would tend to decrease with an increase in temperature, for a fixed potential, which would tend to require an increase in the magnitude of the overpotential. The increase in the reaction constant, however, dominates this effect, ultimately leading to less negative overpotentials. The

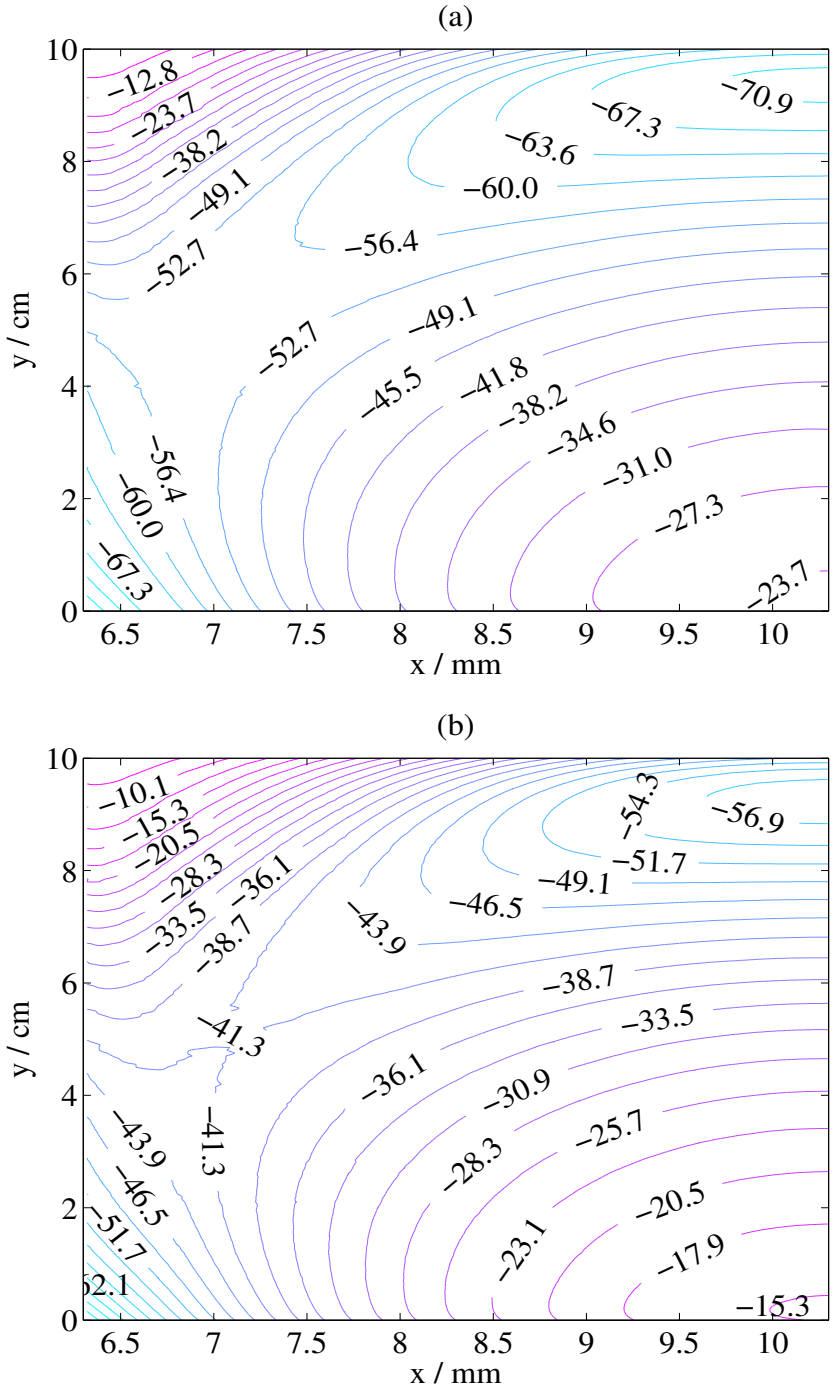

Figure 10: Contours of overpotential in the negative electrode, η_1 (in mV) towards the end of the charge phase, $t = 28.75$ min, for the two cases: (a) $T_0 = 303$ K and (b) $T_0 = 333$ K in Figure 9. The other parameter values are given in Appendix (A). The left-hand boundary ($x = 6.3$ mm) corresponds to the intersection of the electrode with the current collector (x_1) in Figure 1 and the right-hand boundary ($x = 10.3$ mm) to the intersection of the electrode with the membrane (x_2) in Figure 1.

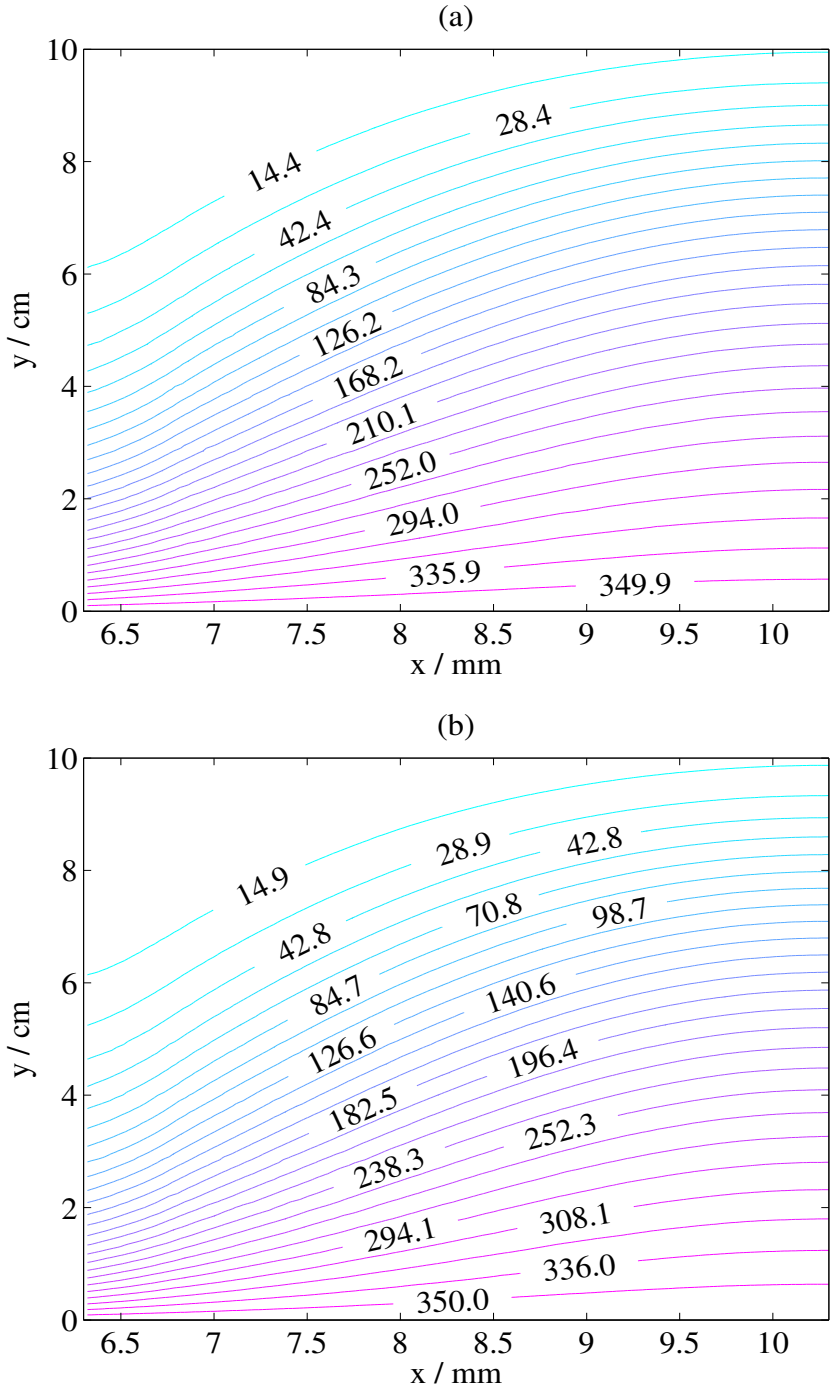

Figure 11: Contours of V(III) concentration in the negative electrode (in mol m^{-3}) towards the end of the charge phase, $t = 28.75$ min for the two cases: (a) $T_0 = 303$ K and (b) $T_0 = 333$ K in Figure 9. The other parameter values are given in Appendix (A). The left-hand boundary ($x = 6.3$ mm) corresponds to the intersection of the electrode with the current collector and the right-hand boundary ($x = 10.3$ mm) to the intersection of the electrode with the membrane.

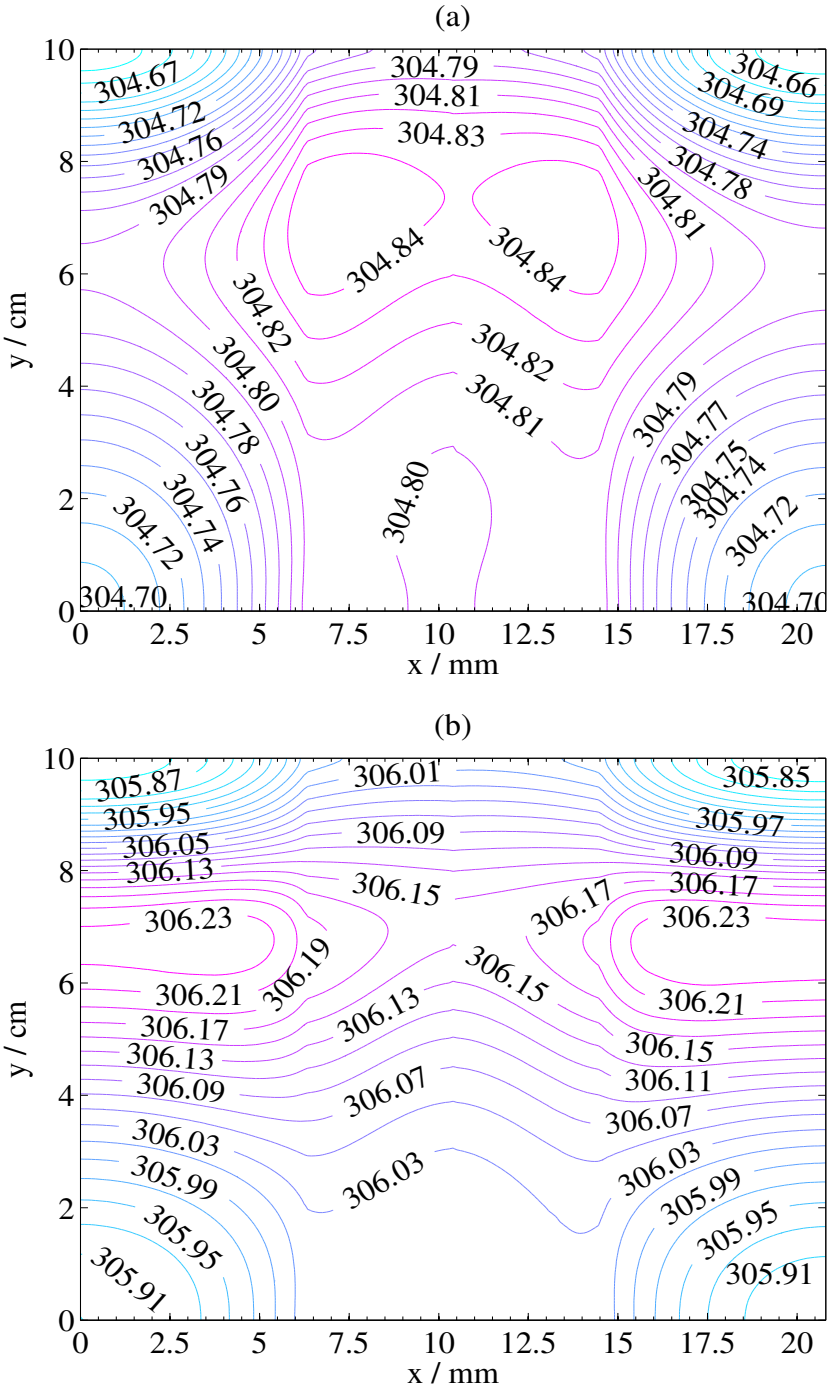

Figure 12: Contours of the temperature (in K) in the entire cell: (a) towards the end of charge $t = 28.75$ min and (b) towards the end of discharge $t = 45$ min. These plots correspond to the curve at $T_0 = 303$ K in Figure 9. The other parameter values are given in Appendix (A). The various regions are as follows: current collector ($0 \leq x < 6.3$), negative electrode ($6.3 \leq x < 10.3$), membrane ($10.3 \leq x < 10.5$), positive electrode ($10.5 \leq x < 14.5$) and current collector ($14.5 \leq x \leq 20.8$).

decreased magnitude of the overpotential at 333 K (in both the positive and negative electrodes) will lead to decreased rates of side reactions such as oxygen evolution (in the positive electrode) and hydrogen evolution (in the negative electrode) towards the end of charge. This suggests that in order to avoid gas evolution, the target SOC should be reduced if the temperature of the system is decreased.

Contour plots of the temperature in the cell at the end of the charge and discharge cycles for the case $T_0 = 303$ K are given in Figure 12. Contours at the other temperatures are qualitatively the same, with roughly equal temperature rises in each case. The various regions are as follows (in mm): current collector ($0 \leq x < 6.3$); negative electrode ($6.3 \leq x < 10.3$); membrane ($10.3 \leq x < 10.5$); positive electrode ($10.5 \leq x < 14.5$); and current collector ($14.5 \leq x \leq 20.8$). At the end of the charge phase, the cell temperature is almost 2 K higher than the initial temperature and by the end of the discharge phase, the temperature rise is approximately 3 K throughout. This represents a significant level of heating (due primarily to the ohmic resistances in equation (91)) in a relatively short period of time. These results demonstrate that over the course of several hours, the heat, if not allowed to dissipate, would rise to unacceptable levels.

4.2 Variations in the Applied Current

Figure 13 shows simulated charge-discharge curves for three applied currents: $I_{\text{app}} = 5$ A, 10 A and 20 A. The sign of the current is reversed during discharge. In all cases the initial temperature is $T_0 = 303$ K. The other parameter values are as in Appendix (A). The charge times are defined by an equivalent SOC for each applied current value (the same SOC value used in the calculations in Figure 9). There is clearly a dramatic increase in the maximum cell voltage as the applied current is increased. At $I_{\text{app}} = 20$ A, the magnitudes of the overpotentials in the both electrodes rise well above the values required for the onset of hydrogen and oxygen evolution, well before the final SOC is reached. The coulombic efficiency is substantially increased as the magnitude of the applied current is reduced; fixing the end of discharge as the point at which the cell voltage reaches a value of 0.8 V, the coulombic efficiency for $I_{\text{app}} = 10$

A is 57 % and for $I_{\text{app}} = 5$ A, it is 81 %. At low loads and over several cycles, self-discharge engendered by reactant crossover may lower the coulombic efficiency.

Figure 14 shows contours of the overpotential and V(III) concentration in the negative electrode at the end of the charge phase for the case $I_{\text{app}} = 5$ A. Comparing the V(III) concentration in Figure 14 (a) with the contour plots in Figure 11 for $I_{\text{app}} = 10$ A and $T_0 = 303$ K reveals that the concentration is more uniform (less stratified in the y direction) at the lower value of I_{app}. In particular, V(III) is not entirely depleted locally at $x = 6.3$ mm, $y = 10$ cm, as was the case for $I_{\text{app}} = 10$ A. As a consequence, the overpotential is more evenly distributed, which is seen by comparing Figure 14 (b) and 10 (a). Moreover, the magnitudes of the overpotentials are markedly lower for $I_{\text{app}} = 5$ A, primarily as a result of the lower rates of reaction required to maintain a lower current.

Figure 15 shows contours of the temperature towards the end of discharge for the two cases $I_{\text{app}} = 5$ A and 20 A depicted in Figure 13. While the increase in temperature for the lower value of I_{app} is approximately 2 K, the increase for $I_{\text{app}} = 20$ A is as high as 12 K. This is despite a much shorter timescale; 20 min compared with 100 min. Local maxima in the temperature develop in both current collectors at a height of approximately 3 cm. The distribution of temperature is determined largely by the gradients in electronic and ionic potential, since the majority of heating arises from ohmic resistance (see the form in Table 5). Figure 16, showing contours of the heat source Q_{ohm} (in kW m^{-3}) for (a) the current collector adjacent to the negative electrode and (b) the negative electrode at $t = 18.75$ min for the case $I_{\text{app}} = 20$, demonstrates the influence of the potential gradients on the temperature distribution (the contours in the current collector adjacent to the positive electrode have a similar-laterally inverted-shape). A local maximum in Q_{ohm} develops in the negative electrode in the vicinity of the inlet, $x = 6.3$ mm, $y = 0$ cm, which outweighs the local maximum in the current collector, at $y \approx 5$ cm. This local maximum in the electrode is determined primarily by the gradient of the electronic potential in the x direction, $\partial\phi_s/\partial x$; at the higher current density, the greater non-uniformity in the V(II) reactant concentration on discharge leads to larger potential gradients in the electrode, which

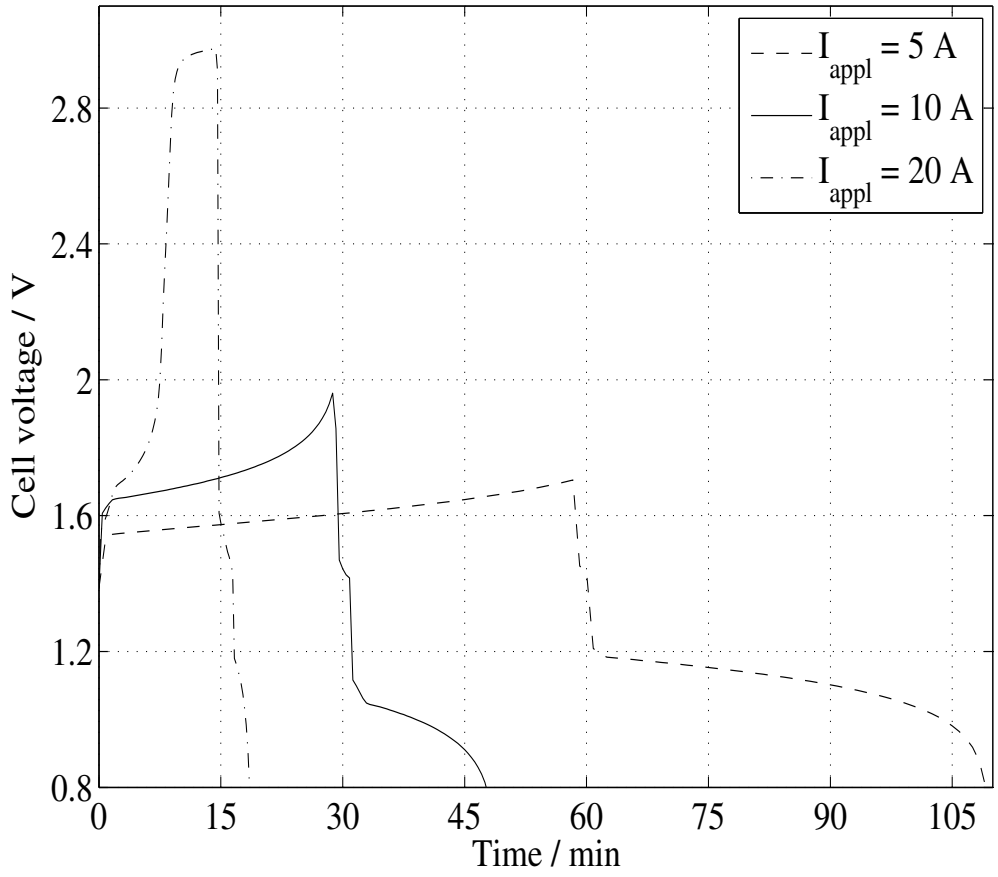

Figure 13: Simulated charge-discharge curves for three applied currents (the sign of the current is reversed during discharge): $I_{\text{app}} = 5$ A, 10 A and 20 A. The charge times are defined by an equivalent state of charge for each applied current value. The other parameter values are given in Appendix (A).

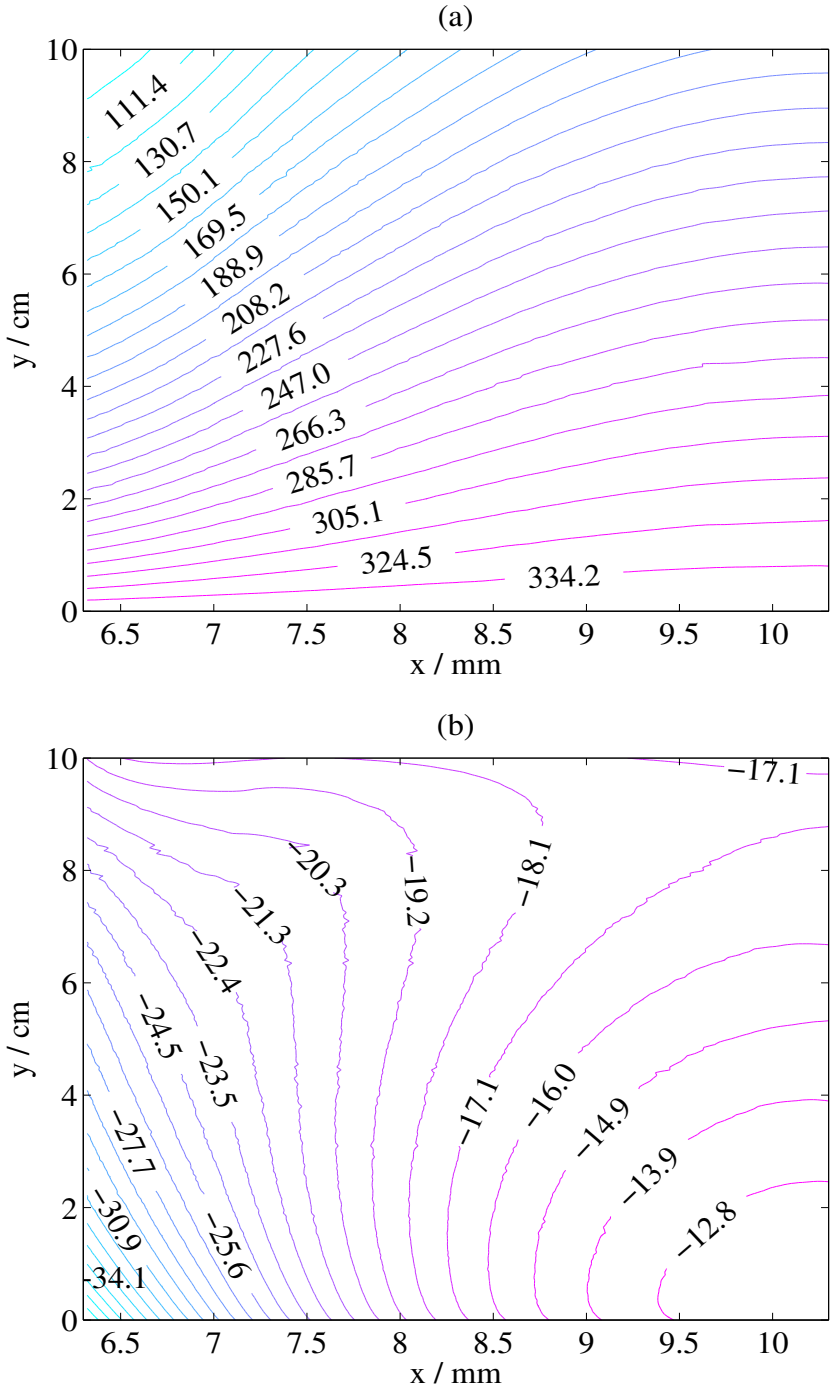

Figure 14: Contours of (a) V(III) concentration and (b) overpotential in the negative electrode towards the end of the charge phase, $t = 58.33$ min, for the case $I_{\text{app}} = 5$ A in Figure 13. The other parameter values are given in Appendix (A). The left-hand boundary ($x = 6.3$ mm) corresponds to the intersection of the electrode with the current collector and the right-hand boundary ($x = 10.3$ mm) to the intersection of the electrode with the membrane.

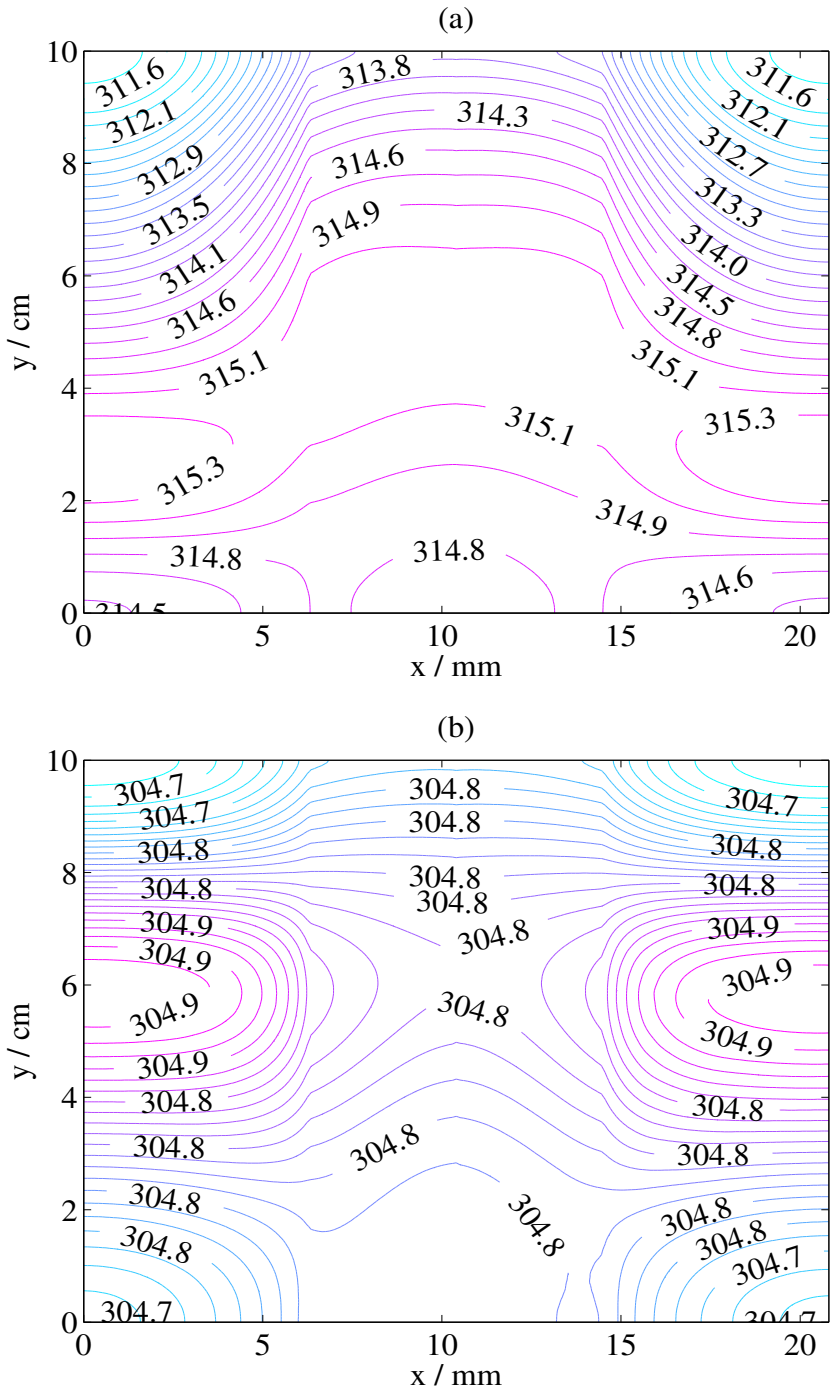

Figure 15: Contours of the temperature (in the entire cell) towards the end of discharge for the case (a) $I_{\text{app}} = 20$ A, $t = 18.75$ min; and (b) $I_{\text{app}} = 5$ A, $t = 109.17$ min. The other parameter values are given in Appendix (A). The various regions are as follows: current collector ($0 \leq x < 6.3$), negative electrode ($6.3 \leq x < 10.3$), membrane ($10.3 \leq x < 10.5$), positive electrode ($10.5 \leq x < 14.5$) and current collector ($14.5 \leq x \leq 20.8$).

exert a stronger influence over the temperature profile.

4.3 Variations in the Electrolyte Flow Rate

The flow (pump) rate of the electrolyte is an important control mechanism in the operation of a vanadium redox flow battery system. At low flow rates the electrolyte is not efficiently circulated and stagnant regions can form in the electrode. If the flow rate is too high, there is a risk of leakage, or the performance gains may not be sufficient to outweigh the extra power required to pump the electrolyte through the system at a faster rate. Figure 17 compares the charge/discharge curve for the base case with $\omega = 0.25$ mL s^{-1} with that for $\omega = 0.5$ mL s^{-1}.

As the flow rate is increased the coulombic efficiency markedly improves. A higher flow rate reduces the contact time for reaction in the electrode, which leads to a longer time for the exit solution to reach the desired state of charge, [37]. The V(III) concentration is more uniform (the reactant in the electrode is replenished from the reservoir more rapidly) leading to greater uniformity in the overpotential and transfer current density. As a result, the cell voltage at the end of charge is lower for $\omega = 0.5$ mL s^{-1}.

Figure 18 shows the temperature distribution near the end of discharge for $\omega = 0.5$ mL s^{-1}, corresponding to the calculation in Figure 17. Comparing Figure 18 with Figure 12 (b), the difference in the temperature rise between the two flow rates is small. However, the distribution of the temperature is more uniform at the higher flow rate, which is clearly a result of the increased convective transport of heat from the electrodes to the reservoirs, in the absence of changes in other parameters. Furthermore, the localised maxima in temperature seen in Figure 12 are not as pronounced. Over long timescales, this suggests that the likelihood of localised heating is higher at low flow rates where concentrations, reactions, and, importantly, potentials can be highly stratified.

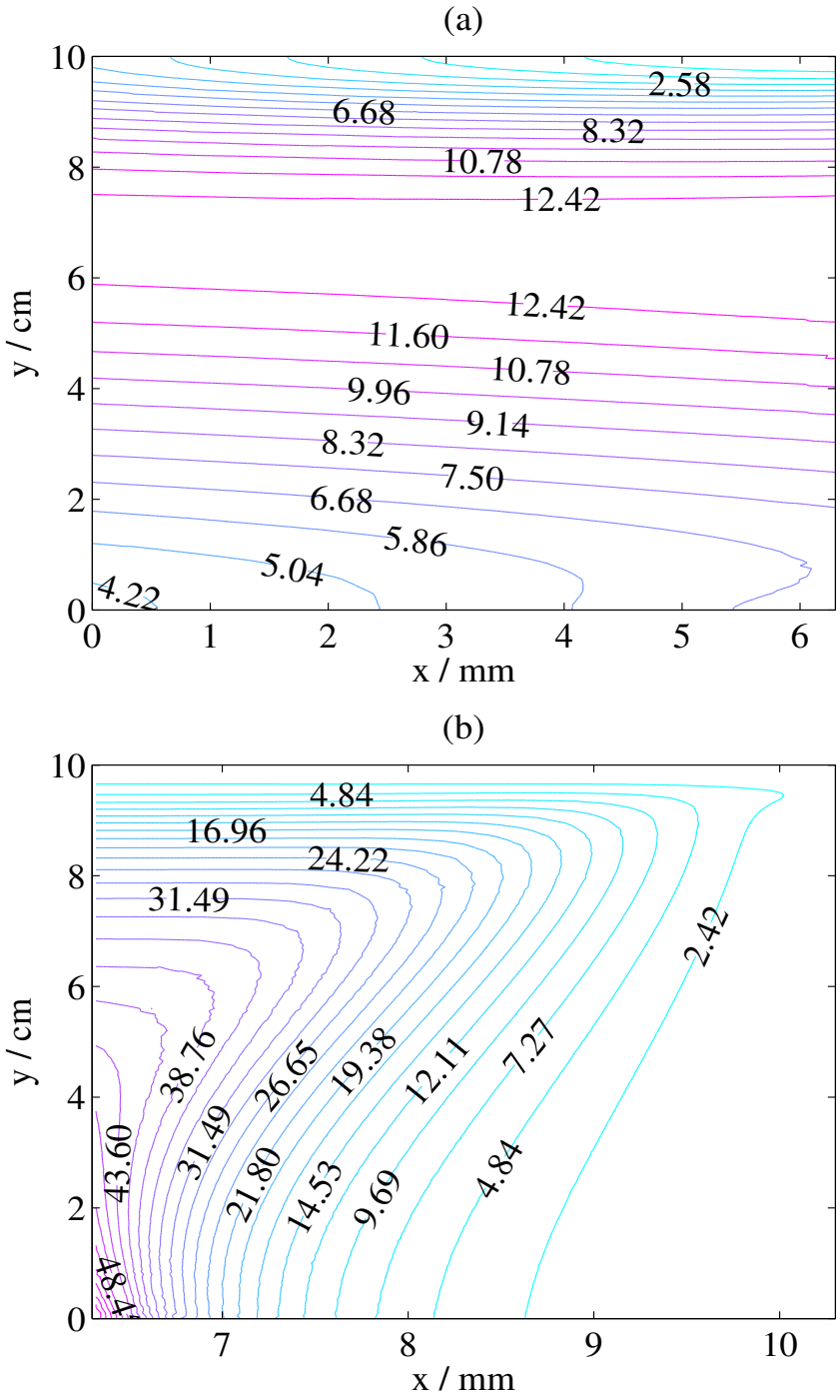

Figure 16: Contours of the heat source Q_{ohm} (in kW m^{-3}) at the end of the discharge phase, $t = 18.75$ min, in (a) the current collector adjacent to the negative electrode and (b) the negative electrode. These plots correspond to the case $I_{\text{app}} = 20$ A in Figure 13. The other parameter values are given in Appendix (A). $x = 0$ mm defines the intersection between the current collector and external environment and $x = 10.3$ mm defines the intersection between the electrode ad the ion-exchange membrane.

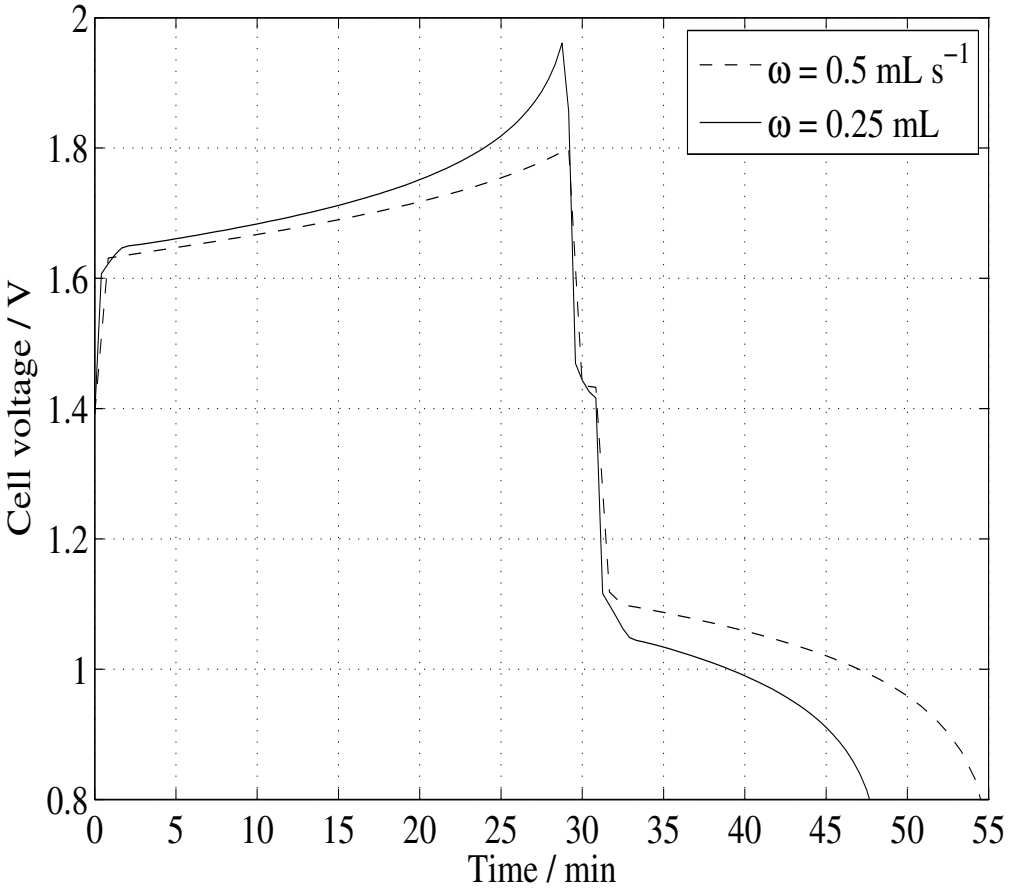

Figure 17: Simulated charge-discharge curves for two flow rates: $\omega = 0.5$ mL s^{-1} and the base case of $\omega = 0.25$ mL s^{-1}. The other parameter values are given in Appendix (A).

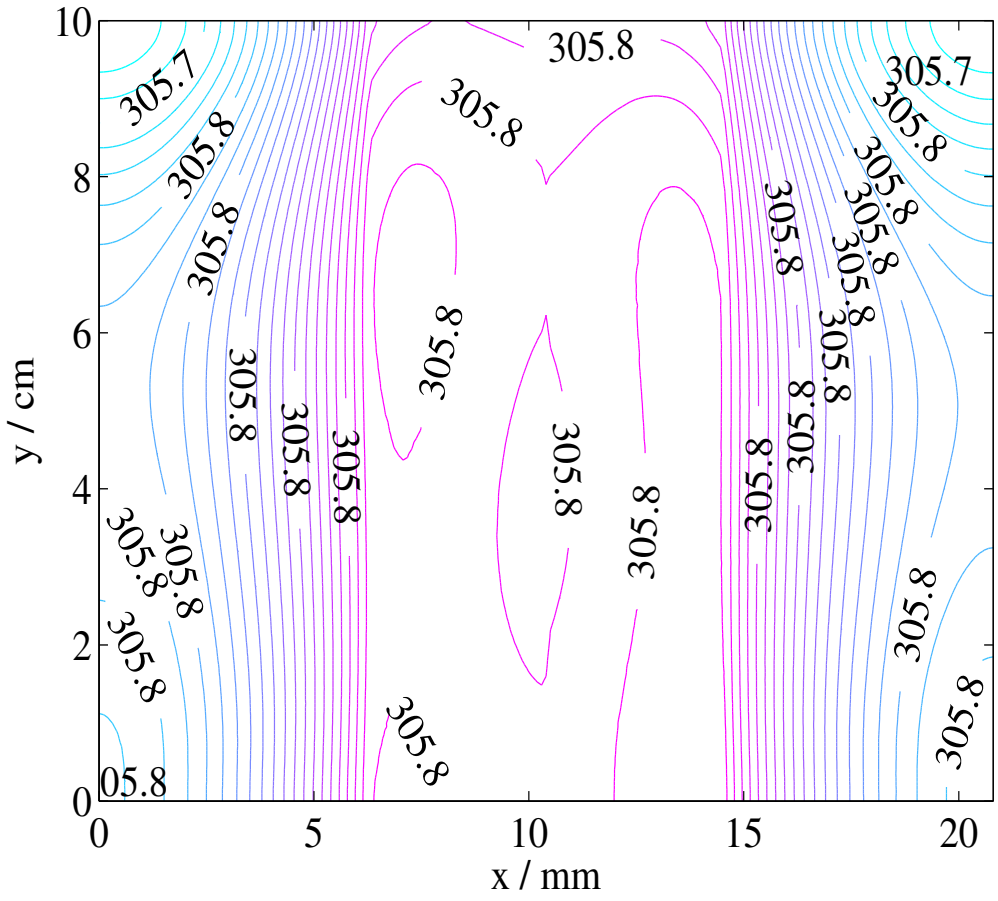

Figure 18: The temperature distribution in the entire cell near the end of discharge for a flow rate of $\omega = 0.5$ mL s^{-1}, corresponding to the calculation shown in Figure 17. The other parameter values are given in Appendix (A). The various regions are as follows: current collector ($0 \leq x < 6.3$), negative electrode ($6.3 \leq x < 10.3$), membrane ($10.3 \leq x < 10.5$), positive electrode ($10.5 \leq x < 14.5$) and current collector ($14.5 \leq x \leq 20.8$).

4.4 Effects of Heat Loss to the Environment

Thus far it has been assumed that the system is adiabatic. It has been demonstrated above that if heat is not allowed to escape from the system, the temperature can rise to unacceptable levels over relatively short periods of time, particularly for high loads. Figure 19 demonstrates the effect of a finite rate of heat loss to the external environment. The adiabatic case corresponds to $T_0 = 303$ K with all other parameters as in Appendix (A). The other two curves correspond to heat loss by natural convection with a Nusselt number of 10 and forced convection with $Nu = 50$. A value of $Nu = 0$ corresponds to the adiabatic condition and a value of $Nu = \infty$ to a fixed temperature $T = T_a$ at the boundary.

Without loss of generality, the heat loss was applied only to the outermost surfaces of the current collectors in the x direction, $x = 0$ mm and $x = 20.8$ mm. For the non-adiabatic cases, heat loss lowers the temperature in the electrodes, which leads to a gradual increase in the cell voltage during charge and a lower cell voltage during discharge; during charge, the standard potentials increase with a decreasing temperature and the slower reaction rates at lower temperatures require a compensating increase in the activation overpotentials. The more heat is lost (Nusselt number is increased) the greater the deviation of the cell voltage from the equilibrium value. Figure 20 (a) shows contours of the overpotential in the negative electrode towards the end of the charge phase, $t = 28.75$ min, for the case $Nu = 50$. A comparison with Figure 10 (a) shows the greater polarisation with heat loss included. The evolution of the average value of the rate constant in the positive electrode, $\langle k_1 \rangle$ is shown in Figure 20 (b). By the end of discharge, the value has decreased by almost an order of magnitude. The decrease in $\langle k_2 \rangle$ is less pronounced due to the smaller activation energy (Gibbs free energy change), but is still substantial.

Figure 21 shows the distribution of temperature in the entire cell towards the end of discharge, $t = 49.17$ min, for the two cases (a) $Nu = 10$ and (b) $Nu = 50$. In both cases, the fall in temperature is greatest at the boundaries where heat is lost ($x = 0$ mm and $x = 20.8$ mm). While the gradients in temperature in the x direction are relatively large, there is an almost uniform distribution of temperature along any

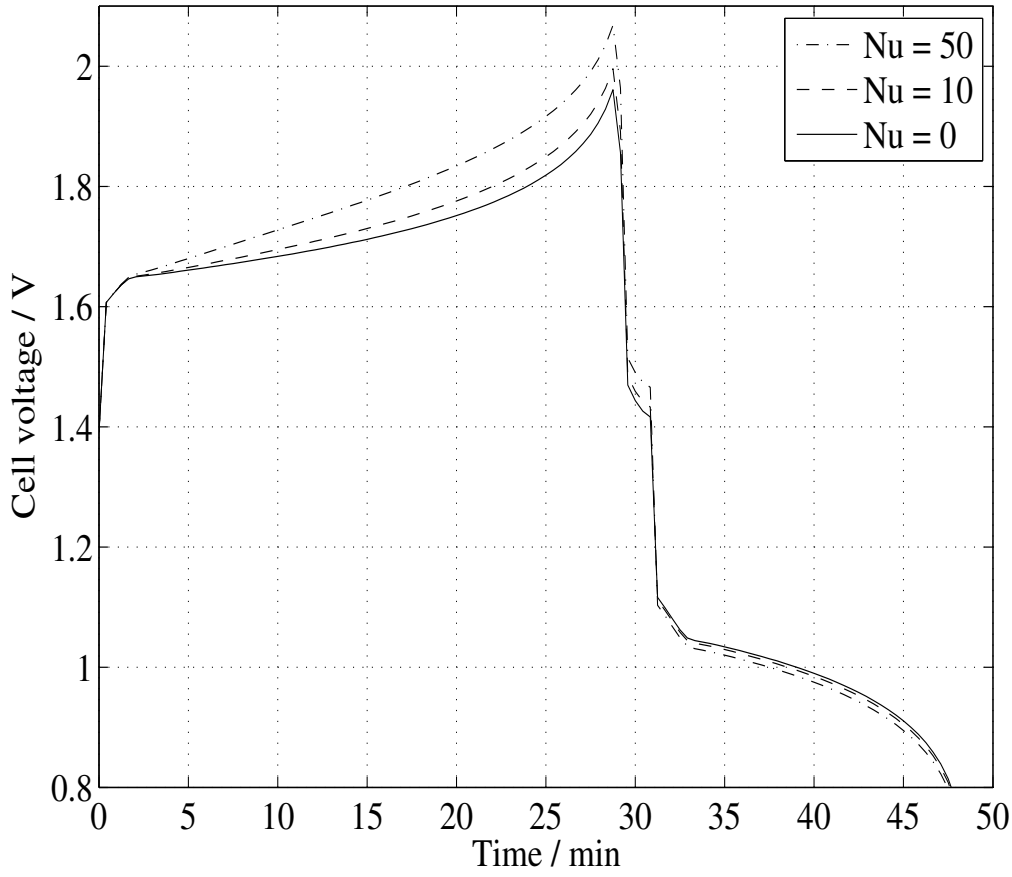

Figure 19: The effect of a finite rate of heat loss to the external environment. The three cases $Nu = 0$, $Nu = 10$ and $Nu = 50$ represent adiabatic conditions, free convection and forced convection, respectively. The other parameter values are given in Appendix (A).

vertical line.

4.5 Conclusions

Due to non-uniformities in the reactant concentrations and, therefore, potentials and transfer current densities, local maxima in temperature can develop. A large electrolyte flow rate, combined with regulation of the external temperature, could be used to avoid such hotspots by keeping the temperature distribution uniform. Moreover, such high flow rates increase the coulombic efficiency of the cell.

The value of the applied current for charge and discharge plays a crucial role in heat generation. The amount of heat generated and the timescale of the temperature rise do not increase linearly with the current. Regions of high temperature can form rapidly in the current collectors and electrodes due to large gradients in the electronic potential.

Heat loss can have a significant effect on the charge/discharge behaviour and temperature distribution of the cell. In the examples presented, cell performance was shown to deteriorate markedly, with increases in the magnitudes of the overpotentials in both electrodes and, therefore, an increased likelihood of gas evolution. These results further highlight the need for an effective heat management strategy to maintain the desired cell temperature, particularly in environments where the temperature is not optimal.

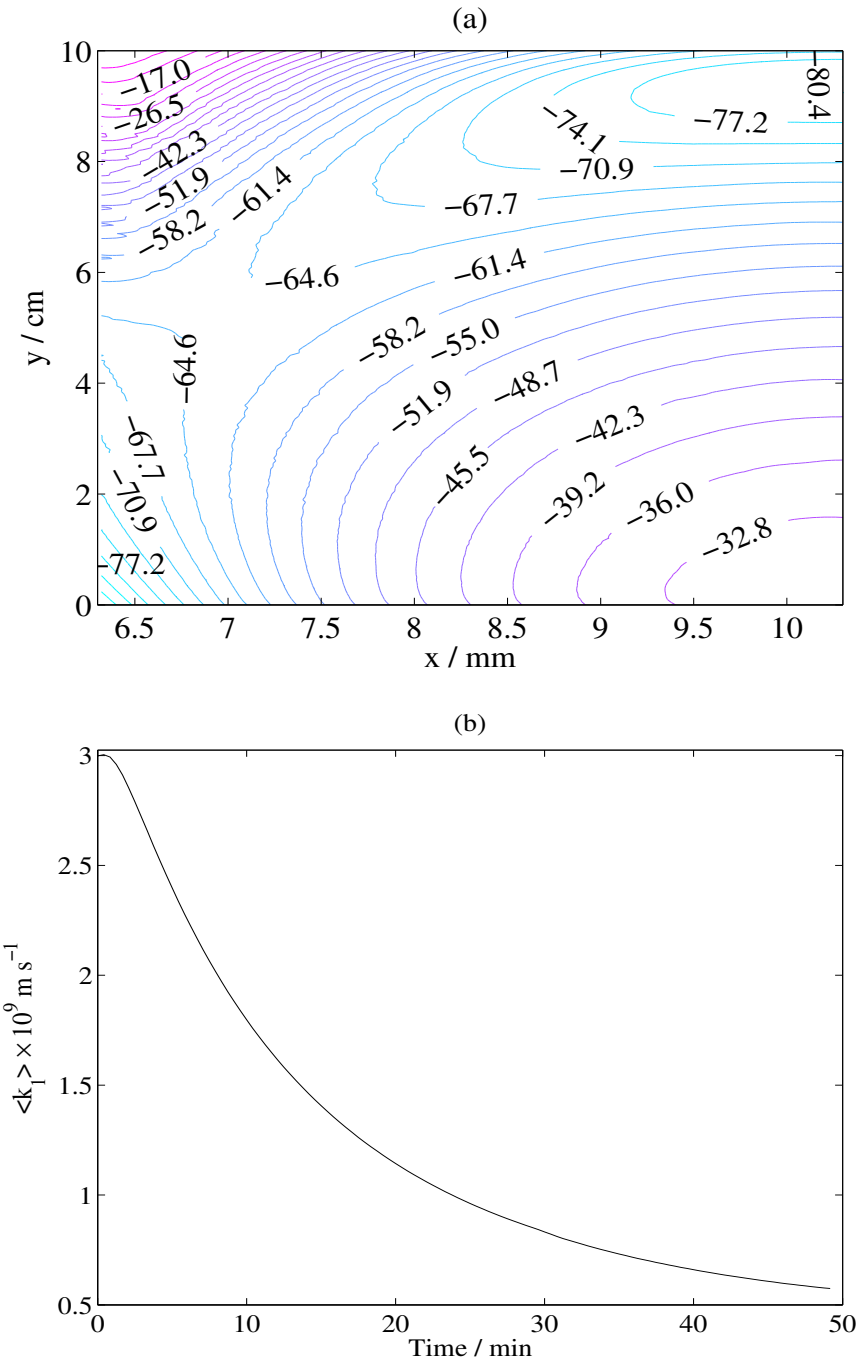

Figure 20: (a) Contours of overpotential in the negative electrode towards the end of the charge phase, $t = 28.75$ min, for the case $Nu = 50$ in Figure 19. The other parameter values are given in Appendix (A). The left-hand boundary ($x = 6.3$ mm) corresponds to the intersection of the electrode with the current collector and the right-hand boundary ($x = 10.3$ mm) to the intersection of the electrode with the membrane. (b) The evolution of the spatially averaged value of the rate constant, k_1 for the positive electrode reaction in the case $Nu = 50$.

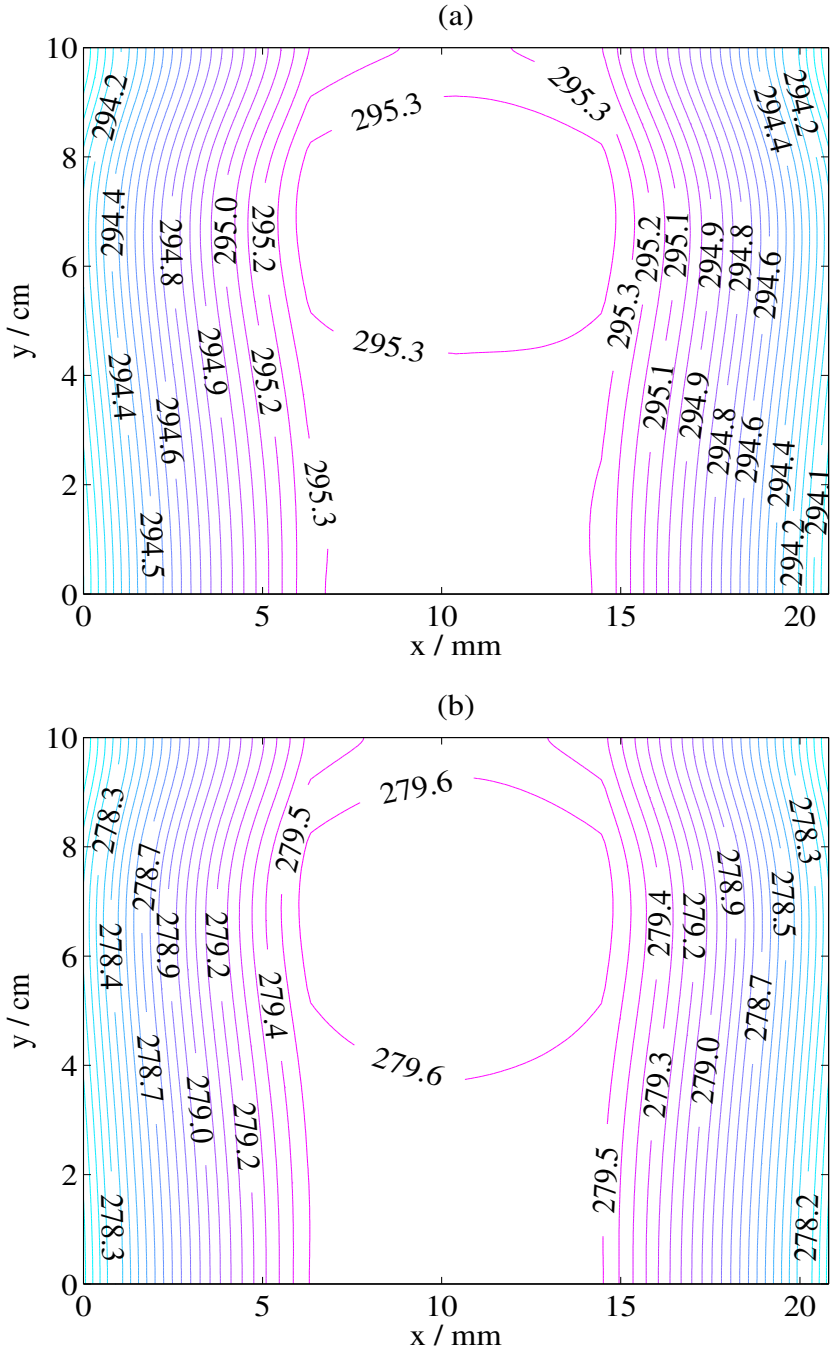

Figure 21: The distribution of temperature in the entire cell towards the end of discharge, $t = 49.17$ min, for the two cases (a) $Nu = 10$ (free convection) and (b) $Nu = 50$ (foced convection) in Figure 19. The various regions are as follows: current collector ($0 \leq x < 6.3$), negative electrode ($6.3 \leq x < 10.3$), membrane ($10.3 \leq x < 10.5$), positive electrode ($10.5 \leq x < 14.5$) and current collector ($14.5 \leq x \leq 20.8$). In both cases the external temperature, along the surfaces $x = 0$ mm and $x = 20.8$ mm, is $T_a = 273$ K. The other parameter values are given in Appendix (A).

Chapter 5
Effects of Hydrogen Evolution on the Battery Performance

5 Modelling Hydrogen Evolution

In this chapter, the incorporation of temperature (equation (91)) to the model developed in chapter three was ignored and the effects of bubble formation in the negative electrode on the battery behaviour are discussed below. The simulation results are presented and comparisons to the experimental data are made. The effects of varying the vanadium concentrations, the mean linear flow rate of the electrolyte, the applied current and the bubble diameter are discussed in detail.

All calculations were performed to an equivalent state of charge SOC, estimated from the residual V(III) concentration (equation (115)).

Experimental data are compared to simulation results at two different vanadium concentrations and mean linear flow velocities. For each case, the SOC value at the end of the charging period was estimated from simulation to be 0.794 based on the experimental charge time for $c_3^0 = c_4^0 = 1080$ mol m^{-3} (in the base case simulation, the experimental charge time was used and the SOC, as defined above, was measured).

5.1 Validation and the Effects of Hydrogen Evolution

Figure 22 shows a comparison between the simulated and experimentally obtained cell voltage, E_{cell} curves during charge/discharge for two different concentrations, $c_3^0 = c_4^0 = 1080$ mol m^{-3} and $c_3^0 = c_4^0 = 1440$ mol m^{-3}, with an applied current $I_{\text{app}} = 10$ A, a mean linear flow rate $\omega = 1$ mL s^{-1} and a bubble diameter $d_g = 50$ μm in both cases. The other parameter values are given in Appendix (A). The model captures the trends extremely well.

The discrepancies between the experimental and simulation results were discussed in Section 3.9. Both sets of results show increased efficiencies for an increased

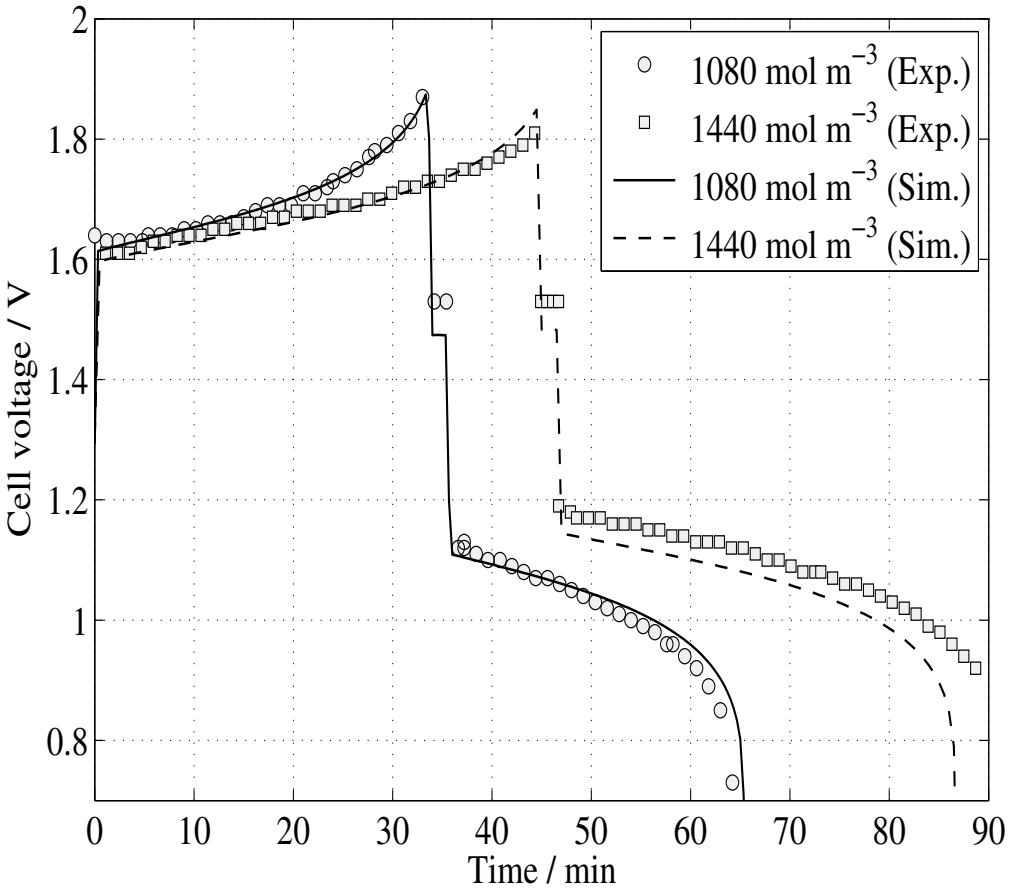

Figure 22: A comparison between simulated and experimentally obtained cell voltage, E_{cell} curves during charge/discharge for two different concentrations, $c_3^0 = c_4^0 = 1080$ mol m^{-3} and $c_3^0 = c_4^0 = 1440$ mol m^{-3}; $I_{\text{app}} = 10$ A, $\omega = 1$ mL s^{-1} and $d_g = 50$ μm in both cases. The other parameter values are given in Appendix (A). For both concentrations, SOC=0.794 at the end of charge: $t = 2017$ s for $c_3^0 = 1080$ mol m^{-3} and $t = 2687$ s for $c_3^0 = 1440$ mol m^{-3}.

concentration. At the lower concentration, $\xi_v = 59.7$ % and at the higher concentration, $\xi_v = 61.5$ %, while the coulombic efficiencies are 87.8 % and 90.1 % for the lower and higher concentrations, respectively. The latter two compare favourably with the experimental values of 85.1 % and 93.1 %, respectively.

Contour plots of the H_2 gas volume fraction, β_g at various times during charge and discharge for the case $c_3^0 = 1080$ mol m^{-3} are shown in Figures 23 and 24. In these plots, $x = 0$ mm corresponds to the current collector/negative electrode interface (x_1) in Figure 1 and $x = 4$ mm corresponds to the negative electrode/membrane interface (x_2). The inlet surface is represented by the line $y = 0$ and the outlet by $y = 10$ cm. During charge (Figures 23 (a) 1009 s and 23 (b) 2017 s), the volume fraction of H_2 increases as the height above the inlet surface increases along any vertical line. At the inlet, a zero volume fraction is maintained through the boundary condition, which represents inflow from a reservoir free of bubbles. It is worth noting that at the end of discharge (Figure 24 (b)), the H_2 has not entirely disappeared from the electrode, although the volume remaining is small.

In the x (horizontal) direction, the degree of variation in β_g is minimal, despite substantial variations in the H_2 volumetric current density, $2j_{H_2}$, as evidenced in Figures 25 and 26, which show the H_2 volumetric current density (in A cm^{-3}) and overpotential η_{H_2} (in mV), respectively in the negative electrode during charge for the case $c_3^0 = 1080$ mol m^{-3} (Figures 25 (a) and 26 (a), 1009 s and 25 (b) and 26 (b), 2017 s). Also evident from these plots is that the H_2 volumetric current density and the H_2 overpotential are closely linked, both sets of contours resembling a similar pattern during charge. Maxima in both are attained at the intersection between the outlet and the current collector, $y = 10$ cm, $x = 0$ mm, and the minima in both occur at the intersection between the membrane and the inlet, $y = 0$ cm and $x = 4$ mm. The H_2 current is controlled by the overpotential η_{H_2}, which is controlled primarily by the electronic potential, ϕ_s and the open-circuit potential, $E_{0,-}$.

The effect of H_2 evolution on the charge/discharge behaviour can be seen in Figure 27, which shows the charge/discharge curve for $c_3^0 = c_4^0 = 1080$ mol m^{-3} both with and without H_2 evolution included in the simulation (charge for 2017 s under 10

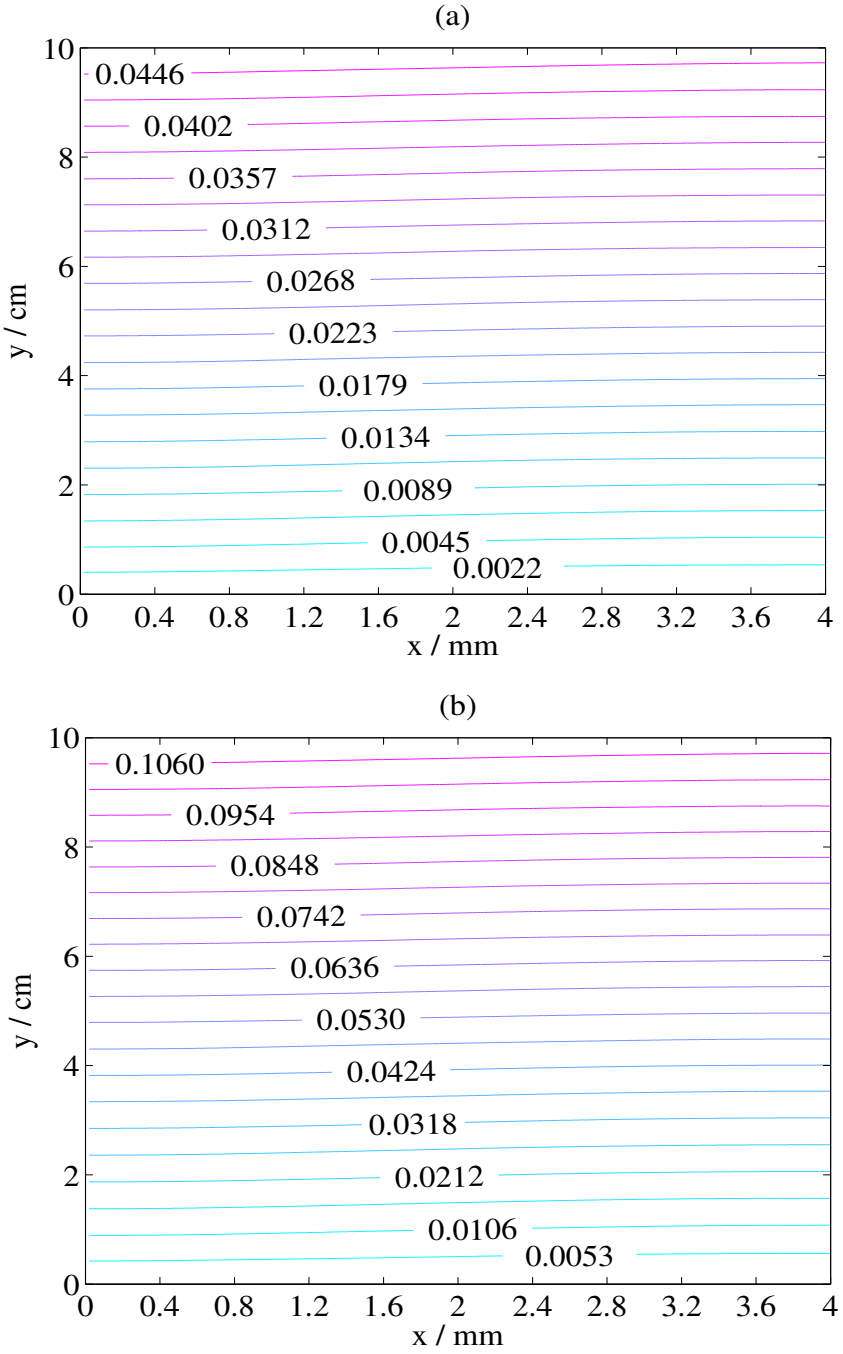

Figure 23: Contour plots of the H_2 gas volume fraction, β_g in the negative electrode during charge for the case $c_3^0 = 1080$ mol m^{-3} in Figure 22 at the times (a) $t = 1009$ s and (b) $t = 2017$ s. $x = 0$ mm corresponds to the current collector/electrode interface (x_1) in Figure 1 and $x = 4$ mm corresponds to the electrode/membrane interface (x_2) in Figure 1. The inlet surface is represented by the line $y = 0$ and the outlet by $y = 10$ cm. The other parameter values are given in Appendix (A).

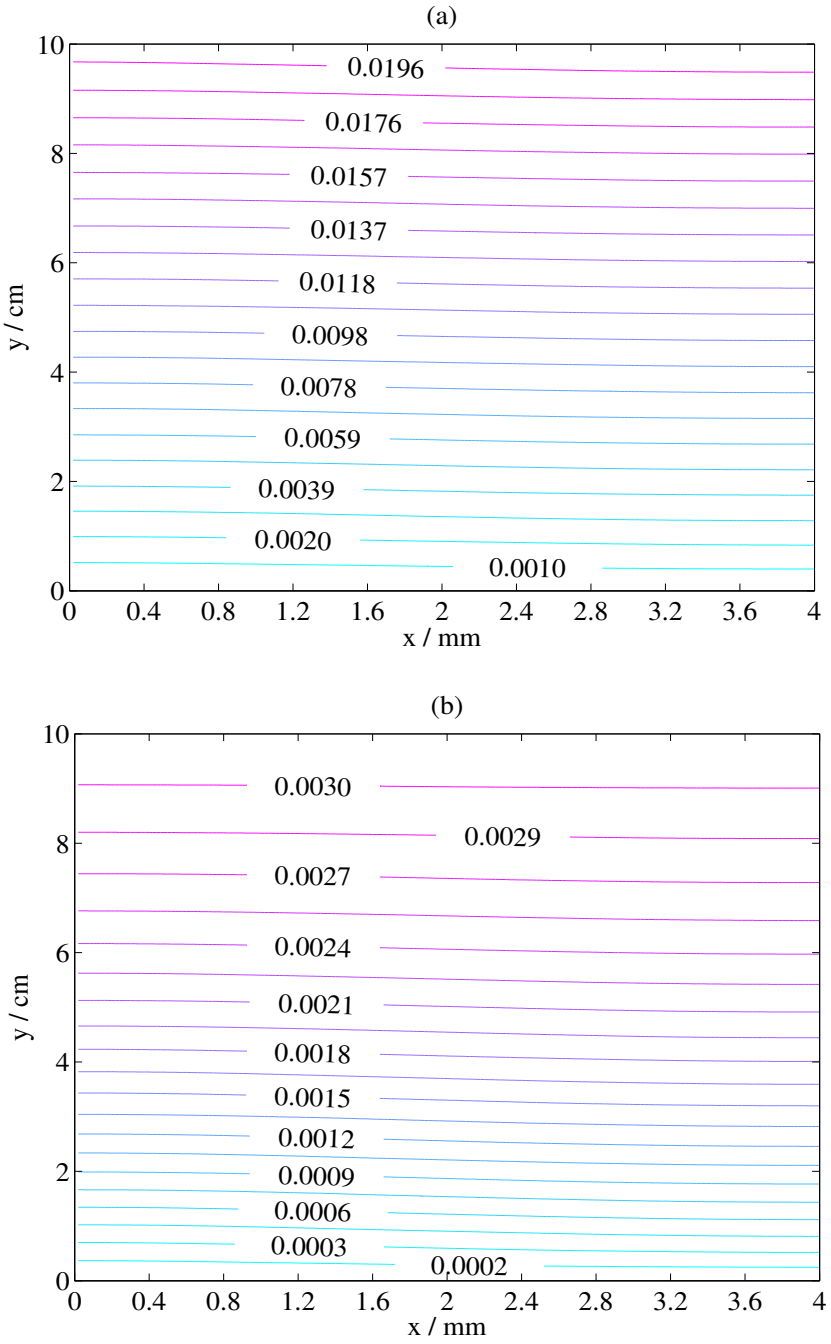

Figure 24: Contour plots of the H_2 gas volume fraction, β_g in the negative electrode during discharge for the case $c_3^0 = 1080$ mol m^{-3} in Figure 22 at the times (a) $t = 3000$ s and (b) $t = 3900$ s. $x = 0$ mm corresponds to the current collector/electrode interface and $x = 4$ mm corresponds to the electrode/membrane interface. The inlet surface is represented by the line $y = 0$ and the outlet by $y = 10$ cm. The other parameter values are given in Appendix (A).

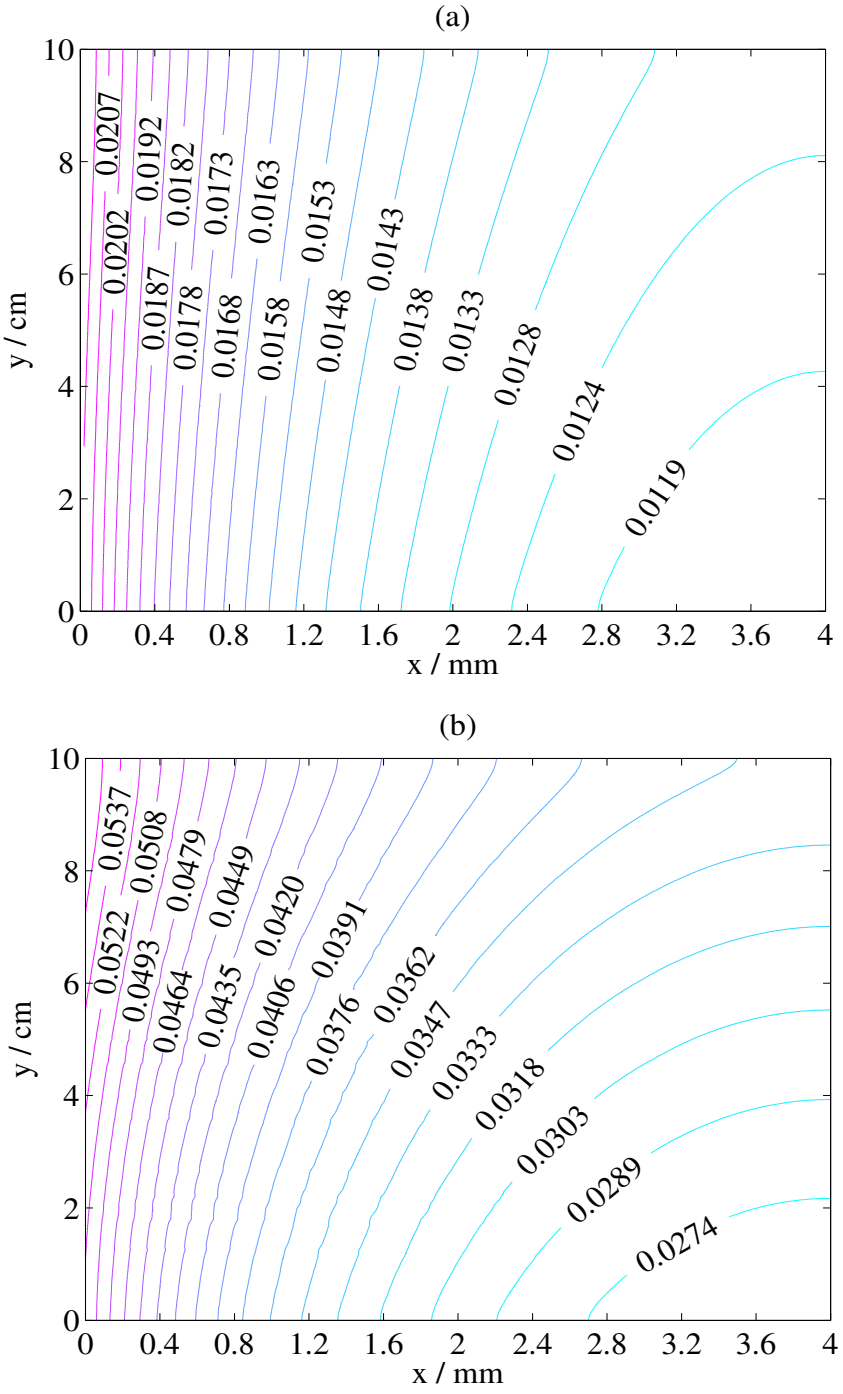

Figure 25: Plots of the volumetric current density associated with the H_2 evolution reaction, $2j_{H_2}$ (in A cm^{-3}) in the negative electrode during charge (see equation (87) at the times (a) $t = 1009$ s and (b) $t = 2017$ s. These Figures correspond to the case $c_3^0 = 1080$ mol m^{-3} in Figure 22. The other parameter values are given in Appendix (A).

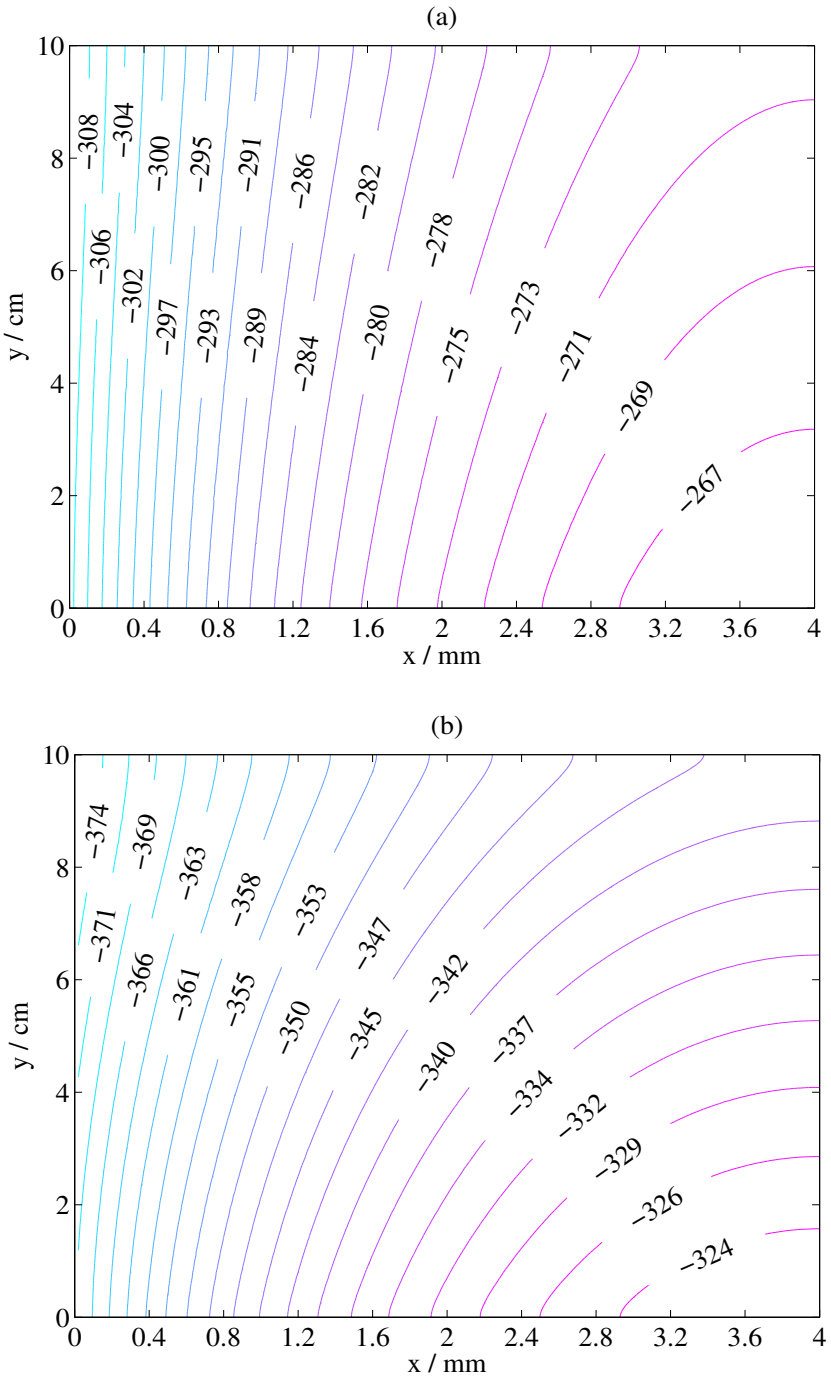

Figure 26: Plots of the overpotential associated with the H_2 evolution reaction, η_{H_2} (in mV) given by equation (88) in the negative electrode during charge at the times (a) $t = 1009$ s and (b) $t = 2017$ s. These Figures correspond to the case $c_3^0 = 1080$ mol m^{-3} in Figure 22. The other parameter values are given in Appendix (A).

A followed by 0 A for 120 s before discharge at 10 A). There are noticeable differences both in the cell voltage attained at the end of charge and in the times to discharge. For the calculations in Figure 27, the voltage efficiency is 59.7 % with evolution and 60 % without evolution. The difference between the coulombic efficiencies is more marked: 87.8 % with evolution and 99.7 % without evolution.

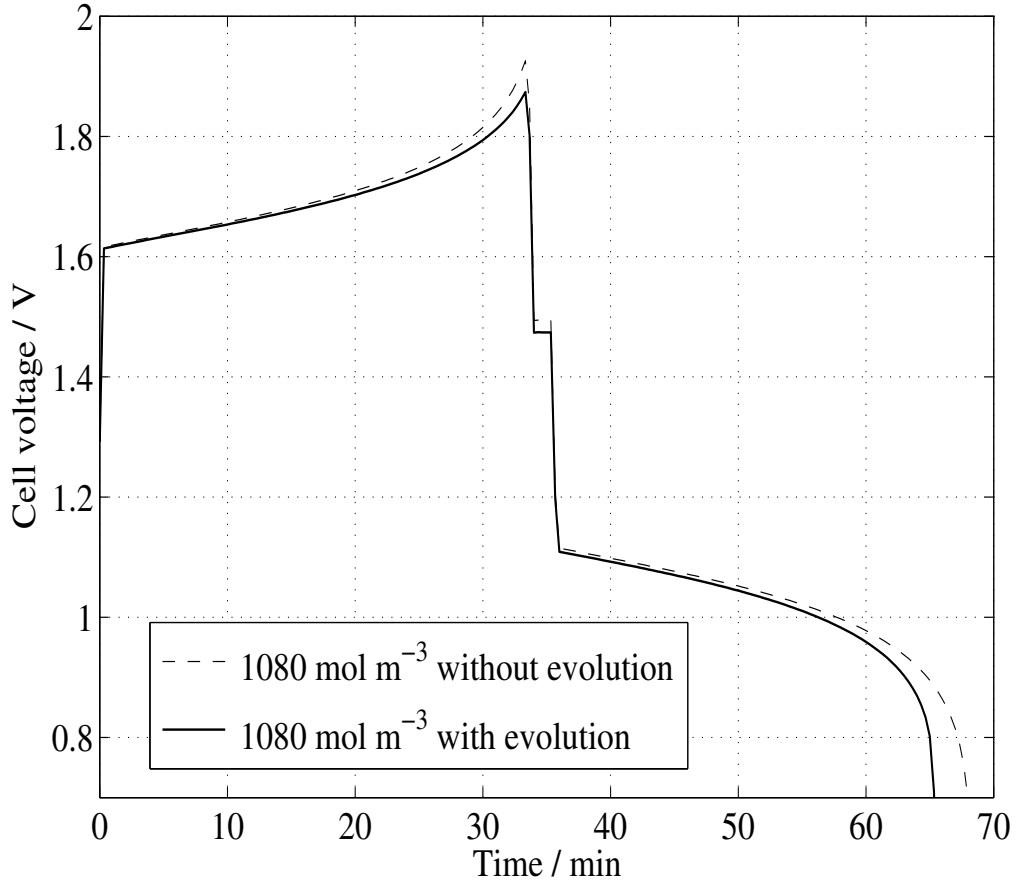

Figure 27: A comparison between simulated cell voltage, E_{cell} curves with and without H_2 evolution included; $c_3^0 = c_4^0 = 1080$ mol m^{-3}, $I_{\text{app}} = 10$ A, $\omega = 1$ mL s^{-1} and $d_g = 50$ μm in both cases. The other parameter values are given in Appendix (A). The charge time in both cases is 2017 s. With hydrogen evolution included, SOC=0.794 at the end of charge and without hydrogen evolution, SOC=0.854.

Figures 28 (a) and (b) show the total volumetric current density (in A cm^{-3}) at $t = 1900$ s, that is, (a) $j = j_- + 2j_{H_2}$ with H_2 evolution included, and (b) $j = j_-$ without H_2 evolution included (see equation (89) and the corresponding text). In

both cases, the maximum occurs at the intersection between the inlet and the current collector, $y = 0$ cm and $x = 0$ mm. With H_2 evolution included, the total volumetric current density is lowered. The evolution of the gas bubbles lowers j_- by a factor of β_g, which has a maximum of approximately 0.1 according to Figure 23 (b). This reduction is not balanced by the H_2 evolution volumetric current density, $2j_{H_2}$ in the vicinity of the current collector/electrode interface (Figure 25 (b) indicates that $2j_{H_2}$ is considerably smaller than j_-).

The corresponding profiles of the overpotential η_- are given in Figures 29 (a) and (b) (in mV). Markedly lower values are attained in the case with no H_2 evolution, consistent with the higher values of the total volumetric current density. The minimum overpotential value with H_2 evolution included occurs at $x = 0$ mm, $y = 0$ cm, whereas the minimum value without H_2 evolution included yields a minimum at around $x = 0$ mm, $y = 8$ cm. Up to a time of $t \approx 1500$ s, the minimum is attained at $x = 0$ mm, $y = 0$ cm, as in the case with H_2 evolution.

Beyond this time, mass transport effects become significant and the open-circuit potential, $E_{0,-}$, which decreases along a vertical line approaching the outlet, decreases more rapidly with time in a region close to the inlet. Simultaneously, the electronic potential, which decreases along any vertical line as the outlet is approached and along any horizontal line as the current collector is approached, also decreases. The net result is that the overpotential minimum is attained above the inlet surface along the current collector/electrode interface.

For the case without H_2 evolution included, the higher volumetric current density at a given time leads to a faster depletion of the V(III) reactant in the negative electrode, as seen in Figure 30, which shows the V(III) concentration profiles at $t = 1900$ s for the two cases (with and without H_2 evolution) in Figure 27. In turn, the overpotentials rise more rapidly to maintain the applied current in the mass-transport limited regime. At $t = 2017$ s, the concentration of V(II) is, therefore, higher in the case without evolution; with hydrogen evolution included, SOC=0.794 at the end of charge and without hydrogen evolution included, SOC=0.854 at the end of charge. This leads to a longer discharge time and, consequently, a higher coulombic

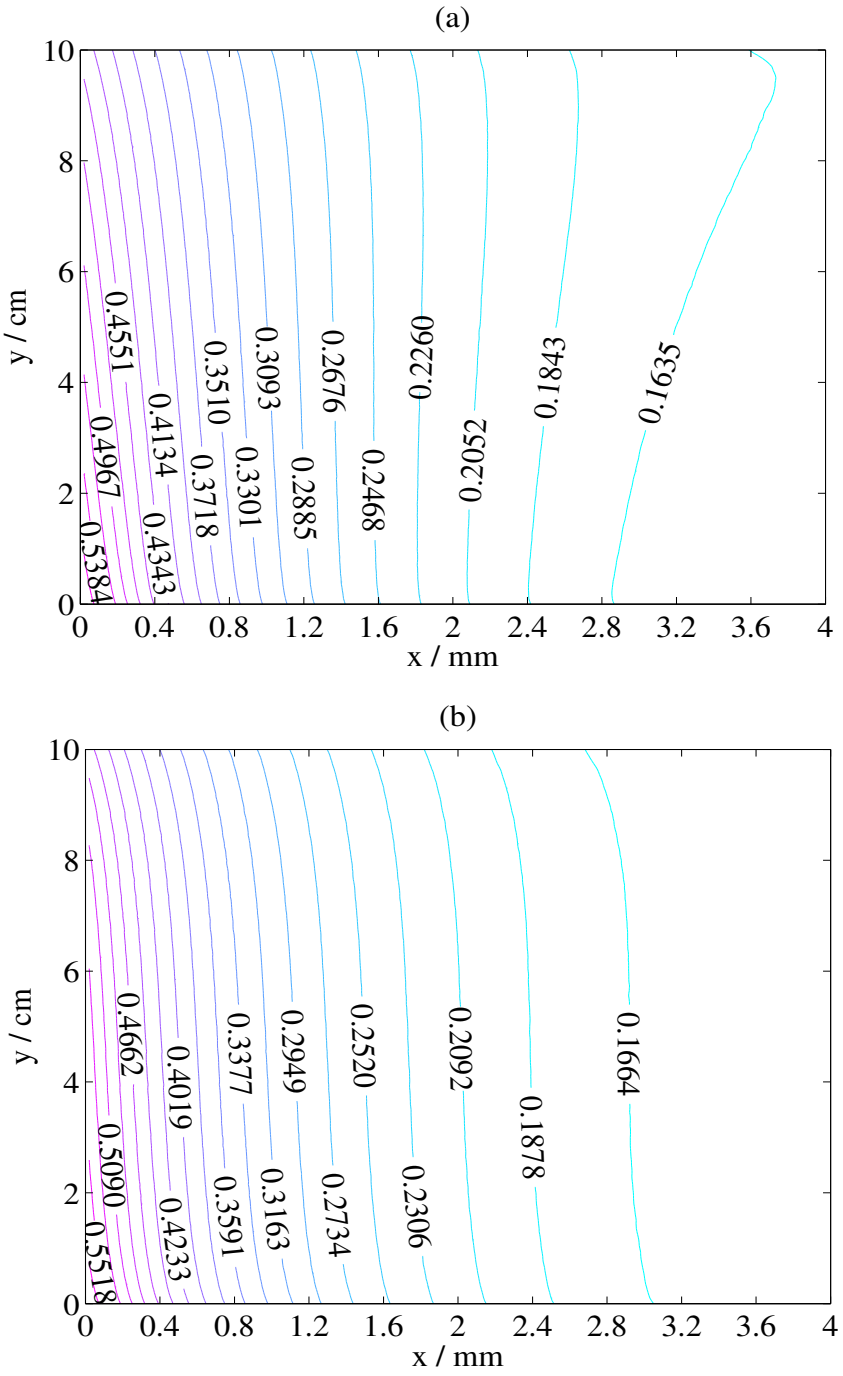

Figure 28: Contour plots of the total volumetric current density, j in A cm^{-3} (see equation (89)) in the negative electrode at $t = 1900$ s for $c_3^0 = 1080$ mol m^{-3}: (a) with hydrogen evolution included and (b) without hydrogen evolution. The V(III) concentration profiles at $t = 1900$ s are shown in Figure 30. The charge/discharge cycles corresponding to these plots are given in Figure 27. The other parameter values are given in Appendix (A).

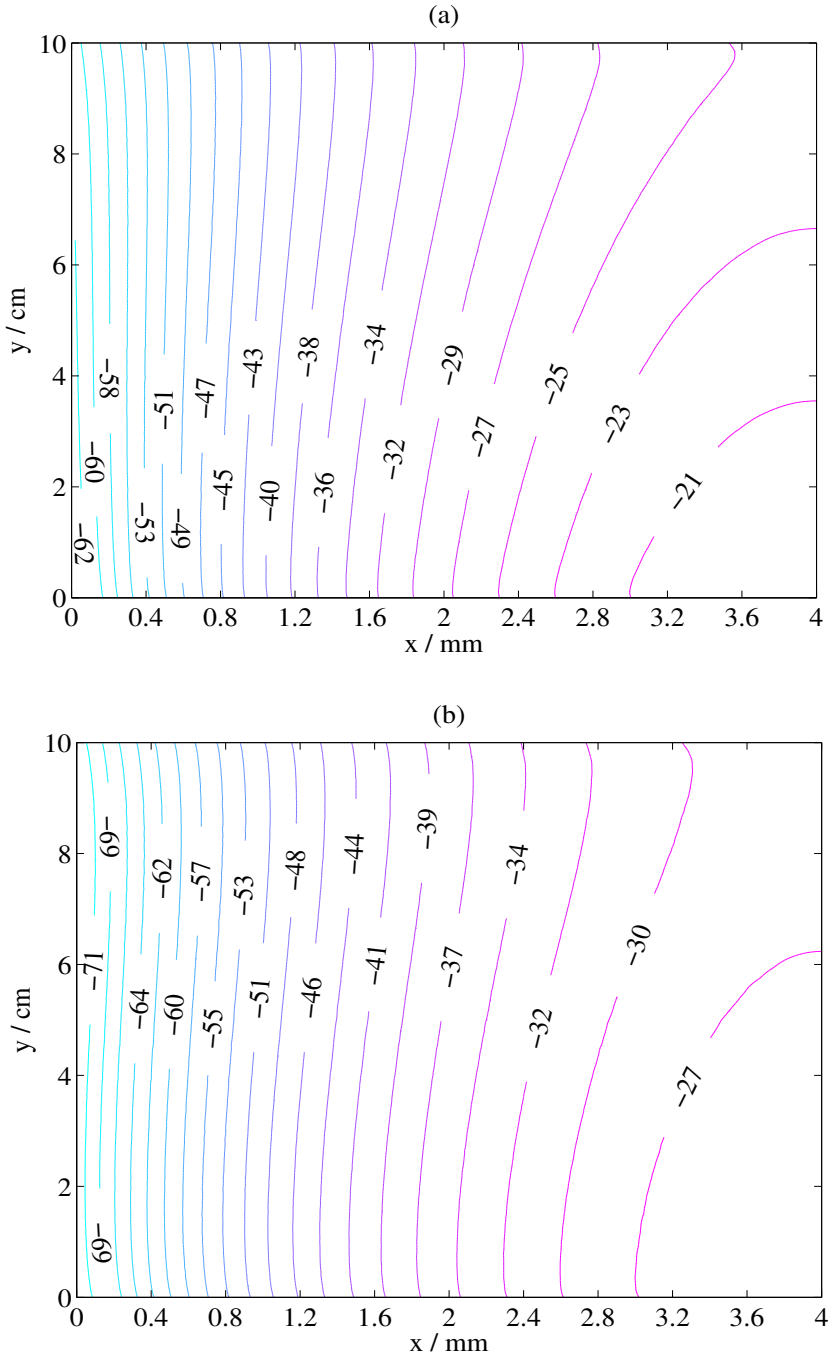

Figure 29: Contour plots of the overpotential, η_- in mV (see equation (88)) in the negative electrode at $t = 1900$ s for $c_3^0 = 1080$ mol m^{-3}: (a) with hydrogen evolution included and (b) without hydrogen evolution. The V(III) concentration profiles at $t = 1900$ s are shown in Figure 30. The charge/discharge cycles corresponding to these plots are given in Figure 27. The other parameter values are given in Appendix (A).

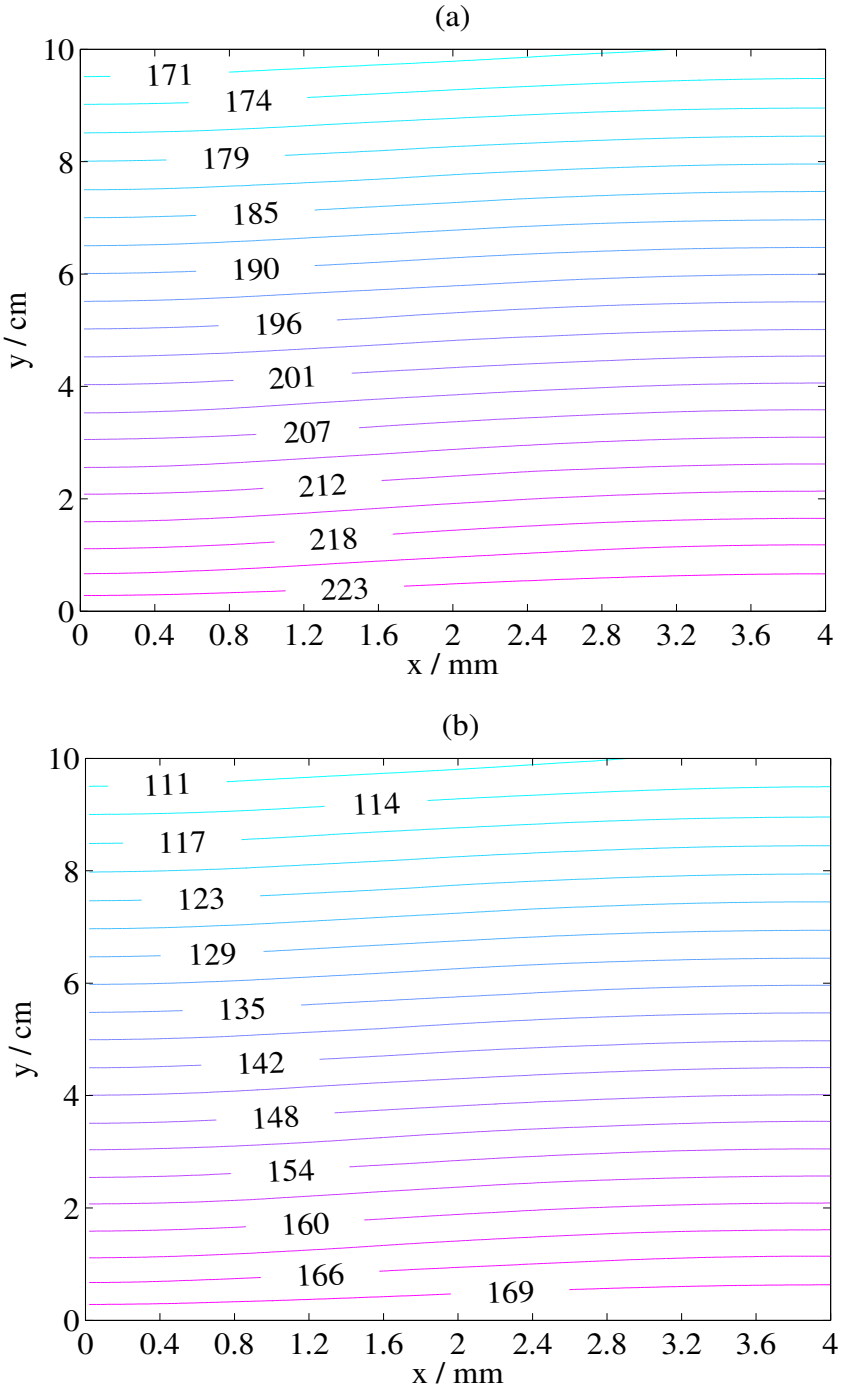

Figure 30: (a) The V(III) concentration (in mol m^{-3}) in the negative electrode at $t = 1900$ s with $c_3^0 = 1080$ mol m^{-3} and H_2 evolution included; (b) the equivalent plot without H_2 evolution. The corresponding potential and volumetric current density profiles are given in Figure 28 and the charge/discharge curves in Figure 27. The other parameter values are given in Appendix (A).

efficiency.

Figures 31 and 32 show the evolution of the vertical (y) component of the gas velocity, v_g (in mm s^{-1}) during the charge and discharge processes, respectively for the case $c_3^0 = c_4^0 = 1080$ mol m^{-3} in Figure 22. The gas velocity in the horizontal direction was three orders of magnitude slower as a result of the convection dominated flow of the electrolyte in the y direction. At the end of charge (Figure 31 (b)), the bubble velocity is approximately 17 % higher than the liquid velocity at the outlet, which is shown in Figure 33 (a); the gas bubbles are carried with the electrolyte vertically upwards and, moreover, are accelerated by a velocity, $\vec{u}_{\text{slip}}$, given in equation (61), by buoyancy forces acting in opposition to the viscous drag forces.

As with the gas volume fraction, the gas velocity increases along any vertical line from the inlet to the outlet. During charge, the maximum in the gas velocity is attained at the outlet/membrane interface, $y = 10$ cm, $x = 4$ mm, and during discharge it is attained at the outlet/current collector interface, $y = 10$ cm, $x = 0$ mm. During the charge phase, there is a decrease in the gas velocity along any horizontal line from the membrane to the current collector, as a result of the decrease in the liquid velocity in the same direction.

This can be seen from Figure 33, which shows the two contributions to the y component of the gas velocity, the y components of the liquid and slip velocities, at the end of charge (in mm s^{-1}). The y component of the liquid velocity, which has an initial/inlet value of 3.57 mm s^{-1}, varies by up to 5 % in the x direction, with lower values towards the current collector surface where the gas volume fraction is higher. During discharge, the liquid velocity (not shown) increases as the current collector is approached from the membrane surface along any horizontal line, which results in a increase in the gas velocity in the same direction (Figures 32 (a) and (b)).

The increased gas velocity in the vertically upward direction and the decreased liquid velocity in the horizontal direction as the current collector is approached are due to the increase in the gas volume fraction, which leads to an increased slip velocity, $\vec{u}_{\text{slip}}$ given by equation (61), with the pressure gradient given by equation (56). As the gas volume fraction, β_g increases, the Kozeny-Carman factor in the relative

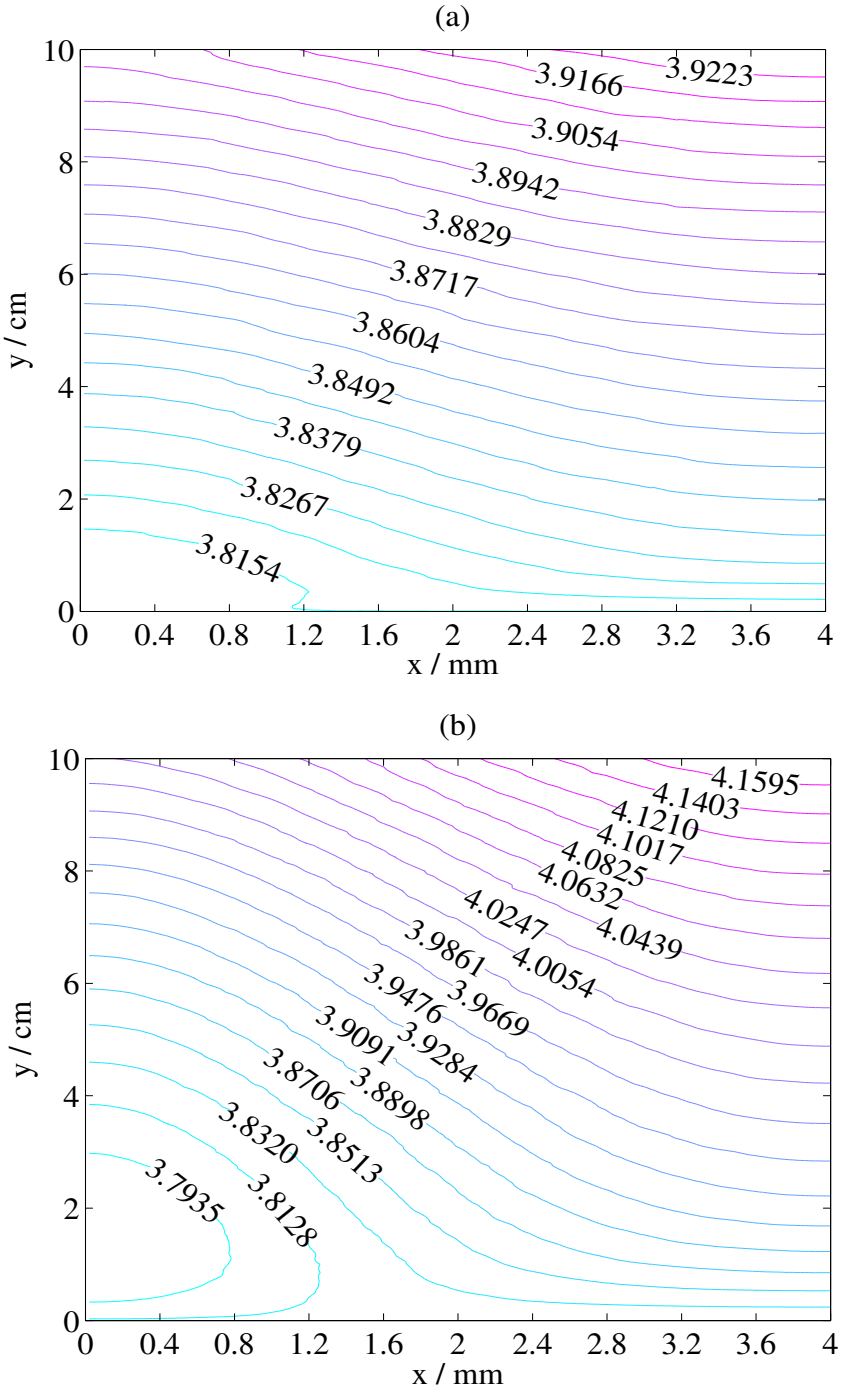

Figure 31: The vertical (y) component of the gas velocity, v_g in mm s^{-1} during the charge process for the case $c_3^0 = c_4^0 = 1080$ mol m^{-3} in Figure 22 at the times (a) $t = 1009$ s and (b) $t = 2017$ s. The other parameter values are given in Appendix (A).

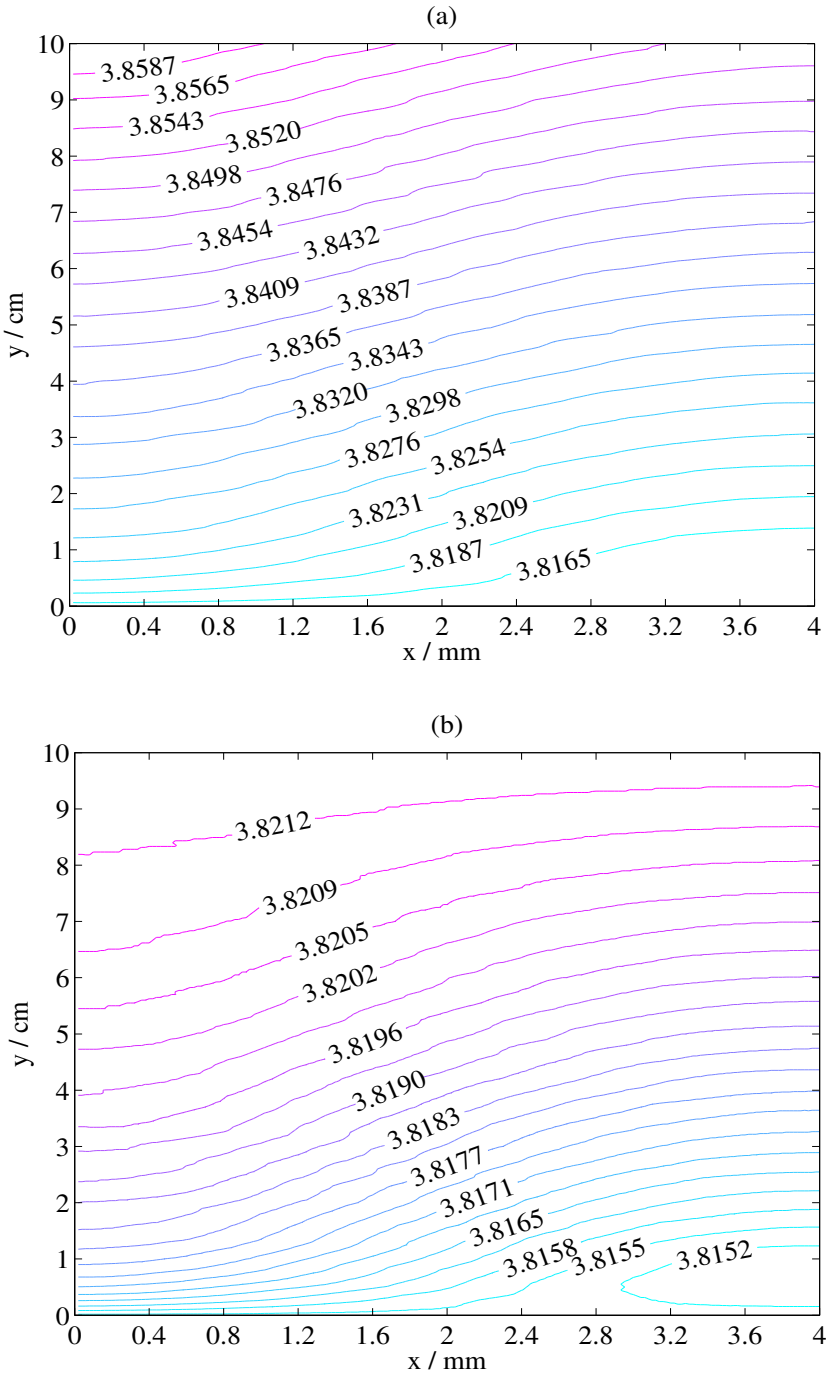

Figure 32: The vertical (y) component of the gas velocity, v_g in mm s^{-1} during the discharge process for the case $c_3^0 = c_4^0 = 1080$ mol m^{-3} in Figure 22 at the times (a) $t = 3000$ s and (b) $t = 3900$ s. The other parameter values are given in Appendix (A).

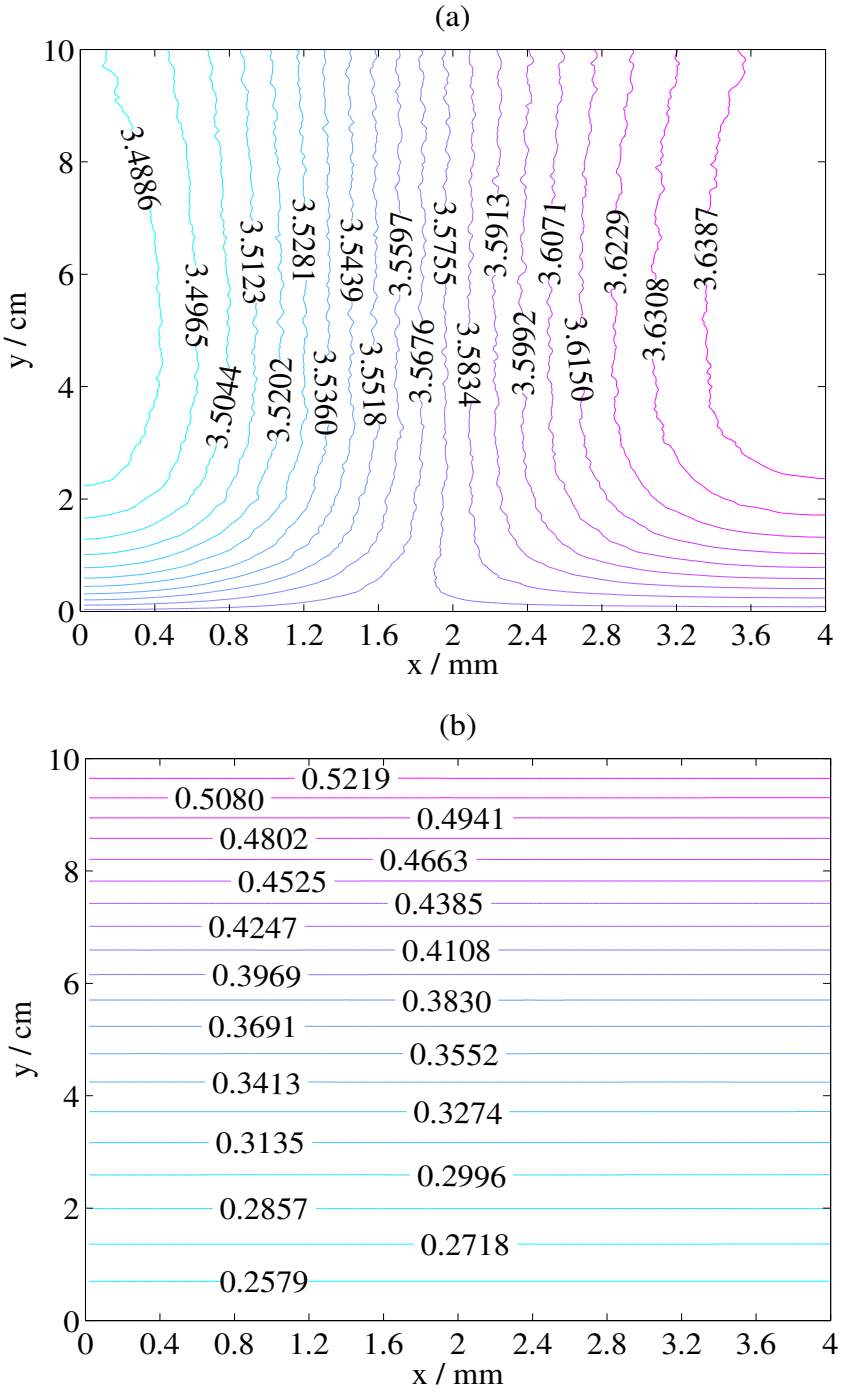

Figure 33: (a) The y components of the liquid velocity, u_l in mm s^{-1} and (b) the y component of the slip velocity, $\vec{v}_{\text{slip}}$ in mm s^{-1} at the end of charge ($t = 2017$ s) in the case $c_3^0 = c_4^0 = 1080$ mol m^{-3} in Figure 22. The other parameter values are given in Appendix (A).

permeability in equation (56) decreases, resulting in a lower liquid velocity, given by equation (53), and a higher value of ∇p; the reduced volume of liquid lowers the permeability and increases pressure gradients. To demonstrate this, consider the following one-dimensional boundary value problem:

$$\begin{aligned} -\frac{d}{dy}\left(\frac{d_f^2}{K\mu_l}\frac{\epsilon^3(1-\beta_g)^3}{(1-\epsilon(1-\beta_g))^2}\frac{dp}{dy}\right) &= 0; \qquad && 0 < y < h \\ -\frac{d_f^2}{K\mu_l}\frac{\epsilon^3(1-\beta_g)^3}{(1-\epsilon(1-\beta_g))^2}\frac{dp}{dy} &= v_{\text{in}}; && y = 0 \\ p &= p_{\text{out}}; && y = h \end{aligned} \tag{116}$$

with a constant value of β_g. Integrating the first of these equations and applying the boundary condition at $y = 0$, leads to an expression for dp/dy:

$$\frac{dp}{dy} = -v_{\text{in}}\frac{K\mu_l(1-\epsilon(1-\beta_g))^2}{d_f^2\epsilon^3(1-\beta_g)^3} \tag{117}$$

which increases as β_g increases. This analysis indicates that the slip velocity, which is directly proportional to ∇p, with a constant of proportionality $d_g^2/(18\mu_l)$, increases as β_g increases, *i.e.*, in the presence of a higher concentration of bubbles.

5.2 Mean Linear Flow Rate Effects

Figure 34 compares simulated and experimentally-obtained cell voltage E_{cell} curves during charge/discharge at the flow rates $\omega = 1$ mL s^{-1} (same as Figure 22) and $\omega = 3$ mL s^{-1}, with $c_3^0 = c_4^0 = 1080$ mol m^{-3}, an applied current $I_{\text{app}} = 10$ A and a bubble diameter $d_g = 50$ μm. The other parameter values are as in Appendix (A). The trend is well captured, particularly the increased coulombic efficiency as the flow rate is increased. The simulated values for the coulombic efficiency are 87.8 % and 91.7 % for $\omega = 1$ mL s^{-1} and $\omega = 3$ mL s^{-1}, respectively, while the experimental values are 85.1 % and 92.9 %, respectively. In agreement with the experimental curves, the cell

voltage at the higher flow rate is slightly lower during charge and the charge time (to the equivalent SOC) is slightly longer: 2028 s compared to 2017 s. During discharge, the cell voltage for $\omega = 3$ mL s^{-1} is slightly higher at any given time. The reason for this behaviour is the greater uniformity of the reactants for the higher flow rate (at the equivalent SOC), as discussed in detail elsewhere [37].

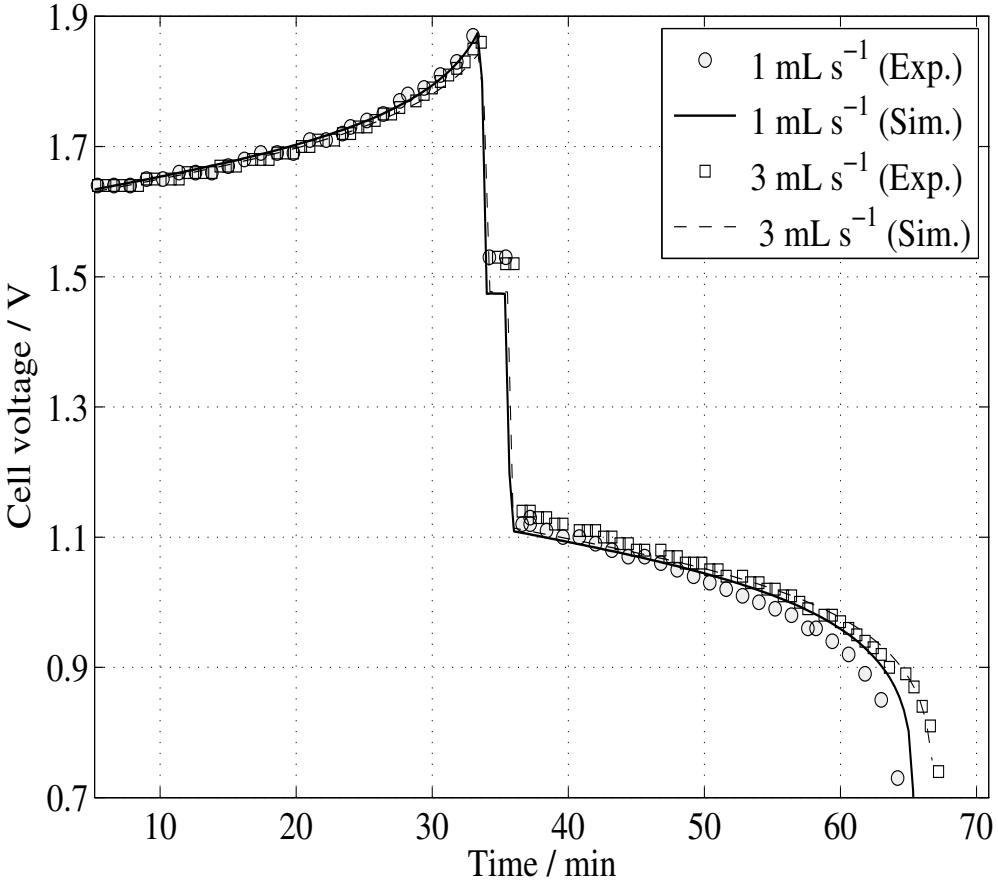

Figure 34: Simulated and experimentally obtained cell voltage, E_{cell} curves during charge/discharge at two flow rates, $\omega = 1$ mL s^{-1} and $\omega = 3$ mL s^{-1}; $c_3^0 = c_4^0 = 1080$ mol m^{-3}, $I_{\text{app}} = 10$ A and $d_g = 50$ μm in both cases. The other parameter values are given in Appendix (A). For both flow rates, SOC=0.794 at the end of charge: $t = 2017$ s for $\omega = 1$ mL s^{-1} and $t = 2028$ s for $\omega = 3$ mL s^{-1}.

Plots of the gas volume fraction, β_g and the y component of the gas velocity, v_g (in mm s^{-1}) at the end of charge, $t = 2028$ s, in the case with $\omega = 3$ mL s^{-1} are given in Figure 35. The maximum in the gas volume fraction, attained at $x = 4$ mm,

$y = 10$ cm, is a factor of approximately 3 lower than the maximum attained for $\omega = 1$ mL s^{-1} (Figure 23 (b)) at the equivalent SOC. The maximum in the y component of the gas velocity is approximately 10 % greater than the initial liquid velocity. At the lower flow rate, the equivalent difference is approximately 17 % (Figure 31 (b)). There appears to be a linear relationship between the gas volume fraction and the reciprocal of the flow rate. The lower gas volume fraction leads to a smaller departure of the gas velocity from the liquid velocity, *i.e.* a lower the slip velocity, as demonstrated in the analysis above.

Figure 36 shows the distribution of the volumetric H_2 evolution current density, $2j_{H_2}$ (in A cm^{-3}) and the overpotential, η_{H_2} (in mV) at the end of charge ($t = 2028$ s) in the case $\omega = 3$ mL s^{-1} in Figure 34. The higher flow rate leads to a more even distribution of reactant and, consequently, higher (smaller in magnitude) overpotential values. Thus, the H_2 evolution rate in the negative electrode is slightly lower than the equivalent rate in Figure 25 (b), which shows $2j_{H_2}$ for $\omega = 1$ mL s^{-1}. The overpotential values are slightly higher than the equivalent overpotential values in Figure 26 (b). The lower gas volume fraction at $\omega = 3$ mL s^{-1} is, however, due primarily to the increased rate at which the electrolyte is moved through the electrode; the flow is convection dominated in the y direction.

5.3 Applied Current Effects

Simulated cell voltage, E_{cell} curves during charge/discharge at two applied currents, $I_{\text{app}} = 10$ A (same as Figure 22) and $I_{\text{app}} = 15$ A, are shown in Figure 37. In these calculations, $c_3^0 = c_4^0 = 1080$ mol m^{-3}, $\omega = 1$ mL s^{-1} and $d_g = 50$ μm. The other parameter values are given in Appendix (A).

The charge times are chosen to give the same SOC at the end of the charging period: $t = 2017$ for $I_{\text{app}} = 10$ and $t = 1321$ s for $I_{\text{app}} = 15$. The efficiencies are lowered by the increased current. The voltage efficiency drops from $\xi_v = 59.7$ % to $\xi_v = 51.8$ %, while the coulombic efficiency experiences only a mild drop from $\xi_c = 87.8$ % to $\xi_c = 86.2$ %.

Figure 38 shows the distribution of the gas volume fraction, β_g and the y compo-

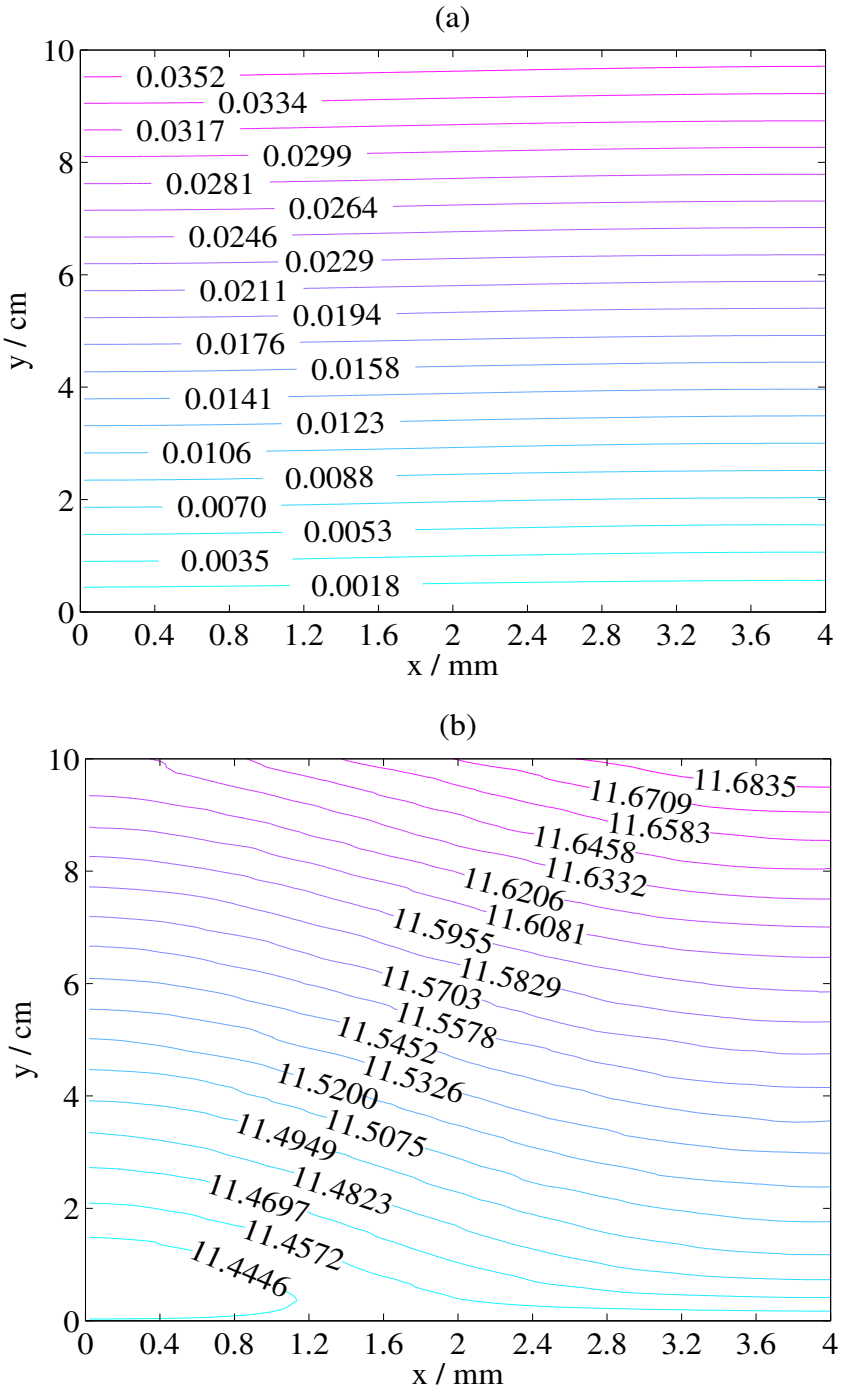

Figure 35: (a) Distribution of the gas volume fraction, β_g and (b) the y component of the gas velocity, v_g in mm s^{-1} at the end of charge ($t = 2028$ s) in the case $\omega = 3$ mL s^{-1} in Figure 34. The other parameter values are given in Appendix (A).

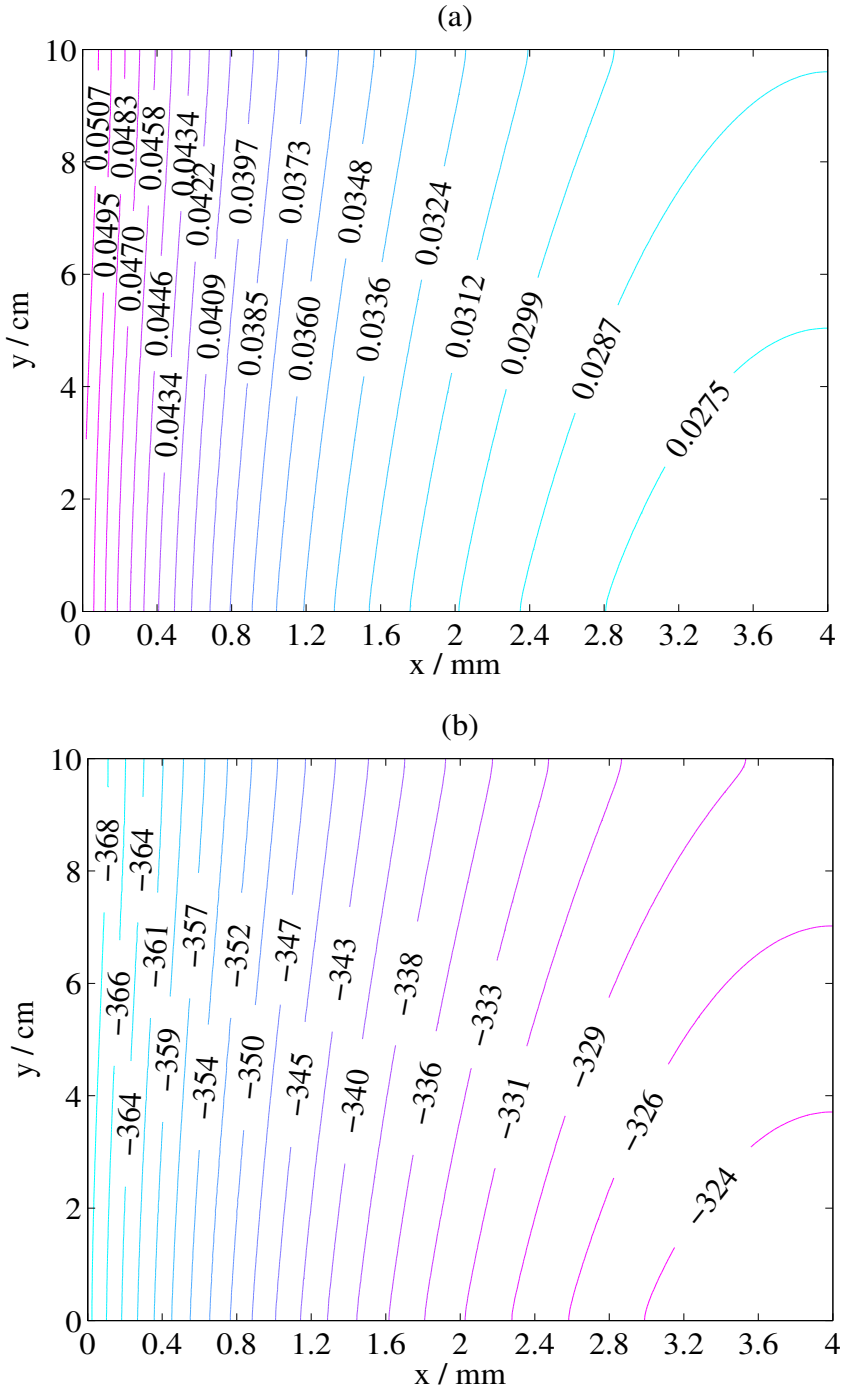

Figure 36: (a) Distribution of the volumetric H_2 evolution current density, $2j_{H_2}$ in A cm^{-3} and (b) the overpotential, η_{H_2} in mV at the end of charge ($t = 2028$ s) in the case $\omega = 3$ mL s^{-1} in Figure 34. The other parameter values are given in Appendix (A).

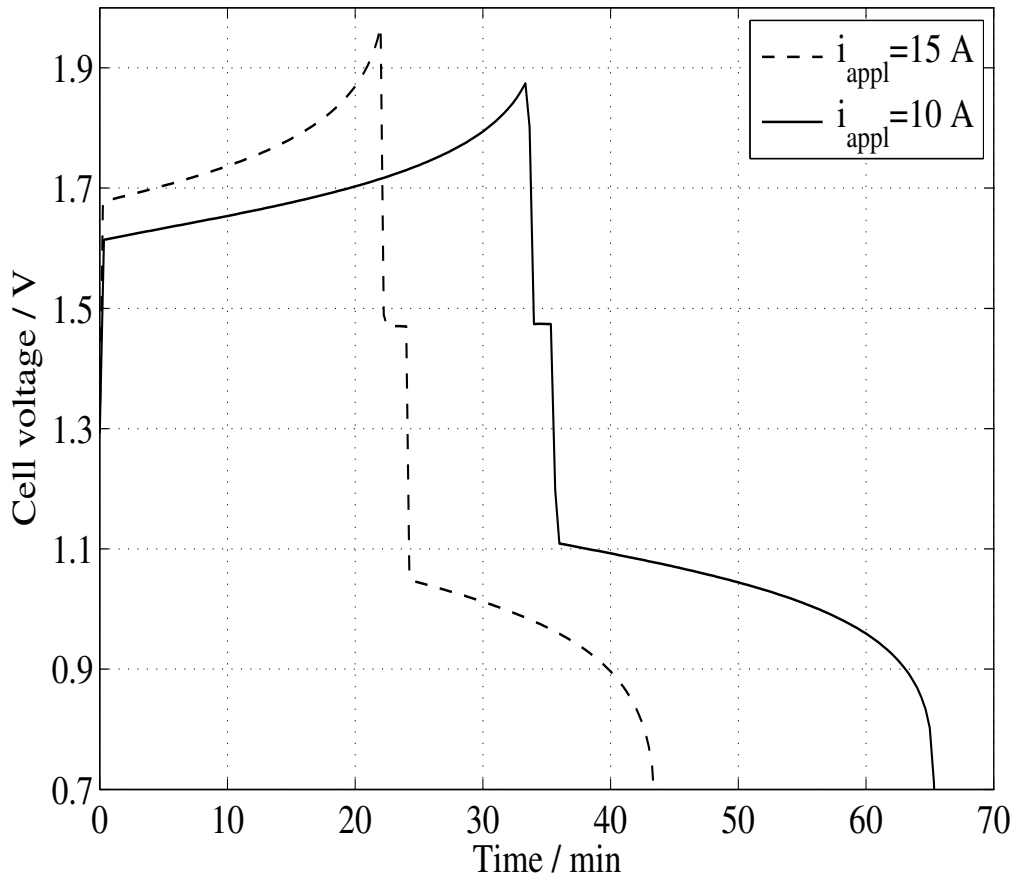

Figure 37: Simulated cell voltage, E_{cell} curves during charge/discharge for two different applied currents, $I_{\text{app}} = 10$ A and $I_{\text{app}} = 15$ A; $c_3^0 = c_4^0 = 1080$ mol m^{-3}, $\omega = 1$ mL s^{-1} and $d_g = 50$ μm in both cases. The other parameter values are given in Appendix (A). For both current densities, SOC=0.794 at the end of charge: $t = 2017$ s for $I_{\text{app}} = 10$ A and $t = 1321$ s for $I_{\text{app}} = 10$ A.

nent of the gas velocity, v_g (in mm s^{-1}) at the end of charge in the case with $I_{app} = 15$ A in Figure 37. These figures are to be compared with Figure 23 (b) and Figure 31 (b), respectively, for the case $I_{app} = 15$ A. The maximum in the gas volume fraction, attained at $y = 10$ cm, $x = 0$ mm, is approximately 27 % greater at the higher current density. The maximum in v_g is approximately 2 % higher, as a result of the increased volume fraction (see equations (116), (117) and the discussion above).

Figure 39 shows the corresponding profiles of the volumetric H_2 evolution current density, $2j_{H_2}$ and the overpotential, η_{H_2} at the end of charge, $t = 1321$ s, for $I_{app} = 15$ A. Comparisons with Figures 25 (b) and 26 (b), respectively, for $I_{app} = 10$ A, reveal that the volumetric current density is substantially higher and the overpotential is markedly lower, as a result of the increased applied current: the maximum in $2j_{H_2}$ is approximately 75 % greater and the minimum is approximately 17 % greater. The increased volume fraction of gas is, therefore, primarily a consequence of the faster rate of H_2 evolution. The modest increase in the gas velocity plays only a minor role in reducing the gas volume fraction, β_g.

5.4 Bubble Diameter Effects

The average (equivalent) diameter of the bubbles formed from gas evolution can range from 25 μm to 100 μm, depending on the operating conditions [122, 125, 126]. In a porous electrode, the diameter cannot exceed the largest pore diameter, typically in the range 100 μm to 800 μm for the porous carbon electrodes used in all-valadium RFB [161]; a value of 172 μm was used in this study [163]. In order to investigate the effects of the bubble diameter, simulations were performed using values of $d_g = 25$ μm and $d_g = 100$ μm, representing the two extremes of the reported values. In the simulations, the cell was charged at $I_{app} = 10$ A, with $c_3^0 = c_4^0 = 1080$ mol m^{-3} and $\omega = 1$ mL s^{-1}, to the equivalent state of charge for the corresponding calculation shown in Figure 22, where $d_g = 50$ μm.

Figures 40 and 41 show profiles of the gas volume fraction β_g and the y component of the gas velocity v_g (in mm s^{-1}), respectively at the end of charge. Figures 40 (a) and 41 (a) correspond to $d_g = 25$ μm and Figures 40 (b) and 41 (b) correspond

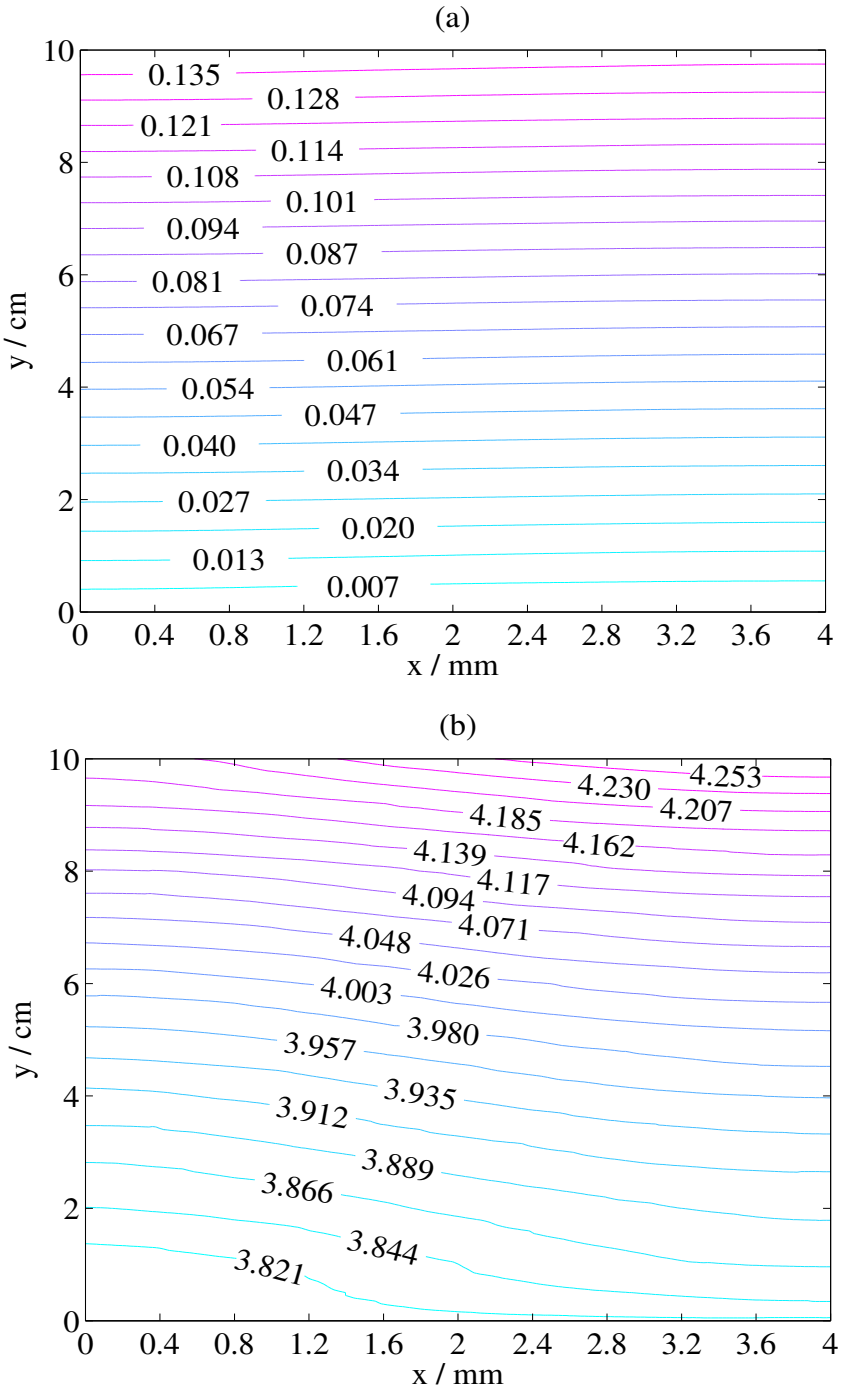

Figure 38: (a) Distribution of the gas volume fraction, β_g and (b) the y component of the gas velocity, v_g in mm s^{-1} at the end of charge ($t = 1321$ s) in the case $I_{\text{app}} = 15$ A in Figure 37. The other parameter values are given in Appendix (A).

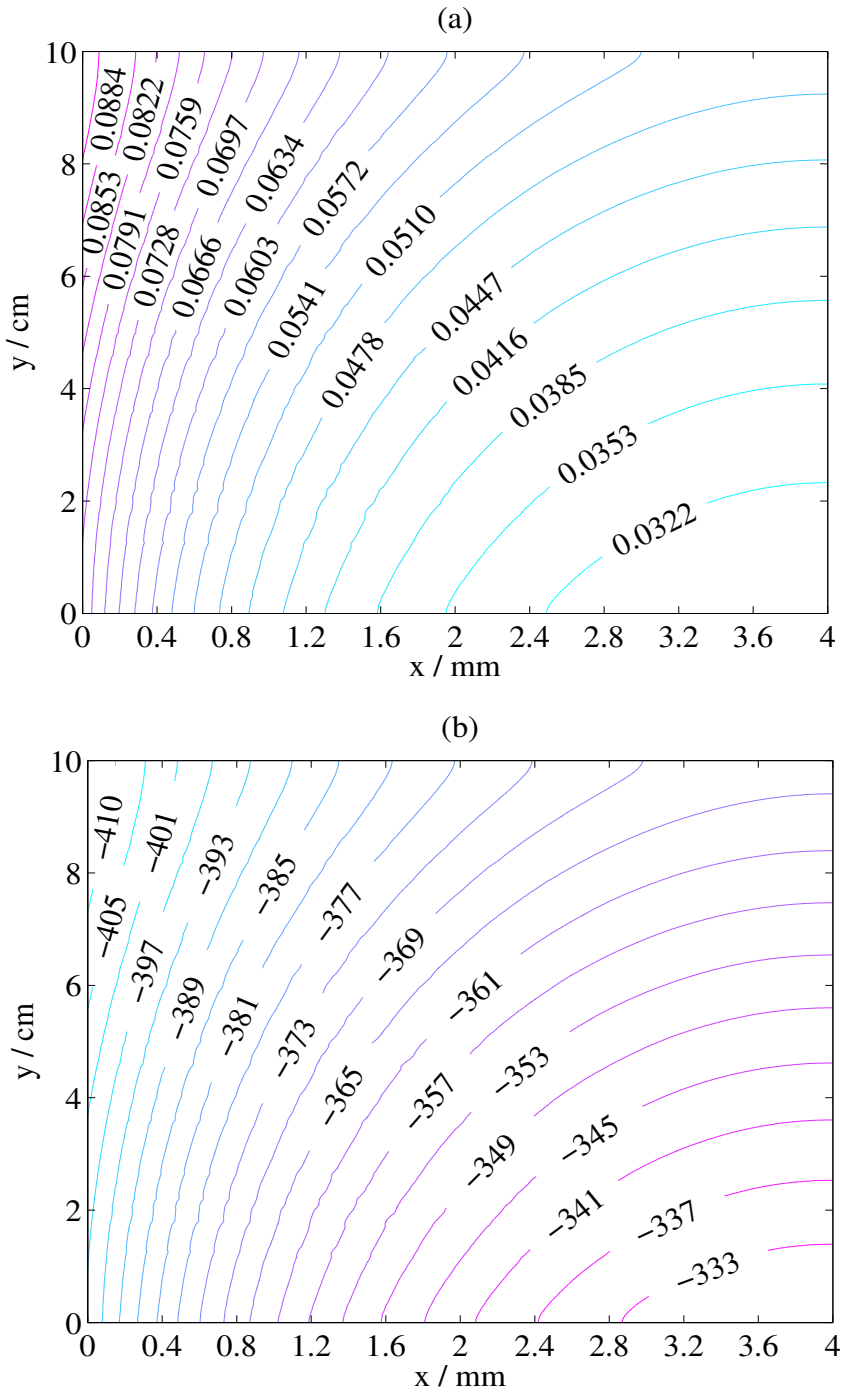

Figure 39: (a) Distribution of the volumetric H_2 evolution current density, $2j_{H_2}$ in A cm^{-3} and (b) the overpotential, η_{H_2} in mV at the end of charge ($t = 1321$ s) in the case $I_{app} = 15$ A in Figure 37. The other parameter values are given in Appendix (A).

to $d_g = 100$ μm. These figures are to be compared with Figure 23 (b) and Figure 31 (b), for the case $d_g = 50$ μm. The maximum in β_g, which is attained at $y = 10$ cm, $x = 0$ mm in all cases, decreases as the bubble diameter is increased; the value for $d_g = 25$ μm is approximately 47 % greater than the value for $d_g = 100$ μm. Likewise, there is a dramatic increase in the value of v_g, with the maximum value, at $y = 10$ cm, $x = 4$ mm, increasing by approximately 42 %.

Equation (61) indicates that the slip velocity increases with an increase in the bubble diameter, for a fixed pressure gradient, which leads to an increase in the gas velocity, given by equation (57). Physically, the drag is proportional to surface area of the bubble (or d_g^2) and buoyancy is proportional to the bubble volume (or d_g^3). Larger bubbles engender a higher slip velocity, leading to a higher gas velocity. The higher gas velocity removes the bubbles at a faster rate, thus lowering the gas volume fraction. This decrease in the gas volume fraction will tend to reduce the slip velocity but any such reduction is outweighed by the increase due to the bubble diameter effect.

5.5 Conclusions

Comparing the simulation results to those from a model that neglects H_2 evolution, it was demonstrated that the formation of H_2 reduces the efficiency of the battery. The main cause is partial consumption of the applied current in order to drive the H_2 reaction, reducing the current density associated with the redox reaction in the negative electrode.

The presence of the bubbles was found not to affect the electrolyte flow field significantly. This is likely to be a consequence of the relatively small volume fraction of gas and the large density difference between the two phases. The mean linear electrolyte flow rate appears, on the other hand, to strongly affect the volume of H_2 in the electrode during charge, by virtue of the rate of bubble removal through the outlet. For an increasing applied current density it was found that the gas volume fraction inside the electrode increases, at a given state of charge. The results suggest that a high flow rate could be used to minimise this increase in gas volume.

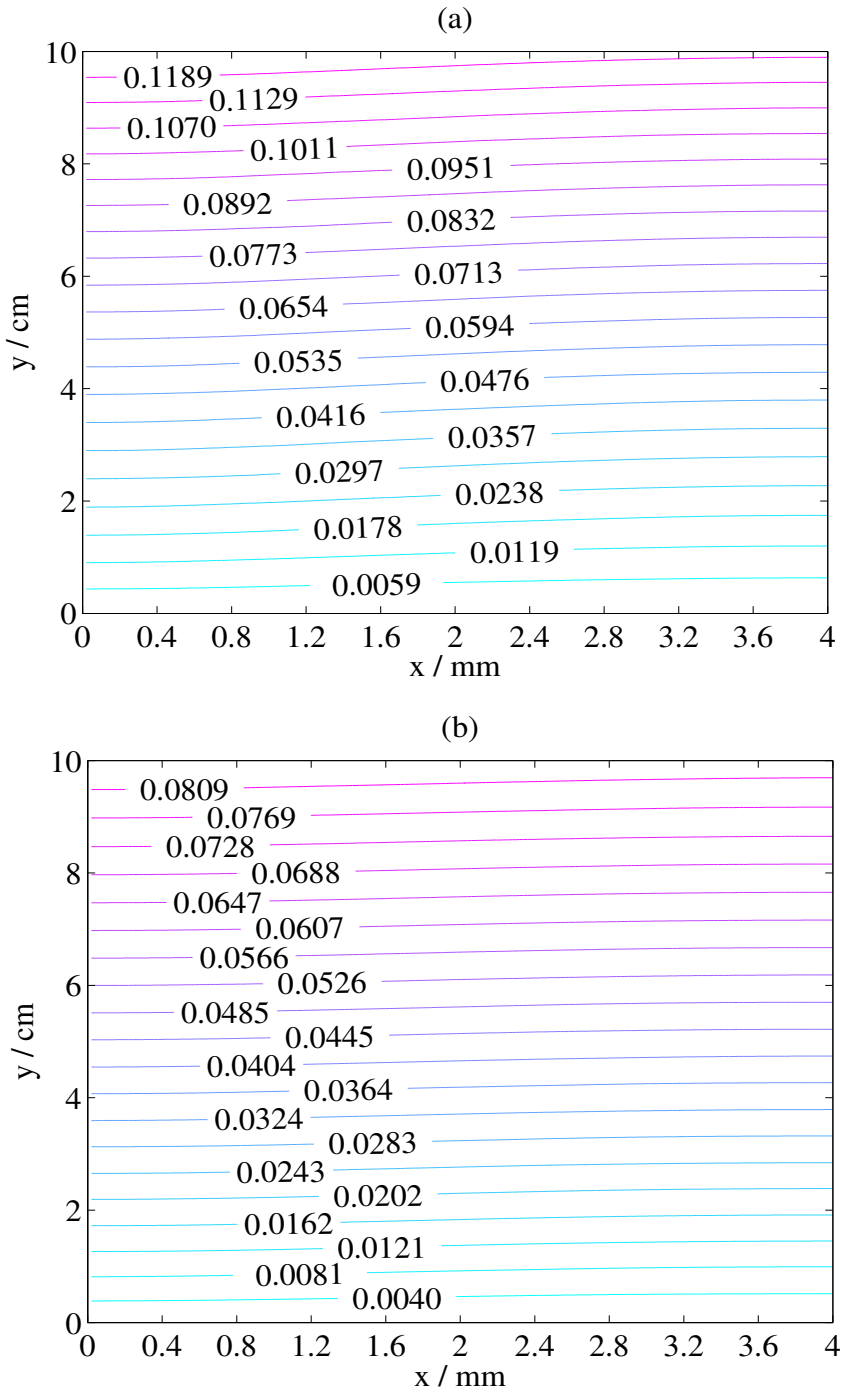

Figure 40: Profiles of the gas volume fraction, β_g at the end of charge for (a) a small bubble diameter, $d_g = 25$ μm and (b) a large bubble diameter, $d_g = 100$ μm; $I_{\text{app}} = 10$ A, $c_3^0 = c_4^0 = 1080$ mol m^{-3} and $\omega = 1$ mL s^{-1}. The other parameter values are given in Appendix (A).

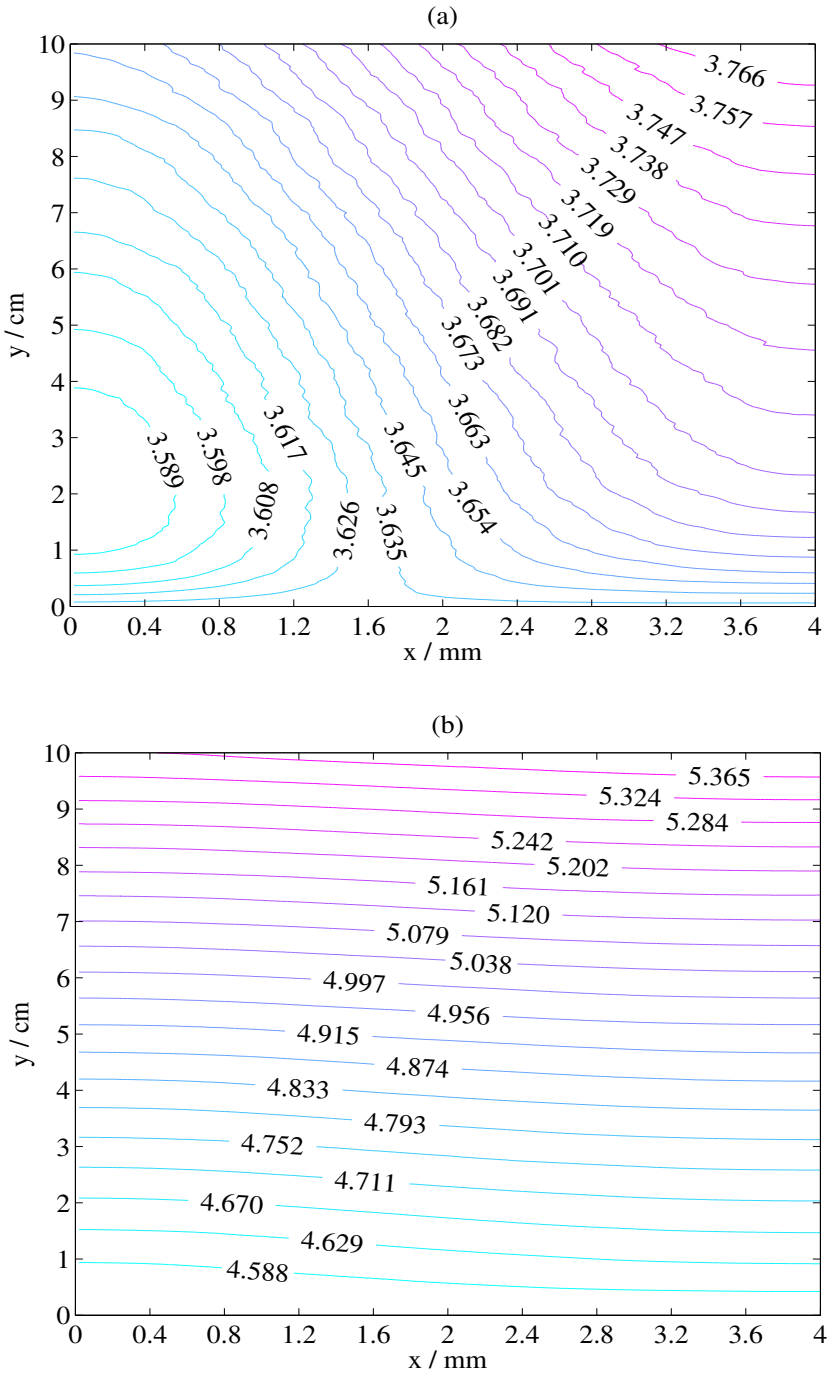

Figure 41: Profiles of the y component of the gas velocity, v_g in mm s^{-1} at the end of charge for (a) a small bubble diameter, $d_g = 25$ μm and (b) a large bubble diameter, $d_g = 100$ μm; $I_{\text{app}} = 10$ A, $c_3^0 = c_4^0 = 1080$ mol m^{-3} and $\omega = 1$ mL s^{-1}. The other parameter values are given in Appendix (A).

The equivalent diameter of the bubbles was shown to exert a strong influence on the gas volume fraction. As the bubble diameter is increased, the gas velocity is enhanced by increased buoyancy, leading to a reduction in the gas volume fraction in the negative electrode. The differences in the gas velocities and gas volume fractions between the smallest and largest reported values of the bubble diameter were found to be appreciable.

Chapter 6
Effects of Oxygen Evolution on the Battery Performance

6 Modelling Oxygen Evolution

In this chapter, the model developed in chapter three including the effects of temperature (equation (91)) and the bubble formation in the positive electrode (equation (62)) on the battery behaviour are discussed below. The effect of O_2 evolution on the efficiency of the battery and the influence of reactant concentration, temperature variations, electrolyte flow rate and bubble diameter are explored.

The state of charge in the calculations was estimated from the residual V(IV) concentration.

$$\mathrm{SOC} = 1 - \frac{c_{4,\mathrm{av}}}{c_4^0} \tag{118}$$

where the quantity $c_{4,\mathrm{av}}$ is the average V(IV) concentration in the positive half cell (including both the electrode and reservoir volumes). Experimental data are compared to simulation results at two different vanadium concentrations and mean linear flow velocities.

6.1 Validation and the Effects of Oxygen Evolution

Simulated and experimental cell voltage, E_{cell} curves for two concentrations, $c_3^0 = c_4^0 =$ 1080 mol m^{-3} and $c_3^0 = c_4^0 =$ 1440 mol m^{-3}, with an electrolyte flow rate of $\omega = 1$ mL s^{-1} and for two flow rates, $\omega = 1$ mL s^{-1} and $\omega = 3$ mL s^{-1}, with a concentration of $c_3^0 = c_4^0 =$ 1080 mol m^{-3} are shown in Figures 42 (a) and (b), respectively. The other parameter values are given in Appendix (A). The model captures the trends

well, both sets of results showing an increase in the cell voltage at the end of charge for the lower flow rate and concentration and an increase in the charge efficiency as the flow rate and concentration are increased as a result of greater spatial uniformity of the reactants at the equivalent SOC, as discussed in detail elsewhere [37].

As the concentration increases from $c_3^0 = c_4^0 = 1080$ mol m^{-3} to $c_3^0 = c_4^0 = 1440$ mol m^{-3}, the simulated charge efficiencies increase from 88.42 % to 91.2 % and the corresponding experimental efficiencies increase from 85.1 % to 93.1 %. Likewise, increasing the flow rate from $\omega = 1$ mL s^{-1} to $\omega = 3$ mL s^{-1}, increases the simulated and the experimental charge efficiencies to 91.8 % and 92.6 %, respectively. The charge time (to the equivalent SOC) for $\omega = 1$ mL s^{-1} was 33.67 min, while for $\omega = 3$ mL s^{-1} it was estimated to be 33.8 min and for $c_3^0 = c_4^0 = 1440$ mol m^{-3} to be 44.53 min. The latter two theoretical times were a good fit to the experimental times, in which the state of charge was measured by monitoring the open-circuit potential.

The effects of O_2 evolution on the charge/discharge behaviour are illustrated in Figure 43, which shows the cell voltage, E_{cell} curves for the base-case parameters both with and without O_2 evolution included in the model. The charge time is 33.67 min in each case, resulting in *different* SOC values at the end of charge for the two cases. The effects O_2 evolution are most strongly felt towards the end of charge, when the cell voltage in the case including O_2 evolution decreases relative to the case without O_2 evolution. During discharge, the presence of O_2 evolution reduces the time to discharge and, consequently, reduces the coulombic (charge) efficiency of the battery; the charge efficiency is 88 % with evolution and 99.7 % without evolution.

Figures 44 (a) and (b) show the distributions of the O_2 evolution current density, $j_{O_2} = 4\nabla \cdot \vec{j}_{O_2}$ (in mA m^{-2}) during charge, $t = 20$ min, and at the end of charge, $t = 33.67$ min. The left-hand side of the plots, $x = 5.8$ mm, corresponds to the membrane/positive electrode interface while the right-hand side, $x = 9.8$ mm corresponds to the positive electrode/current collector interface. The bottom line, $y = 0$ cm, corresponds to the inlet surface and the upper line, $y = 10$ cm, corresponds to the outlet. The maximum at both times occurs at the intersection between the outlet and the current collector ($x = 9.8$ mm, $y = 10$ cm) while the minimum occurs at the

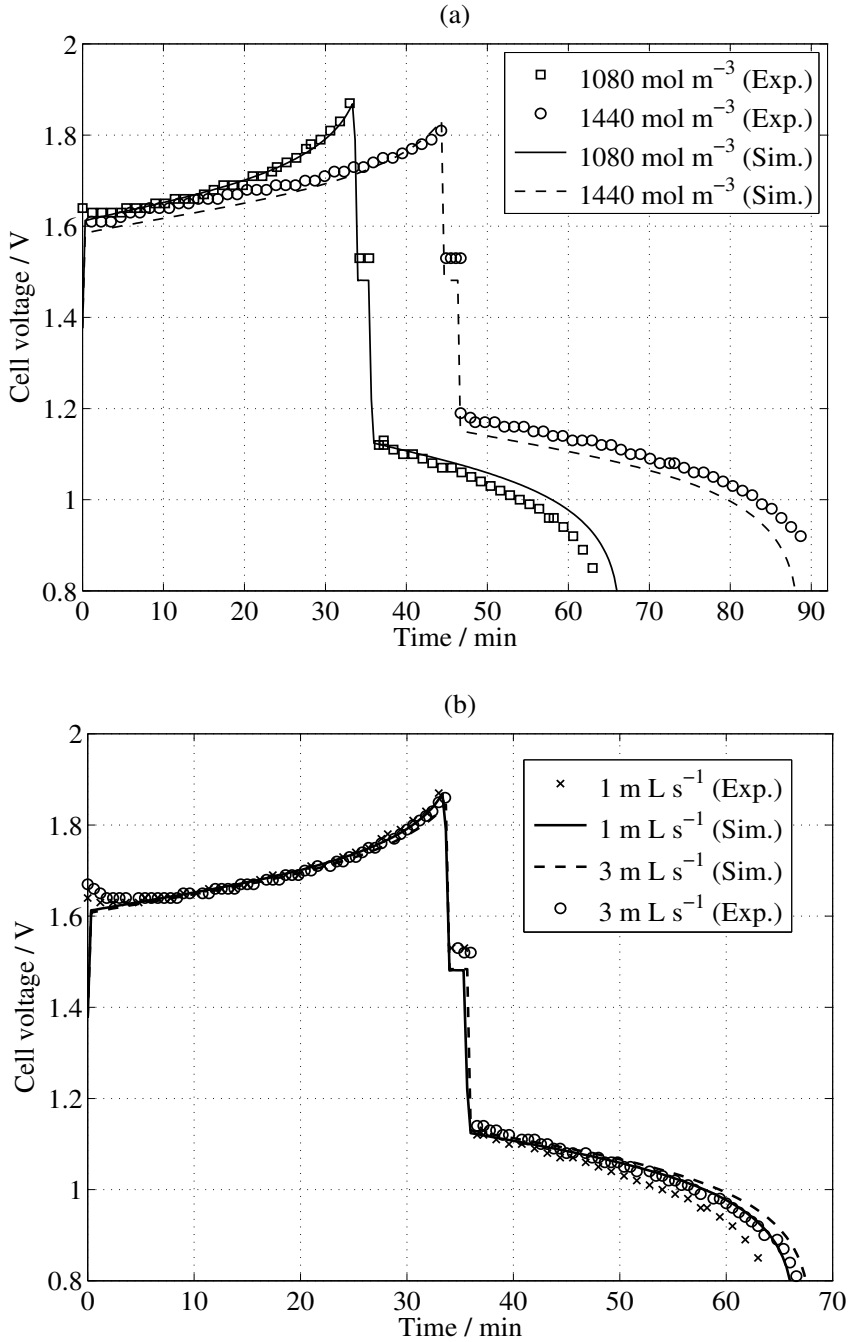

Figure 42: Simulated and experimentally obtained cell voltage, E_{cell} curves during charge/discharge at (a) two different concentrations of $c_3^0 = c_4^0 = 1080$ mol m^{-3} and $c_3^0 = c_4^0 = 1440$ mol m^{-3} at a flow rate of $\omega = 1$ mL s^{-1} and (b) two different flow rates of $\omega = 1$ mL s^{-1} and $\omega = 3$ mL s^{-1} at a concentration of $c_3^0 = c_4^0 = 1080$ mol m^{-3}. For all cases $I_{\text{app}} = 10$ A, $d_g = 50$ μm and $T_0 = 298$ K. The other parameter values are given in Appendix (A).

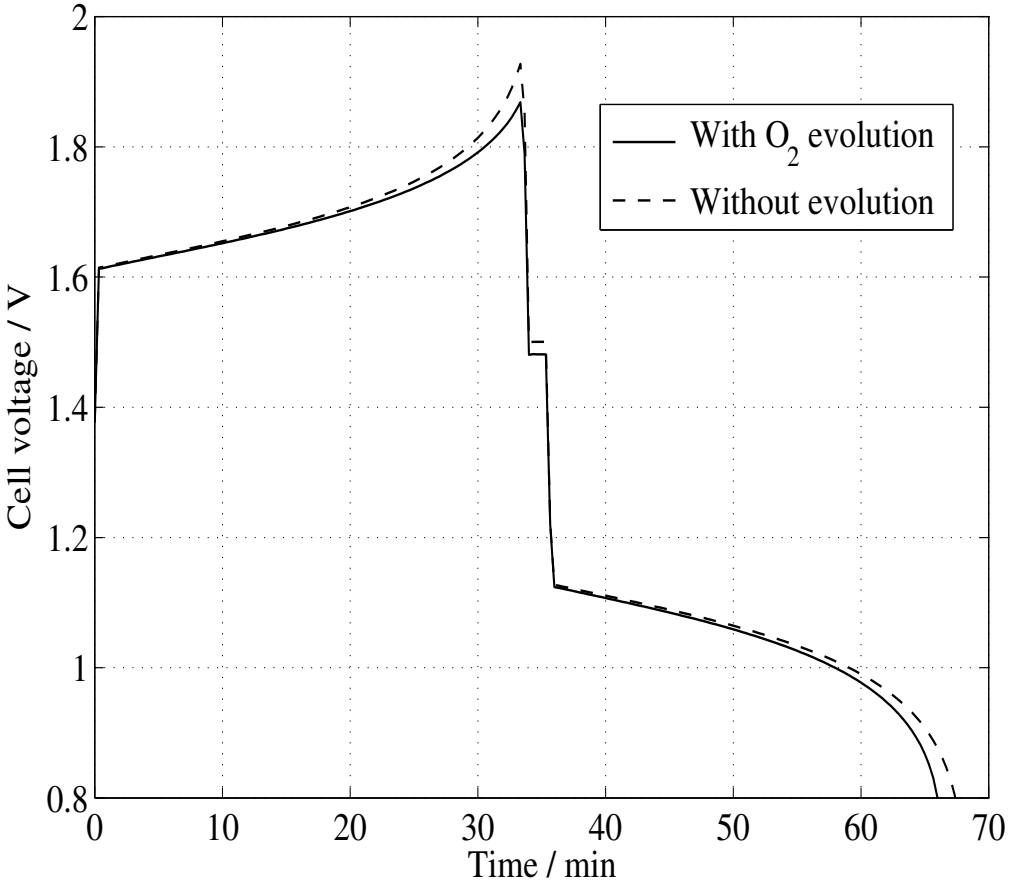

Figure 43: A comparison between simulated cell voltage, E_{cell} curves with and without O_2 evolution at $c_3^0 = c_4^0 = 1080$ mol m^{-3}, $I_{\text{app}} = 10$ A, $\omega = 1$ mL s^{-1}, $d_g = 50$ μm and $T_0 = 298$ K. The other parameter values are given in Appendix (A).

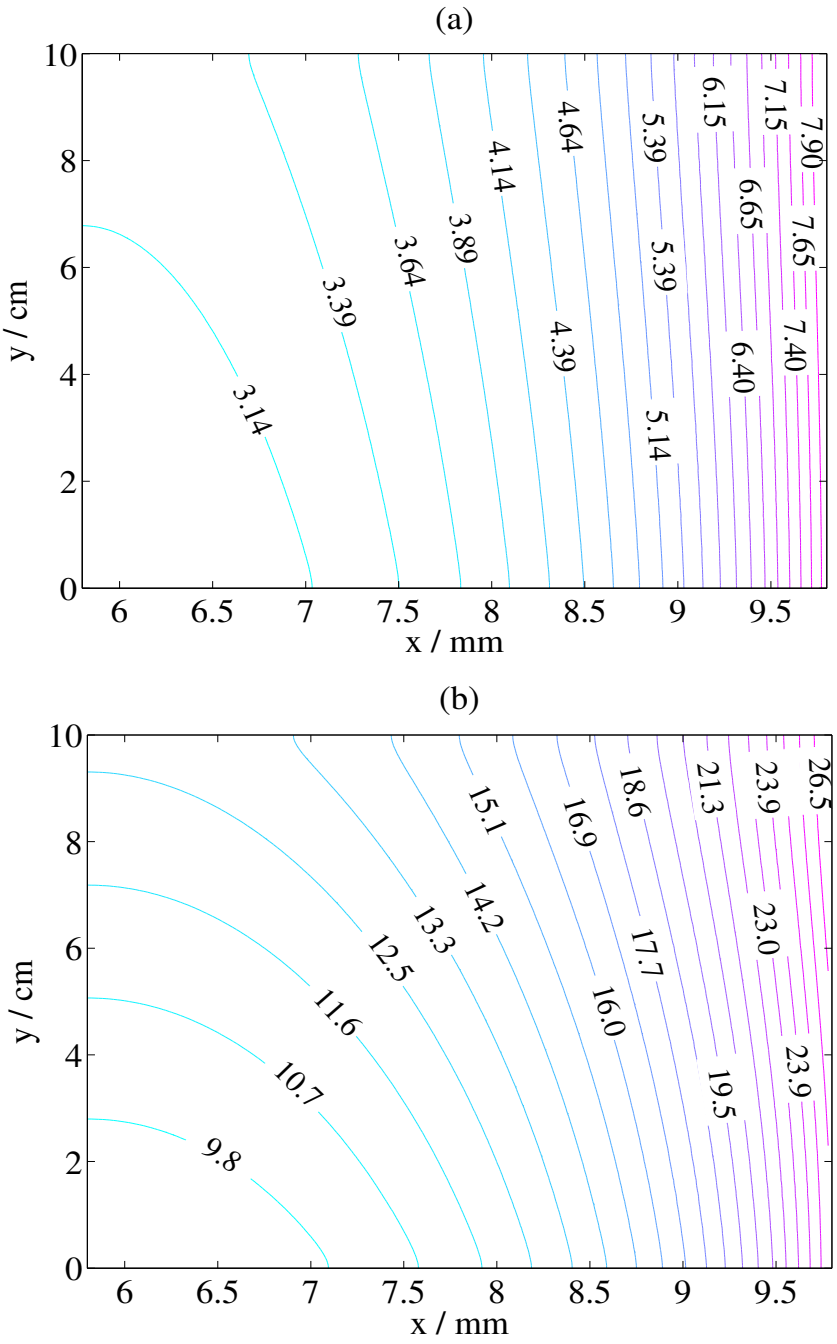

Figure 44: Plots of the O_2 evolution current density, j_{O_2} (in mA m^{-2}) in the positive electrode during charge at (a) $t = 20$ min and at (b) the end of charge, $t = 33.67$ min. In these simulations, $c_3^0 = c_4^0 = 1080$ mol m^{-3}, $I_{\text{app}} = 10$ A, $d_g = 50$ μm, $\omega = 1$ mL s^{-1} and $T_0 = 298$ K. The other parameter values are given in Appendix (A). The left hand side, $x = 5.8$ mm, corresponds to the membrane/electrode interface (x_3) in Figure 1 while the right hand side, $x = 9.8$ mm, corresponds to the electrode/current collector interface (x_4) in Figure 1.

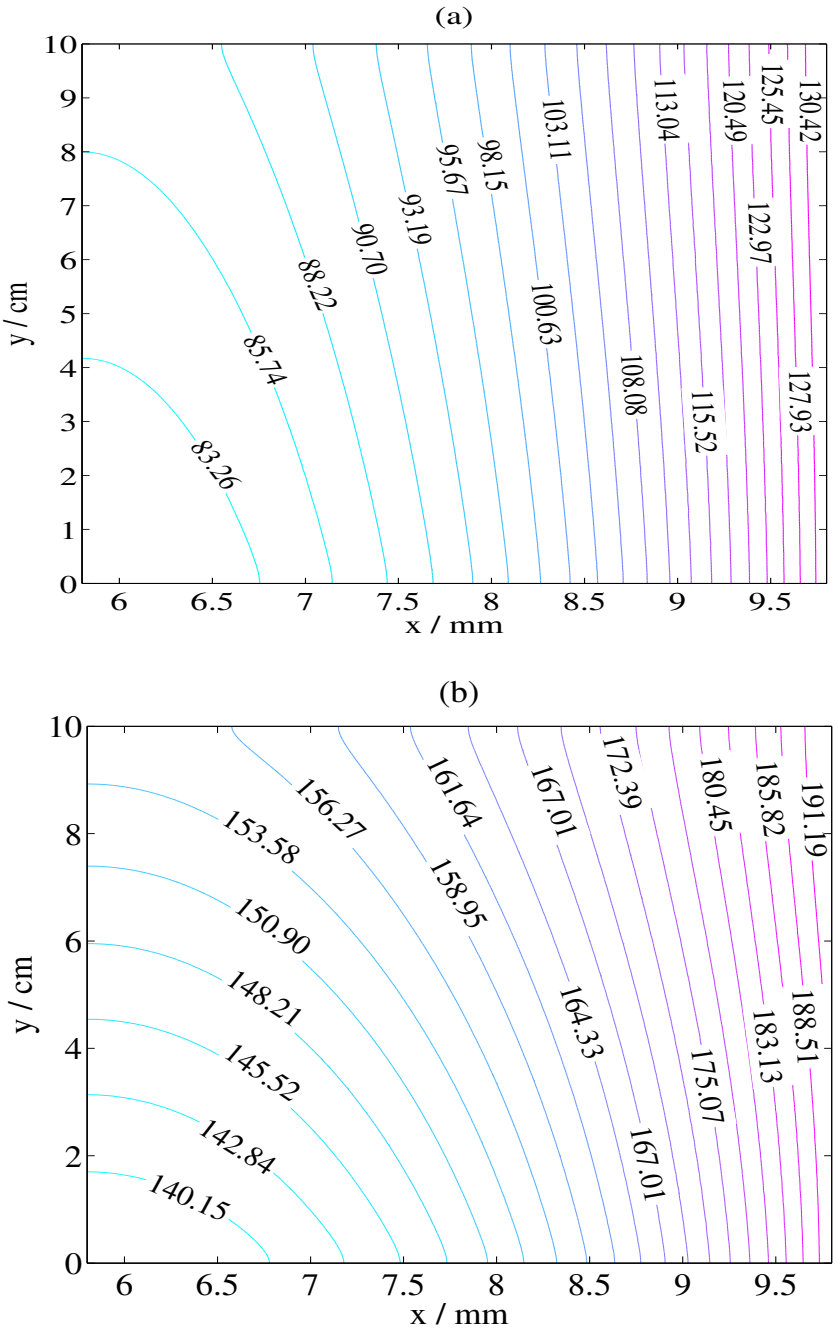

Figure 45: Plots of O_2 evolution overpotential, η_{O_2} (in mV) in the positive electrode during charge at (a) $t = 20$ min and at (b) the end of charge, $t = 33.67$ min. In these simulations, $c_3^0 = c_4^0 = 1080$ mol m^{-3}, $I_{\text{app}} = 10$ A, $d_g = 50$ μm, $\omega = 1$ mL s^{-1} and $T_0 = 298$ K. The other parameter values are given in Appendix (A). The left hand side, $x = 5.8$ mm, corresponds to the membrane/electrode interface while the right hand side, $x = 9.8$ mm, corresponds to the electrode/current collector interface.

intersection between the inlet and the membrane ($x = 5.8$ mm, $y = 0$ cm). The O_2 current density increases along any vertical line as the outlet is approached and along any horizontal line as the current collector approached.

The corresponding distributions of the O_2 evolution overpotential, η_{O_2} (in mV) are given in Figures 45 (a) and (b). There is a close link between the O_2 evolution current density, j_{O_2} and the O_2 evolution overpotential, η_{O_2}, their distributions resembling a similar pattern during charge. It appears that the O_2 evolution current density is controlled by the O_2 evolution overpotential, which is controlled primarily by the electronic potential, ϕ_s, and the open-circuit potential E_{0,O_2}.

Figures 46 (a) and (b) show the profiles of the redox reaction current density, $\nabla \cdot \vec{j} = j_1$ (in mA m^{-2}) with and without O_2 evolution, respectively, at the end of charge in the positive electrode ($t = 33.67$ min). In both cases, the maximum occurs at the intersection between the inlet and the current collector surface ($x = 9.8$ mm, $y = 0$ cm).

The maximum value of the total current density with evolution is approximately 20 % lower than its maximum value in the case without evolution. This is clearly due to the presence of the O_2 evolution reaction, which consumes a portion of the applied current and reduces the value of j_1 by a factor of β_g . The state of charge at $t = 33.67$ min is, therefore, higher in the case without O_2 evolution, leading to a longer time required to reach full discharge (consume the V(V) in the positive electrode and V(II) in the negative electrode). Consequently, the charge efficiency is higher. Figures 47 (a) and (b) show the V(V) concentration profiles at $t = 64.33$ min during discharge, with clearly higher concentrations in the case without O_2 evolution.

6.2 Influence of Electrolyte Flow Rate

Contour plots of the O_2 volume fraction, β_g in the positive electrode at the end of charge (to an equivalent SOC) for two different flow rates, $\omega = 1$ mL s^{-1} and $\omega = 3$ mL s^{-1} are shown in Figures 48 (a) and (b), respectively. The other parameter values are given in Appendix (A). The increase in the flow velocity by a factor of three reduces the volume fraction of gas by a factor of three.

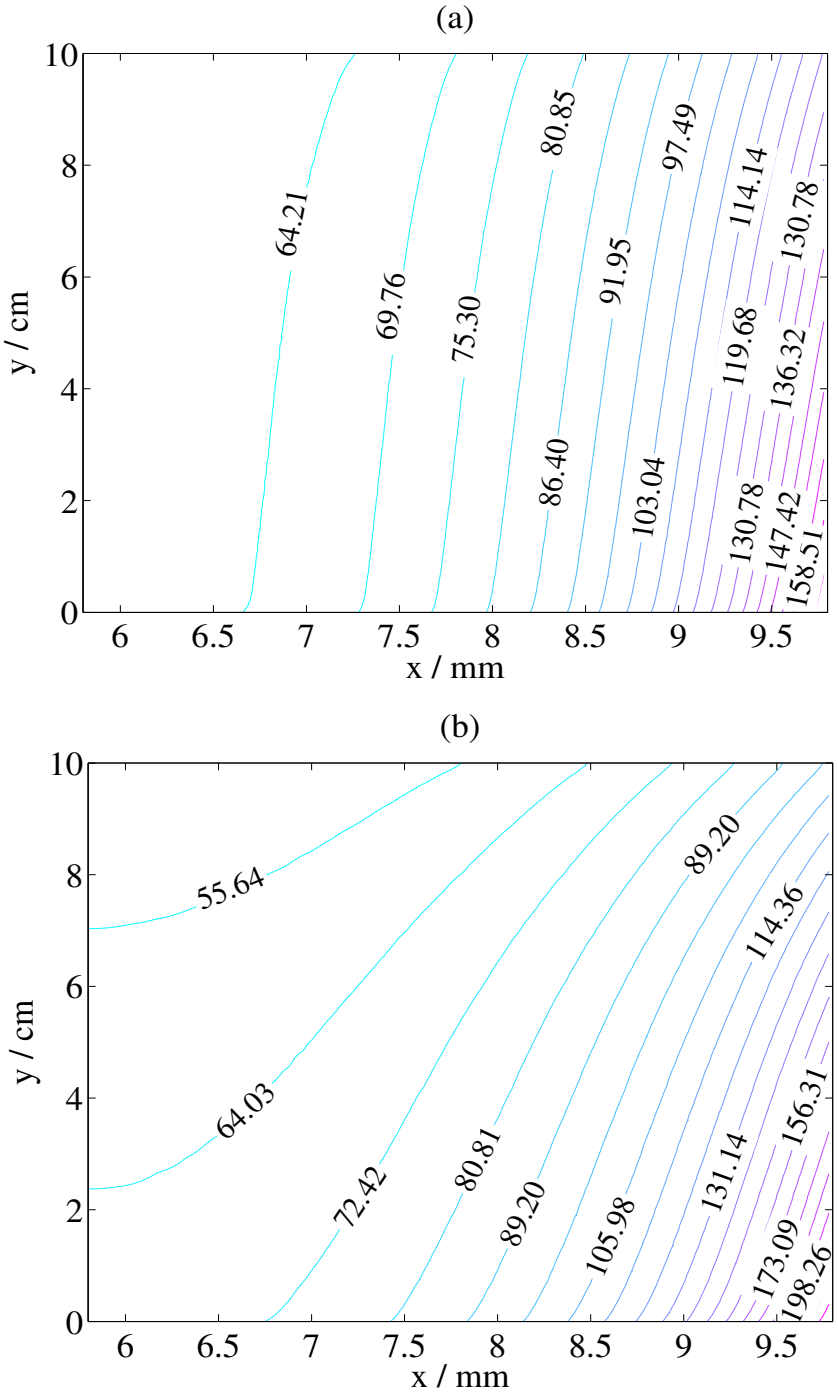

Figure 46: Plots of the redox reaction current density, $\nabla \cdot \vec{j} = j_1$ (in mA m^{-2}) in the positive electrode at the end of charge ($t = 33.67$ min), (a) with and (b) without O_2 evolution. In these calculations, $c_3^0 = c_4^0 = 1080$ mol m^{-3}, $I_{\text{app}} = 10$ A, $d_g = 50$ μm, $\omega = 1$ mL s^{-1} and $T_0 = 298$ K. The other parameter values are given in Appendix (A).

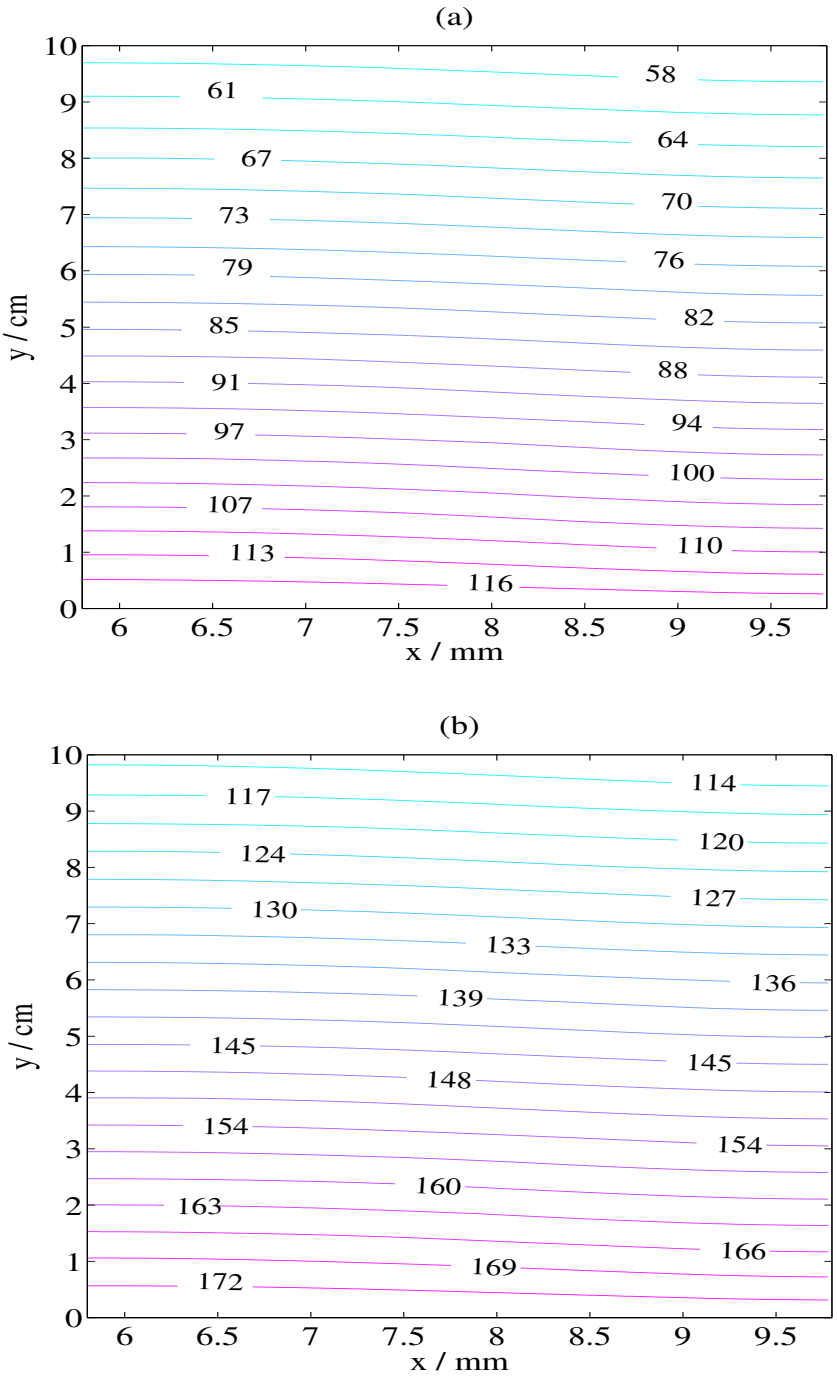

Figure 47: The V(V) concentration (in mol m^{-3}) in the positive electrode during discharge at $t = 64.33$ min, (a) with and (b) without oxygen evolution. In these calculations, $c_3^0 = c_4^0 = 1080$ mol m^{-3}, $I_{app} = 10$ A, $d_g = 50$ μm, $\omega = 1$ mL s^{-1} and $T_0 = 298$ K. The other parameter values are given in Appendix (A).

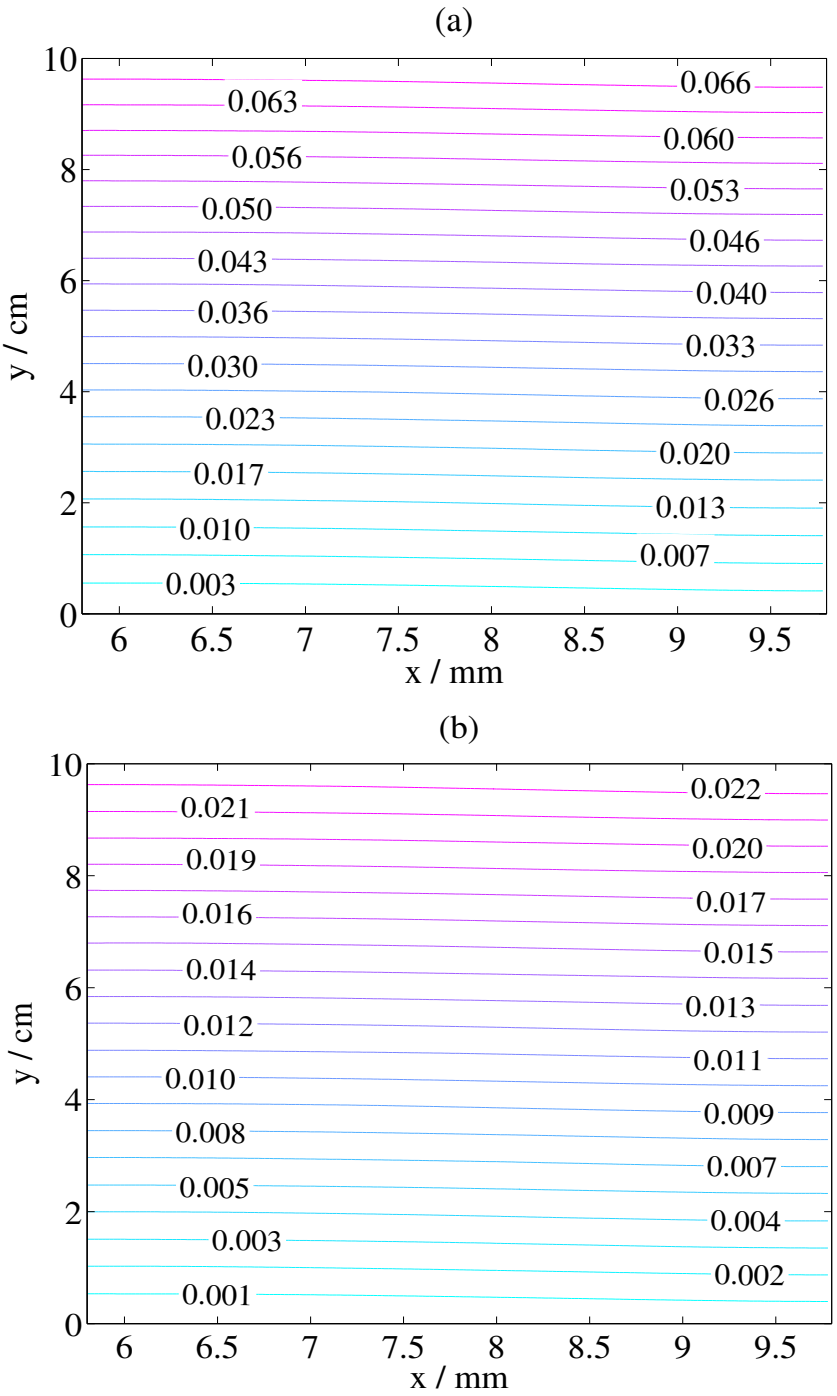

Figure 48: Contour plots of the gas volume fraction, β_g in the positive electrode at the end of the charge ($t = 33.67$ min and $t = 33.8$ min) for the cases (a) $\omega = 1$ mL s^{-1} and (b) $\omega = 3$ mL s^{-1}, respectively. In these simulations, $c_3^0 = c_4^0 = 1080$ mol m^{-3}, $I_{\text{app}} = 10$ A, $d_g = 50$ μm and $T_0 = 298$ K. The other parameter values are given in Appendix (A).

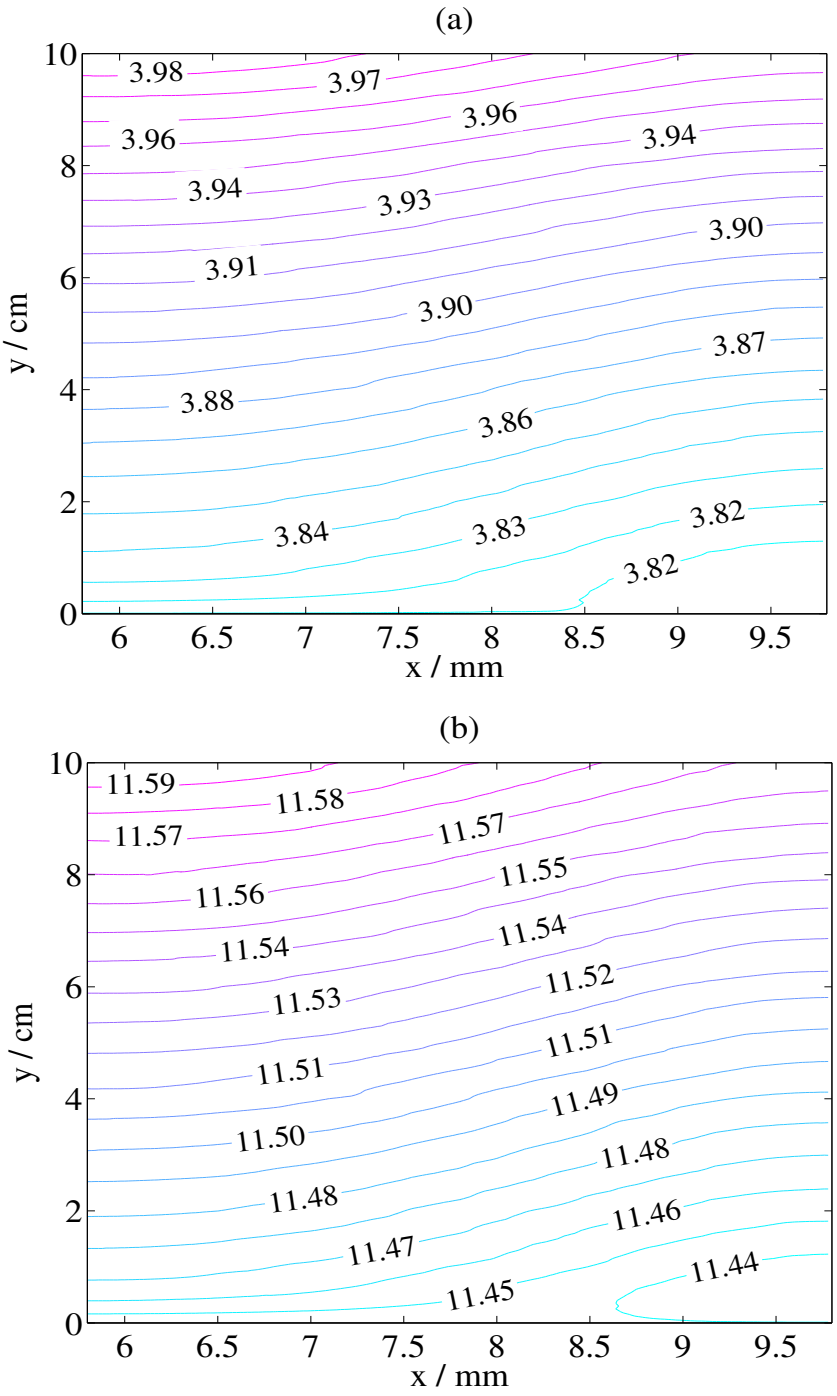

Figure 49: Contour plots of the y component of the gas velocity, v_g (in mm s^{-1}) in the positive electrode at the end of the charge ($t = 33.67$ min and $t = 33.8$ min) for the cases (a) $\omega = 1$ mL s^{-1} and (b) $\omega = 3$ mL s^{-1}, respectively. In these simulations, $c_3^0 = c_4^0 = 1080$ mol m^{-3}, $I_{\text{app}} = 10$ A, $d_g = 50$ μm and $T_0 = 298$ K. The other parameter values are given in Appendix (A).

The value of β_g increases as the height above the inlet surface increases along any vertical line. The assumption of an inlet free of bubbles maintains a zero value of β_g at the inlet, $y = 0$. The degree of variation of the gas volume fraction in the horizontal direction is minimal since the flow is convection dominated in the vertical direction. The maximum value in the gas volume fraction, attained at the outlet surface, is approximately 68% lower at the higher flow rate, $\omega = 3$ mL s^{-1}. A decrease in the gas volume fraction, with other conditions fixed, would decrease the slip velocity, $\vec{u}_{\text{slip}} = (u_{\text{slip}}, v_{\text{slip}})$ given by equation (61), with the pressure gradient given by equation (53) [96]. As the gas volume fraction decreases, the Kozeny-Carman factor in the relative permeability in equation (53) increases, resulting in a higher liquid velocity and a smaller value of ∇p; the reduced volume of liquid lowers the permeability and increases pressure gradients. In Figure 49 (a), therefore, the y component of the gas velocity, v_g is 11.8 % higher than the initial liquid velocity (3.57 mm s^{-1}), while in Figure 49 (b), v_g is only 8.2 % higher than the initial liquid velocity (10.71 mm s^{-1}), *i.e.*, the departure of the gas velocity from the liquid velocity (the slip velocity) is relatively smaller at the higher flow rate. The increase in the liquid velocity, however, is the dominant effect, which leads to the much lower gas volume fraction for $\omega = 3$ mL s^{-1}.

Figures 50 (a) and (b) show contours of the O_2 evolution current density, j_{O_2}, and the O_2 evolution overpotential, η_{O_2}, respectively, at the end of charge ($t = 33.8$ min) for $\omega = 3$ mL s^{-1} (to be compared with Figures 44 (b) and 45 (b), respectively). The higher flow rate leads to a more even distribution of reactant and, consequently lower overpotential values. Thus, the O_2 evolution rate is decreased (compared to Figure 50 (a)). This leads to a further reduction in the O_2 volume fraction, though this reduction is small in comparison to the reduction caused by the higher liquid velocity.

6.3 Influence of Bubble Diameter

Simulations were performed using values of $d_g = 25$ μm and $d_g = 100$ μm (to an equivalent SOC) with other parameter values as in the base case in which $d_g = 50$

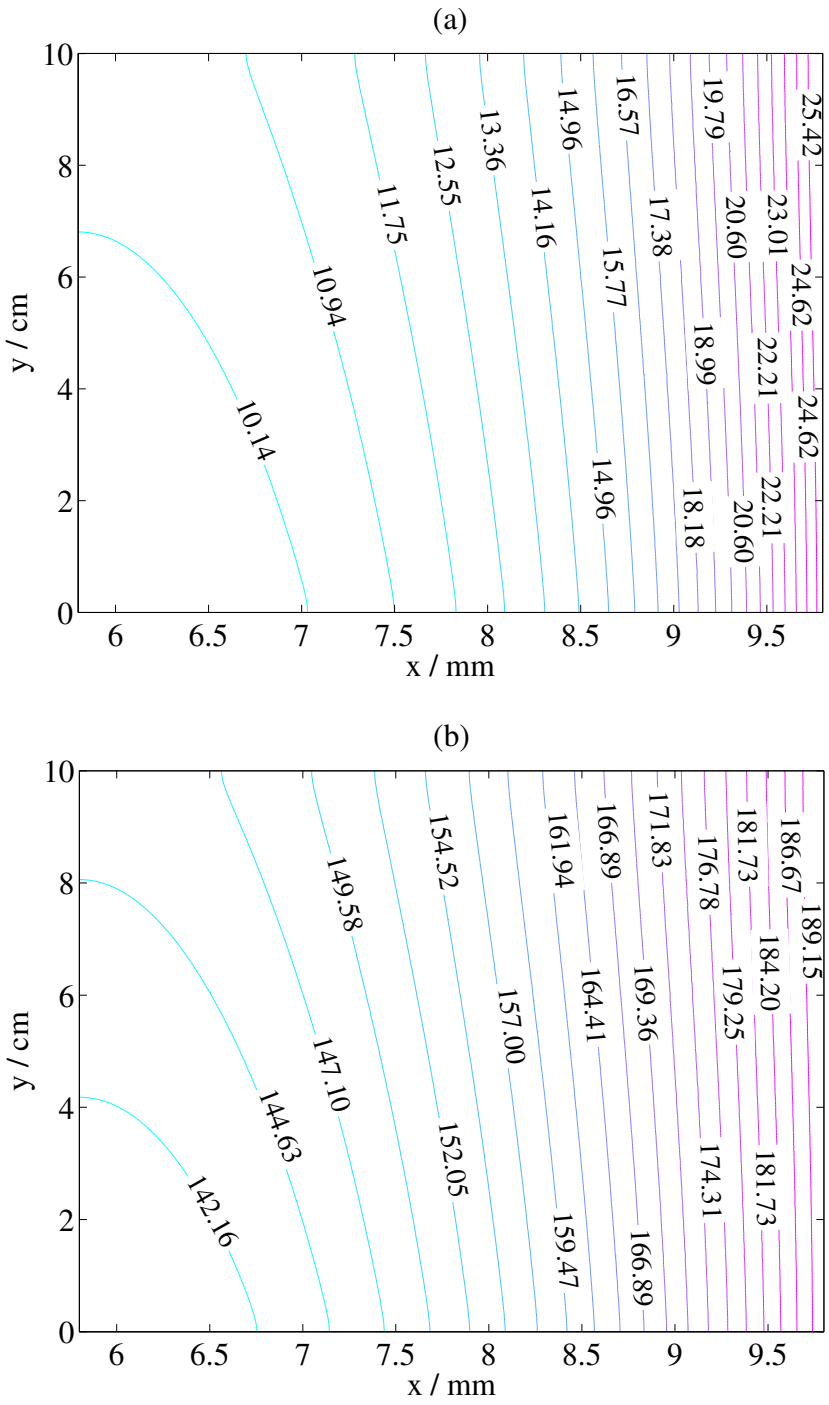

Figure 50: (a) Contour plots of the O_2 evolution current density, j_{O_2} (in mA m^{-2}) and (b) the corresponding O_2 evolution overpotential, η_{O_2} (in mV) at the end of the charge in the positive electrode for $\omega = 3$ mL s^{-1}. In these simulations, $c_3^0 = c_4^0 = 1080$ mol m^{-3} $I_{\text{app}} = 10$ A, $d_g = 50$ μm and $T_0 = 298$ K. The other parameter values are given in Appendix (A).

μm (Figures 42 and 43). Figures 51 (a) and (b) show the distribution of the O_2 volume fraction, β_g in the positive electrode at the end of charge ($t \approx 33.7$ min in all cases). As was the case for $d_g = 50$ μm, the value of β_g increases as the height above the inlet surface increases considerably along any vertical line, whereas its degree of variation in the horizontal direction is minimal. The maximum value of the gas fraction, β_g, attained at the outlet, is decreased by approximately 27 % as the bubble diameter increases from $d_g = 25$ μm to $d_g = 100$ μm.

The lower gas volume fraction for the larger diameter is caused by a considerably greater slip velocity, as indicated by Figures 52 (a) and (b), which show the y component of the slip velocity, v_{slip} for the two diameters. Equation (61) suggests that the slip velocity increases with an increase in the bubble diameter, for a fixed pressure gradient. The gas velocity, which is the sum of the liquid and slip velocities is, therefore, increased. From a physical perspective, the drag force is proportional to surface area of the bubble (or d_g^2) and the buoyancy force is proportional to the bubble volume (or d_g^3). Larger bubbles, therefore, induce a higher slip velocity through an increased net force. The higher gas velocity removes the bubbles at a faster rate, thereby lowering the gas volume fraction.

6.4 Influence of Operating Temperature

Figure 53 (a) shows the simulated cell voltage curves during a charge/discharge cycle for three operating temperatures, $T_0 = 288$ K, 298 K and 313 K for the aforementioned base case. The other parameter values are given in Appendix (A). In all three cases the system is assumed to be adiabatic. In each case, charging was terminated at the same time of 33.67 min. The state of charge was estimated to be 0.9, 0.87 and 0.73 from the lowest to the highest temperature, respectively. As the temperature increases, the cell voltage decreases during charge and increases during discharge, *i.e.*, the departure from the OCV decreases. The capacity of the battery (at the constant charge time) decreases markedly between $T_0 = 298$ K and $T_0 = 313$ K, with only a small decrease between $T_0 = 288$ K and $T_0 = 298$ K. The charge efficiency of the battery decreases from 92 % at an operating temperature of $T_0 = 288$ K to 77 % at

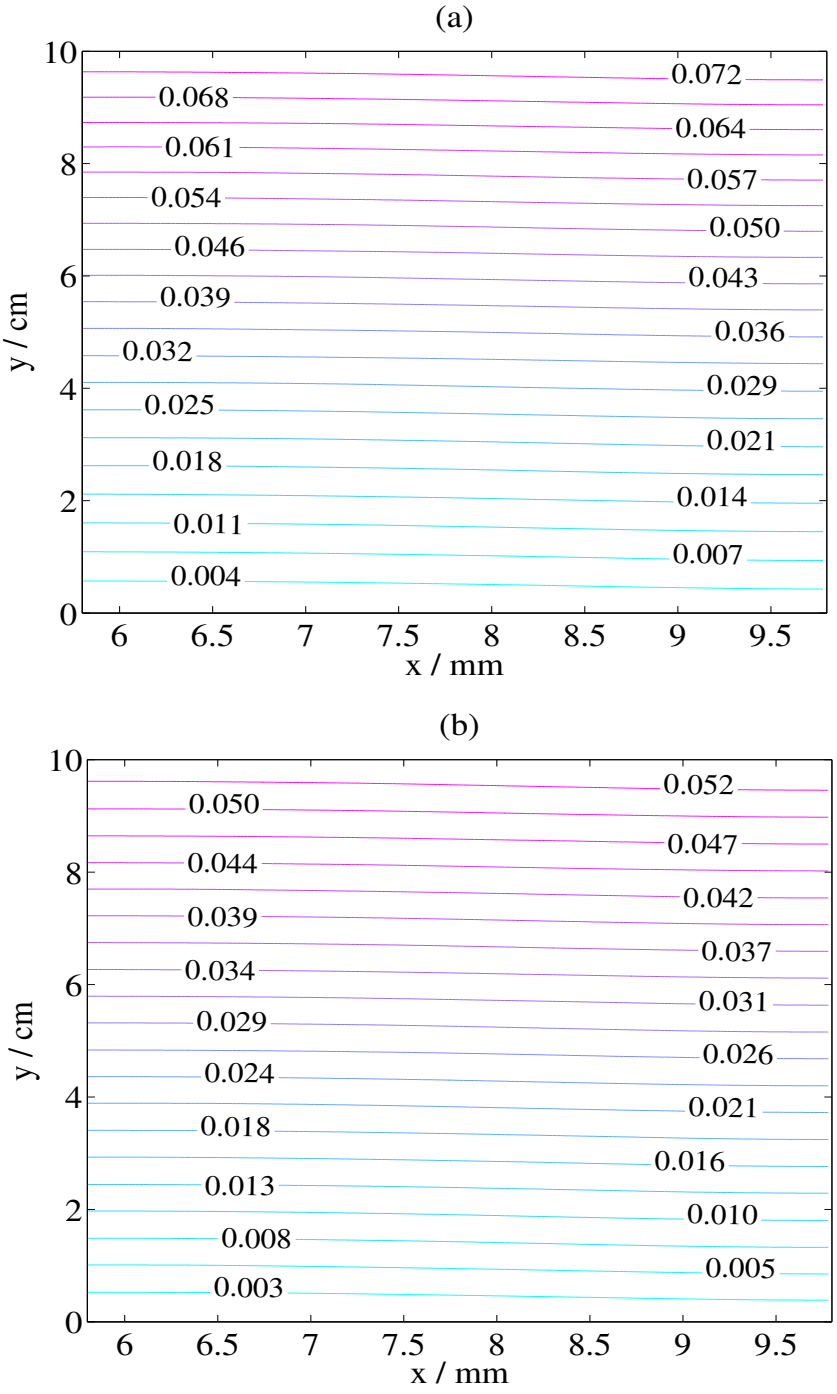

Figure 51: Contour plots of the oxygen gas volume fraction, β_g in the positive electrode at the end of charge for two gas bubble diameters, (a) $d_g = 25$ μm and (b) $d_g = 100$ μm. In these simulations, $c_3^0 = 1080$ mol m^{-3}, $I_{\text{app}} = 10$ A, $\omega = 1$ mL s^{-1} and $T_0 = 298$ K. The other parameter values are given in Appendix (A).

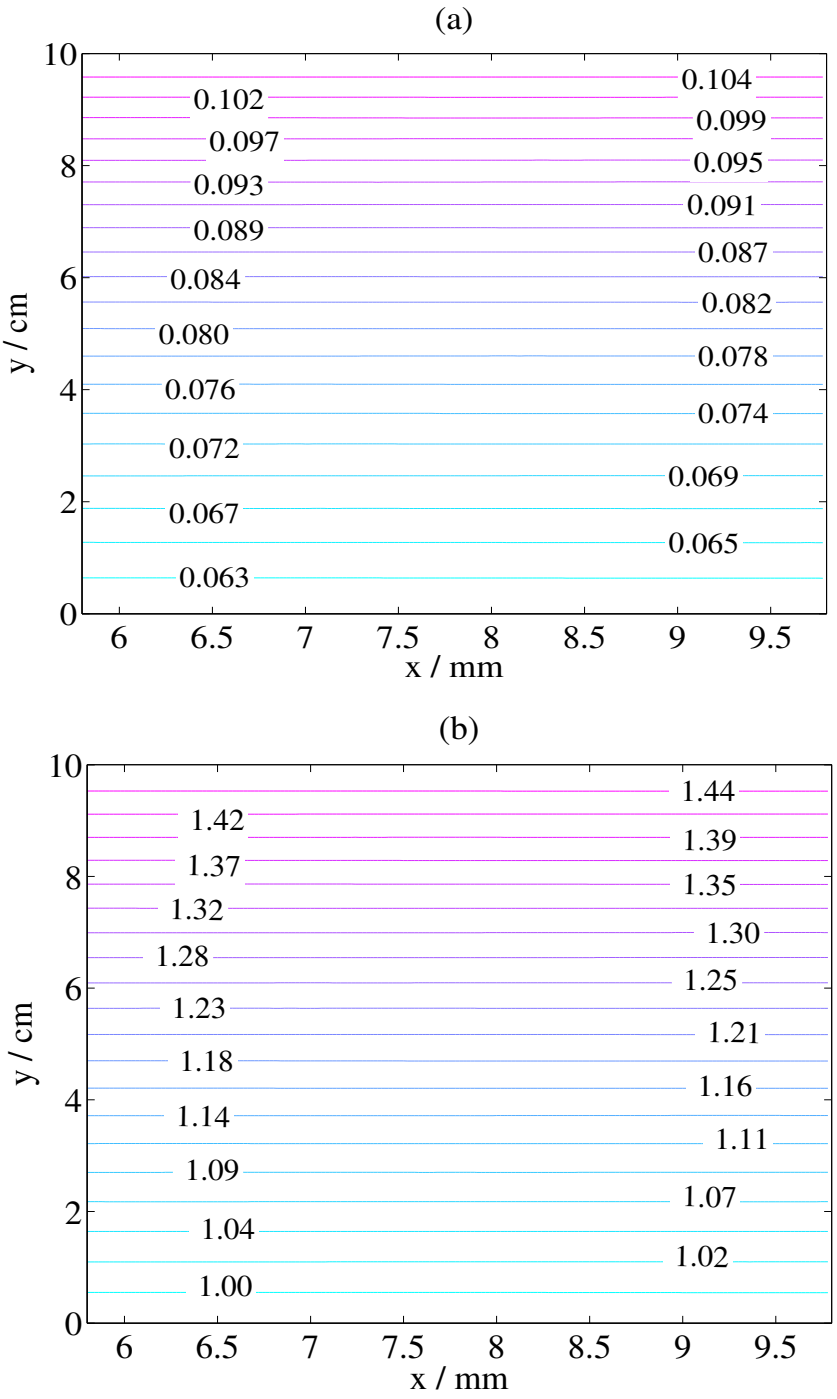

Figure 52: Contour plots of the y component of the slip velocity, v_{slip} (in mm s^{-1}) in the positive electrode at the end of charge for two gas bubble diameters, (a) $d_g = 25$ μm and (b) $d_g = 100$ μm. In these simulations, $c_3^0 = 1080$ mol m^{-3}, $I_{\text{app}} = 10$ A, $\omega = 1$ mL s^{-1} and $T_0 = 298$ K. The other parameter values are given in Appendix (A).

$T_0 = 313$ K.

The decreased deviation of the cell voltage from OCV with increasing temperature is due to several factors [95]. The equilibrium potentials given by equations (84) and (96) decrease in magnitude, for fixed initial concentrations of the reactants, the cell voltage at $t \approx 0$ in Figure 53 (a) decreases as the temperature is increased. An increased temperature increases the rate constants, k_i given in equation (97). An increased reaction rate constant leads to an decrease in the magnitude of the overpotential, in the absence of other effects such as gas evolution, in order to maintain the (fixed) applied current, as is seen from the Butler-Volmer equations (82).

Note that the potential-dependent exponential in the Butler-Volmer equations would tend to decrease with an increase in temperature, for a fixed potential, which would tend to require an increase in the magnitude of the overpotential. The increase in the reaction constant, however, dominates this effect due to the large activation energies in equation (97). With gas evolution included, an increase at a fixed current density in one or both of the rate constants for the two reactions (1) and (3) will, in the absence of other variations, lower the overpotentials η_{O_2} and η_1, which differ by the difference between the equilibrium potentials for the reactions: $\eta_{O_2} = \eta_1 + E'_{0,1} - E_{0,O_2}$.

Figures 54 (a) and (b) show the gas volume fraction, β_g at the end of the charge time ($t = 33.67$ min) for the two temperatures $T_0 = 288$ K and $T_0 = 313$ K (compared with Figure 48 (a)). The maximum in the volume fraction increases from approximately 3.2 % to approximately 13 % from the lower to the higher temperature. This is despite an increase in the gas velocity, the y component of which, v_g is shown in Figures 55 (a) and (b) for the two temperatures $T_0 = 288$ K to $T_0 = 313$ K, respectively, at the end of charge; the maximum in v_g increases by 8.5 % from $T_0 = 288$ K to $T_0 = 313$ K.

The increase in the gas velocity is due to the increased gas volume fraction, which increases the slip velocity as described above. The increase in β_g is due to the increase in the value of the O_2 evolution current density. Figures 56 (a) and (b) show contours of the O_2 evolution current density, j_{O_2} (in mA m^{-2}) in the positive electrode at the end of charge ($t = 33.67$ min). As the operating temperature increases from

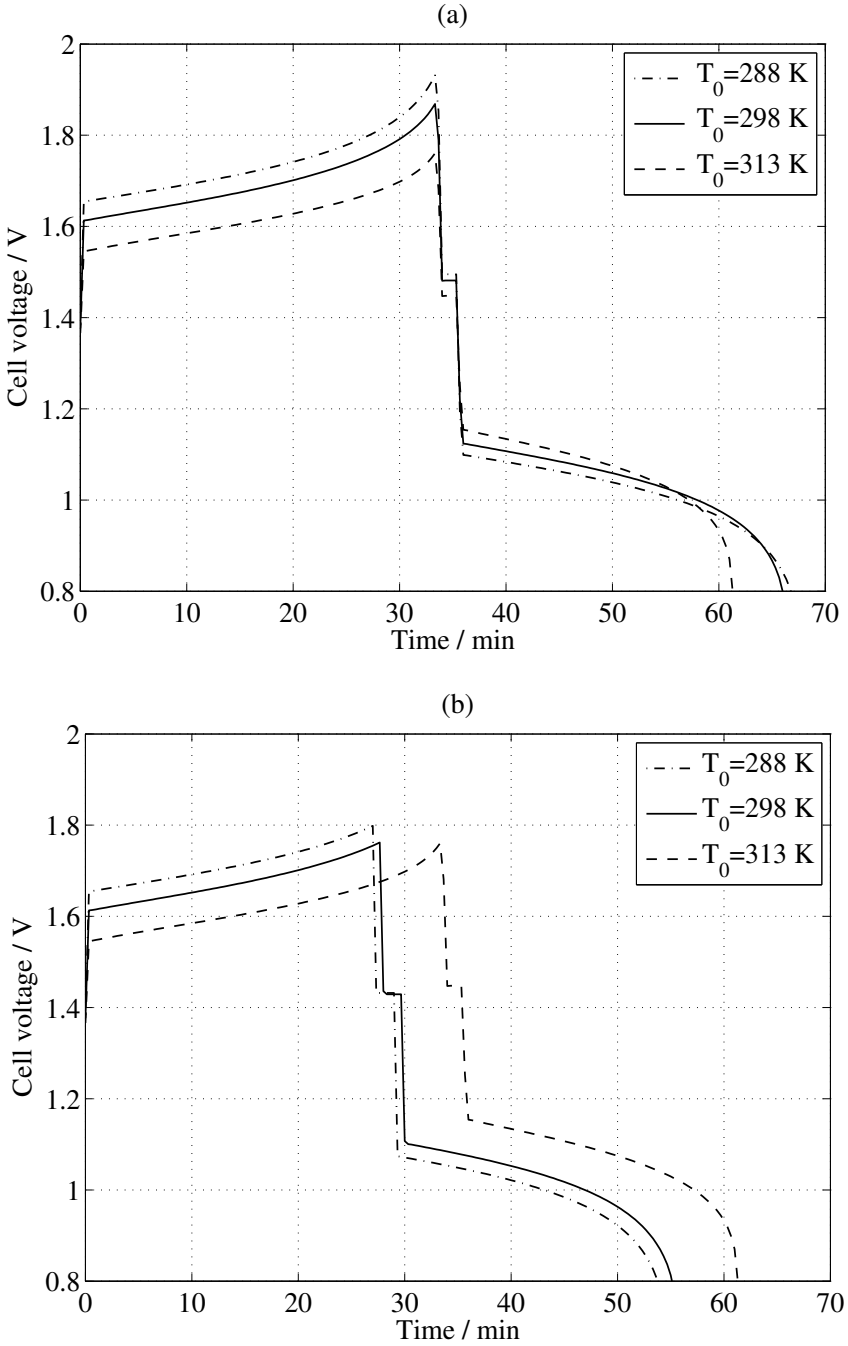

Figure 53: (a) A comparison between simulated cell voltage, E_{cell} curves at three operating temperatures, $T_0 = 288$ K, 298 K and 313 K, using the same charge time in each case (33.67 min). (b) cell voltage (in V) curves at the three operating temperatures with the charge time defined by SOC=0.73 in each case In all simulations, $c_3^0 = c_4^0 = 1080$ mol m^{-3}, $I_{\text{app}} = 10$ A, $\omega = 1$ mL s^{-1} and $d_g = 50$ μm. The other parameter values are given in Appendix (A).

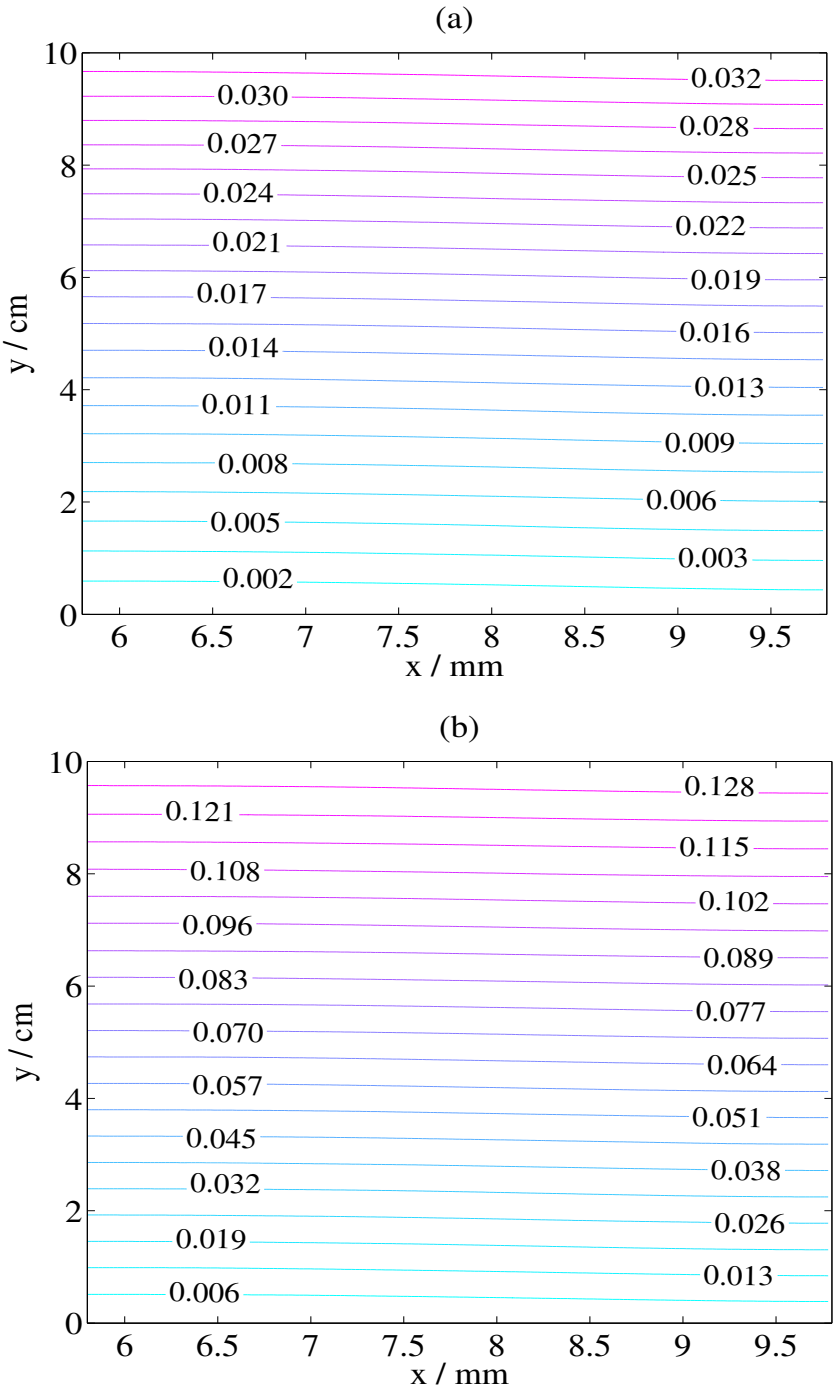

Figure 54: Contour plots of the oxygen gas volume fraction, β_g in the positive electrode at the end of charge ($t = 33.67$ min) for (a) $T_0 = 288$ K and (b) $T_0 = 313$ K, corresponding to Figure 53 (a). In these calculations, $c_3^0 = 1080$ mol m^{-3}, $I_{\text{app}} = 10$ A and $\omega = 1$ mL s^{-1}. The other parameter values are given in Appendix (A).

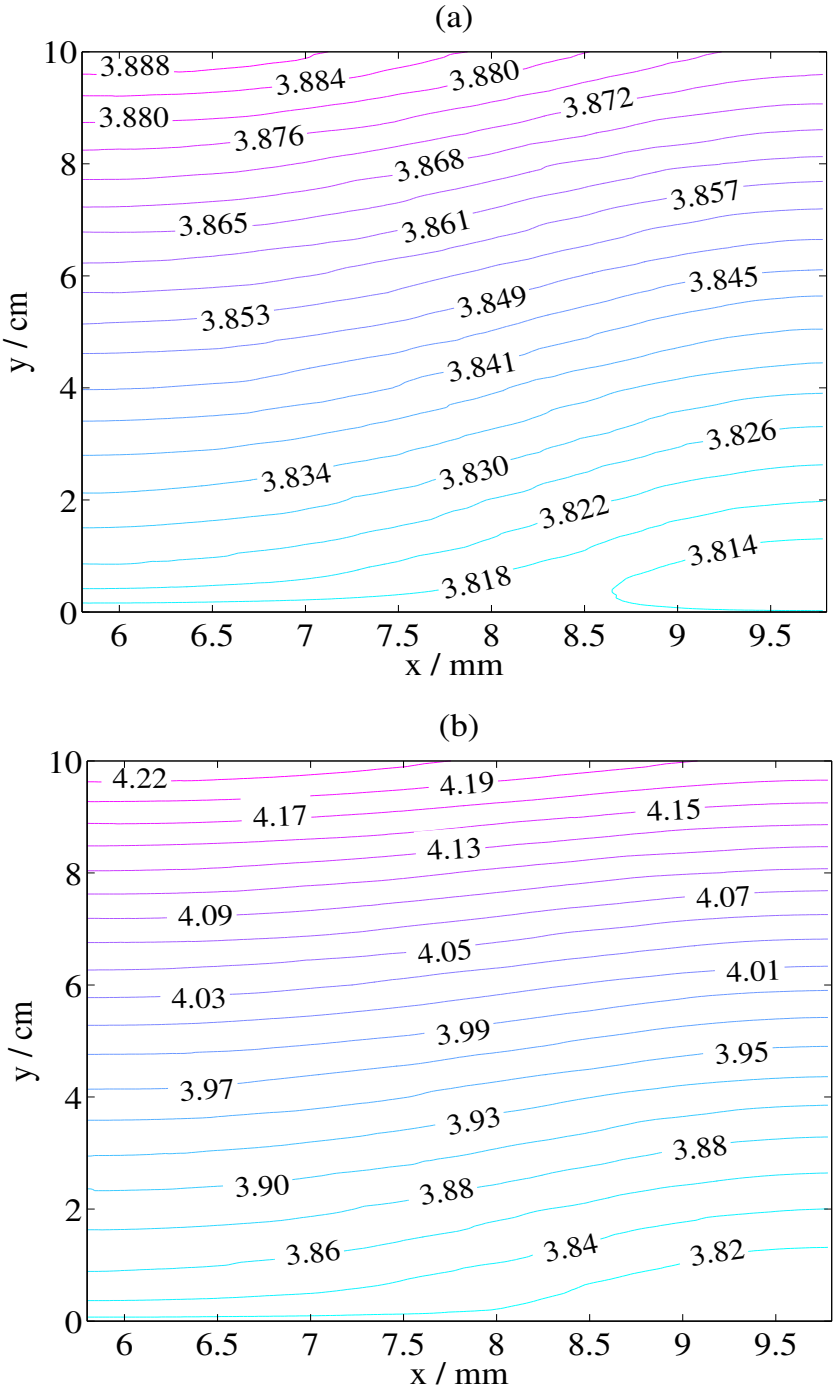

Figure 55: Contour plots of the y component of the gas velocity, v_g (in mm s^{-1}) in the positive electrode at the end of charge ($t = 33.67$ min) for (a) $T_0 = 288$ K and (b) $T_0 = 313$ K. In these calculations, $c_3^0 = 1080$ mol m^{-3}, $I_{app} = 10$ A and $\omega = 1$ mL s^{-1}. The other parameter values are given in Appendix (A).

$T_0 = 288$ K to 313 K, the maximum value of the O_2 evolution current density increases by more than 350 %, on the order of the increase in the gas volume fraction.

In contrast, Figures 57 (a) and (b) show that O_2 evolution overpotential in the positive electrode, η_{O_2} at the end of the charge decreases by as much as 148 mV as the temperature is increased from $T_0 = 288$ K to 313 K. The rate constant for the O_2 evolution reaction, given in equation (98) depends exponentially on temperature. The increase in the overpotential value at the lower temperature is outweighed by the decrease in the reaction rate constant, which leads to much lower values of j_{O_2}.

Figure 53 (b) shows the cell voltage curves at three temperatures when the charge phase is terminated at an equivalent state of charge (SOC=0.73) in all cases. As the temperature is raised, the O_2 evolution reaction consumes a greater portion of the applied current density, leading to increasingly longer (charge) times to the same SOC: 27.07 min, 27.93 min and 33.67 min, in order of ascending temperature. The trend in these values reflects the exponential increase in the rate constant for the O_2 reaction with temperature, as does the plot of the maximum gas volume fraction shown in Figure 58 (a). The slip velocity increases as a consequence, which will partially offset the increase in β_g (Figure 58 (b)). Also evident from Figure 53 (b) is that the charge efficiencies at the different temperatures are roughly similar since the capacity of the battery at the end of charge is theoretically the same in each case.

6.5 Oxygen Evolution Parameters

The electrochemical parameters for O_2 evolution will clearly depend on the electrode material. To provide an indication of the differences between O_2 evolution on different materials, and to confirm that the behaviour described above is robust to changes in the parameter values, calculations were performed with different j_{ref,O_2} values (all other parameters unchanged). Figure 59 shows the cell voltage curves during charge for all cases. The O_2 volume fractions at the end of charge for $j_{\mathrm{ref},O_2} = 1 \times 10^{-10}$ A m^{-2} and 1×10^{-8} A m^{-2} are plotted in Figure 60. These figures show that, as expected, an increased value of j_{ref,O_2} leads to a greater decrease in the cell voltage, as a consequence of a increased current consumed by the parasitic O_2 evolution reaction

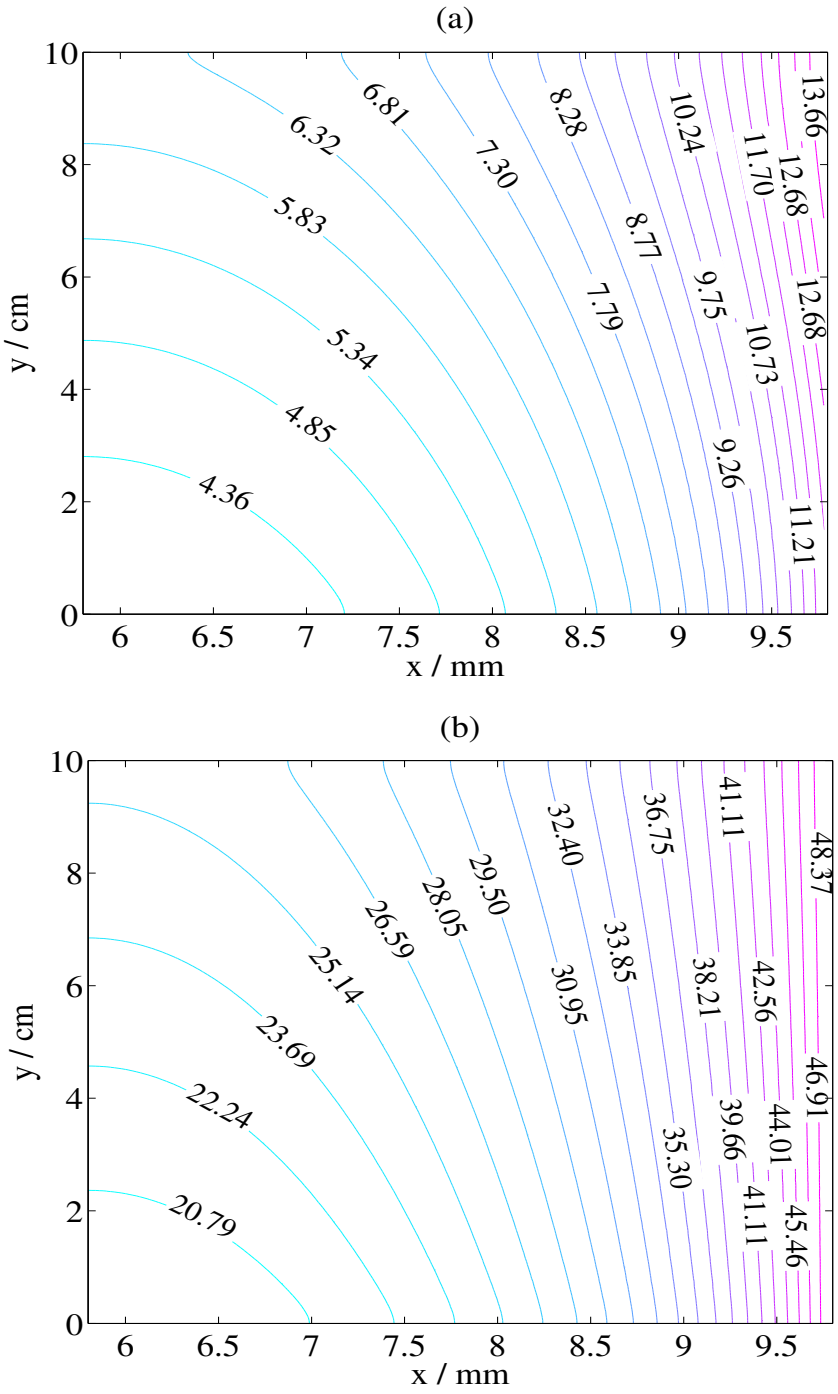

Figure 56: Plots of the O_2 evolution current density, j_{O_2} (in mA m^{-2}) in the positive electrode at the end of charge (t = 33.67 min) at (a) T_0 = 288 K and (b) T_0 = 313 K, corresponding to Figure 53 (a). In these calculations, $c_3^0 = c_4^0$ = 1080 mol m^{-3}, I_{app} = 10 A, d_g = 50 μm, ω = 1 mL s^{-1} and T_0 = 298 K. The other parameter values are given in Appendix (A)

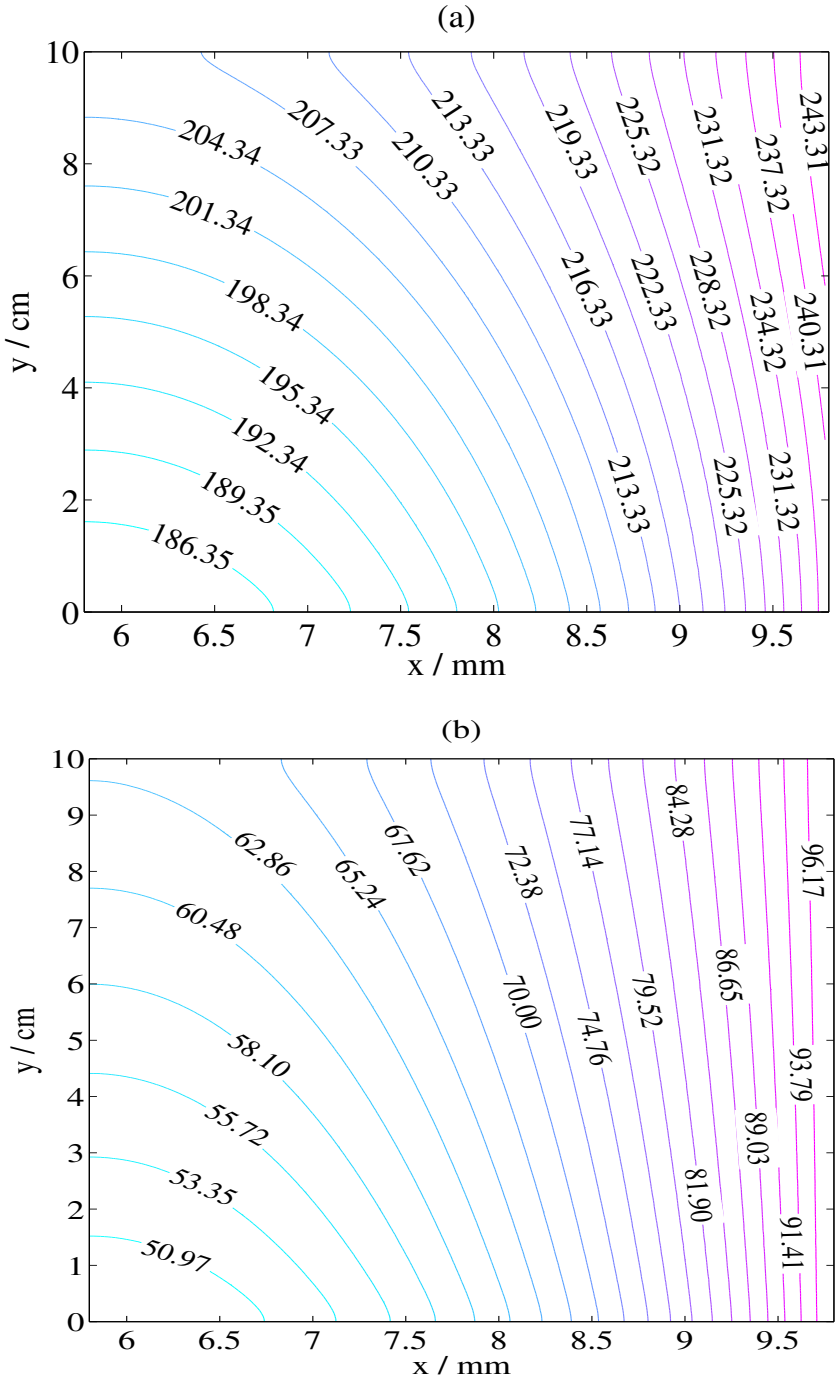

Figure 57: Plots of the O_2 evolution overpotential, η_{O_2} (in mV) in the positive electrode at the end of charge ($t = 33.67$ min) at (a) $T_0 = 288$ K and (b) $T_0 = 313$ K. In these calculations, $c_3^0 = c_4^0 = 1080$ mol m^{-3}, $I_{\text{app}} = 10$ A, $d_g = 50$ μm, $\omega = 1$ mL s^{-1} and $T_0 = 298$ K. The other parameter values are given in Appendix (A)

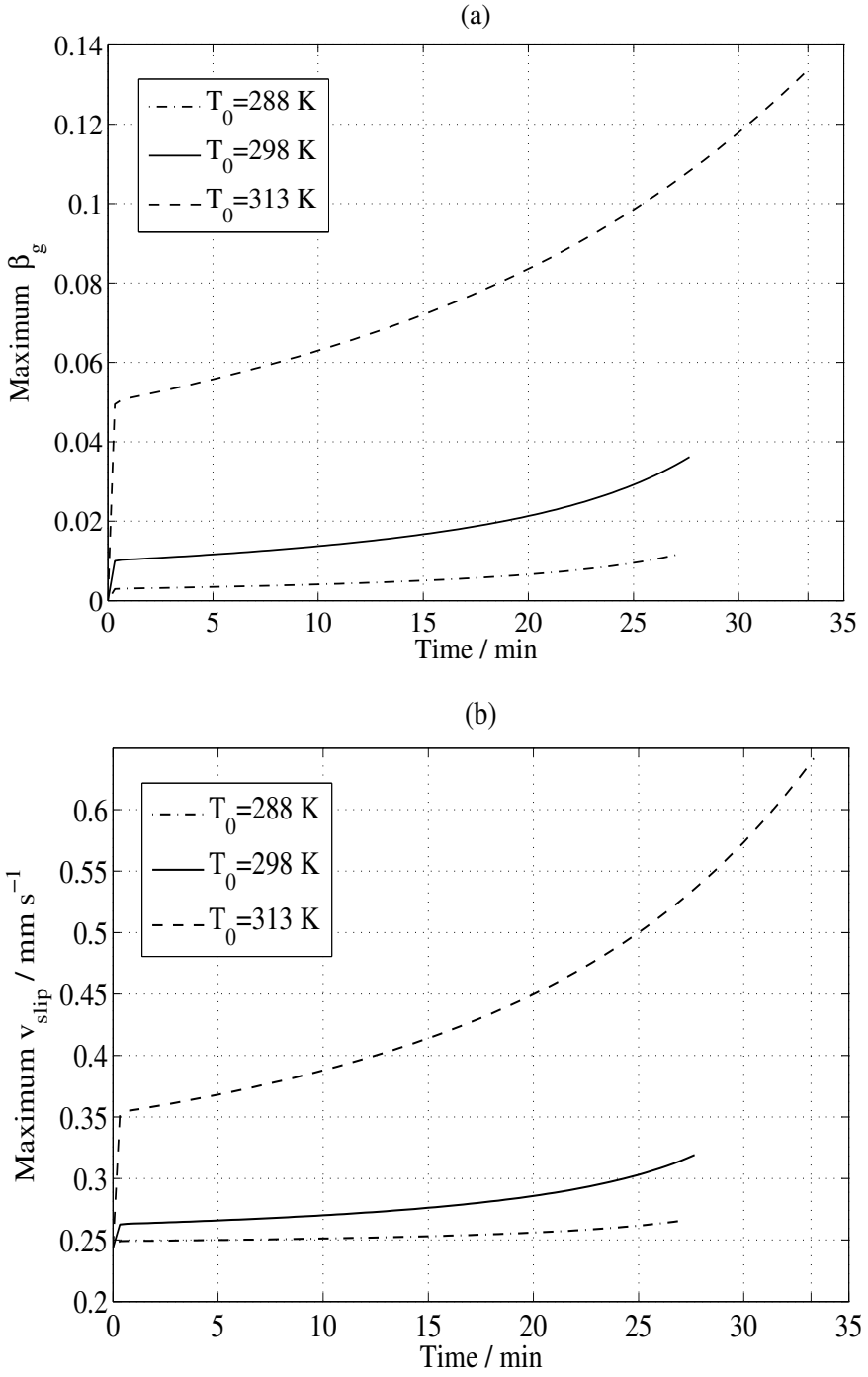

Figure 58: Plots of the maximum value of: (a) the gas volume fraction, β_g; (b) the y component of the slip velocity, v_{slip} (in mm s^{-1}) in the positive electrode during the charge cycles (to SOC=0.73) at different temperatures in Figure 53 (b). In these calculations, $c_3^0 = c_4^0 = 1080$ mol m^{-3}, $I_{\text{app}} = 10$ A, $d_g = 50$ μm and $\omega = 1$ mL s^{-1}. The other parameter values are given in Appendix (A).

and a greater volume of O_2. The results discussed in previous sections, however, are qualitatively unchanged.

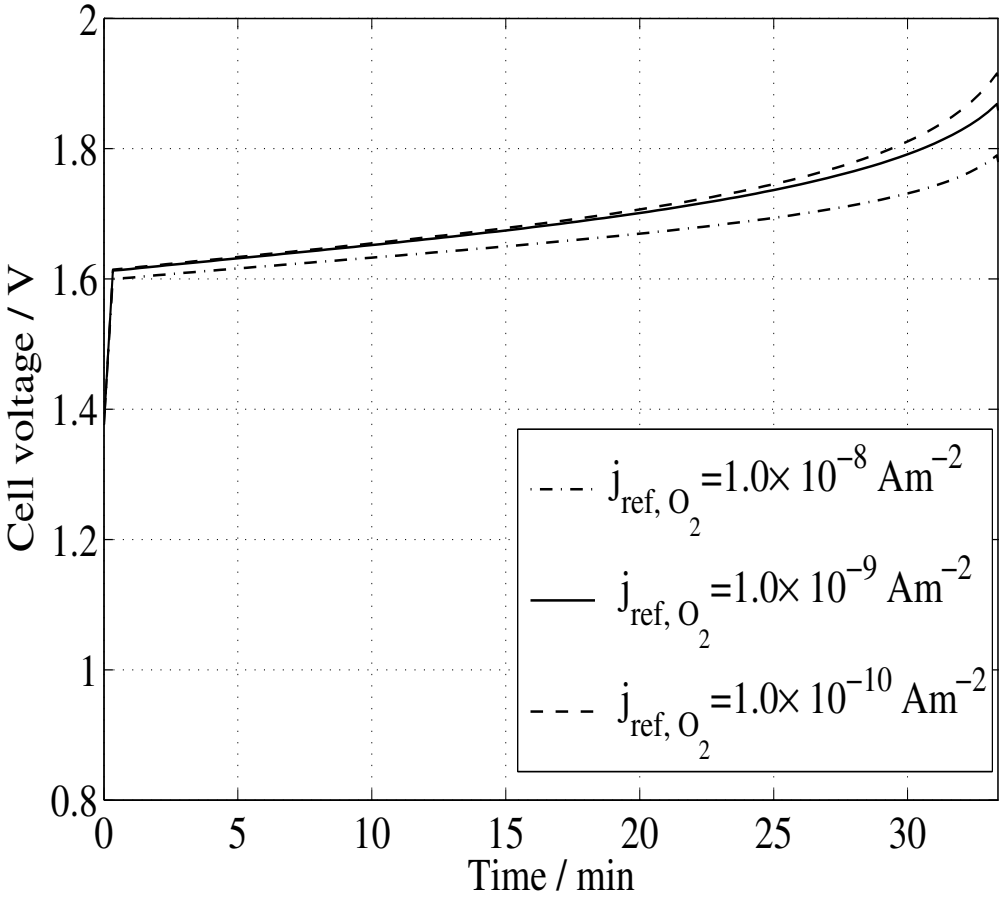

Figure 59: The cell voltage curves during charge for different values of $j_{\mathrm{ref,O_2}}$. In these calculations, $c_3^0 = c_4^0 = 1080$ mol m^{-3}, $I_{\mathrm{app}} = 10$ A, $\omega = 1$ mL s^{-1}, $d_g = 50$ μm and $T_0 = 298$ K. The other parameter values are given in Appendix (A).

6.6 Conclusions

Comparison between numerical simulations and experimental data, for different vanadium concentrations and electrolyte flow rates, demonstrate good qualitative and quantitative agreement.

Increasing the mean linear electrolyte flow rate was found to reduce the volume of the oxygen gas evolved in the positive electrode. This is due mainly to the increased

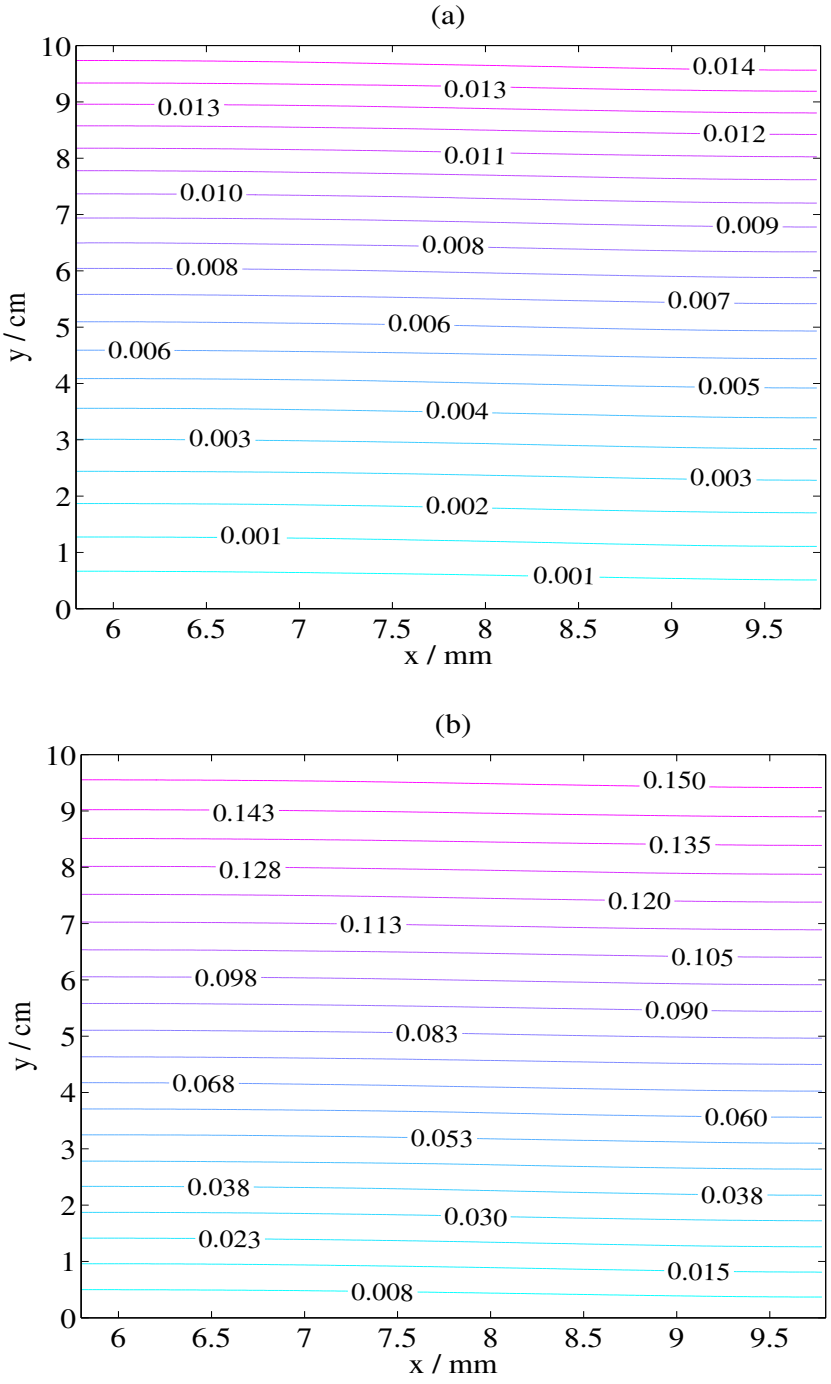

Figure 60: The O_2 volume fraction for (a) $j_{\mathrm{ref},O_2} = 1 \times 10^{-10}$ A m^{-2} and (b) 1×10^{-8} A m^{-2}. In these calculations, $c_3^0 = c_4^0 = 1080$ mol m^{-3}, $I_{\mathrm{app}} = 10$ A, $\omega = 1$ mL s^{-1}, $d_g = 50$ μm and $T_0 = 298$ K. The other parameter values are given in Appendix (A).

rate at which the gas is removed from the cell since the flow is convection dominated. The lower overpotentials achieved with a higher flow rate further reduce the gas volume fraction.

The oxygen gas volume fraction and velocity are strongly influenced by the bubble diameter. The slip velocity increases with bubble diameter as a result of a greater buoyancy force exerted on the bubbles. The gas volume fraction decreases as the gas is removed at a faster rate. Substantial changes are observed over the range of reported bubble diameters.

Increasing the operating temperature was found to enhance O_2 evolution and, therefore, increase the volume of gas in the positive electrode. The exponential dependence of the reaction rate constant for O_2 evolution outweighs several competing factors, including increases in the slip velocity and the magnitudes of the overpotentials, to increase the gas volume fraction at higher temperatures.

Since the rate of evolution is enhanced at higher temperature, and the onset occurs sooner in the charge cycle, at fixed values of the other parameters, the rate of oxidation in the positive electrode decreases at any fixed time. Thus, the time required to reach an equivalent state of charge (charge time) increases with temperature. The charge efficiency of the cell drops markedly as a consequence. The drop in efficiency is nonlinear since the main factor associated with the drop (the O_2 reaction constant) has an exponential dependence on temperature.

Chapter 7
Conclusions and Recommendations for Further Work

7 Conclusions and Recommendations for Further Work

7.1 Conclusions

One of the benefits of modelling is the ability to predict quantities that can be difficult, in some cases impossible to obtain through *in-situ* experimental measurements. This information, however, can be of vital importance to ensuring both good performance and longevity of the battery-knowledge of the likelihood of localised reactant depletion, localised heating and of a steep rise in potential.

A non-isothermal two-dimensional dynamic model of an all-vanadium redox flow battery based on mass, charge, energy and momentum transport and conservation, together with a kinetic model for redox and gas evolving reactions has been developed. The impact of gas evolution and gas bubble formation in the positive and negative electrodes during charge on the performance was investigated. Evolved gas, in the form of bubbles, impacts performance by reducing the active surface area for electrochemical reaction in the electrode, reducing the effective diffusion coefficients, lowering the effective ionic and thermal conductivities and by altering the flow field. Comparison between numerical simulations and experimental data, for different vanadium concentrations and electrolyte flow rates, demonstrate good qualitative and quantitative agreement.

High temperatures are harmful to perfluorinated membranes, such as Nafion®, [147, 166, 167], can enhance corrosion of the plates and can lead to water loss. The numerical simulations conducted in this thesis suggest that without heat dissipation from the cell, the temperature would rise to unacceptable levels in a relatively short period of time. In order to avoid large temperature increases an effective cooling

strategy is required for operation in high-temperature environments and under high loads.

Increasing the operating temperature was found to enhance O_2 evolution and, therefore, increase the volume of gas in the positive electrode. The exponential dependence of the reaction rate constant for O_2 evolution outweighs several competing factors, including increases in the slip velocity and the magnitudes of the overpotentials, to increase the gas volume fraction at higher temperatures. Since the rate of evolution is enhanced at higher temperature, and the onset occurs sooner in the charge cycle, at fixed values of the other parameters, the rate of oxidation in the positive electrode decreases at any fixed time. Thus, the charge time required to reach an equivalent state of charge increases with temperature. The charge efficiency of the cell drops markedly as a consequence. The drop in efficiency is nonlinear since the main factor associated with the drop, at constant O_2 reaction has an exponential dependence on temperature.

The formation of oxygen and hydrogen gas bubbles reduces the efficiency of the battery by consuming a portion of the applied current, reducing the amount of current available for the oxidation of V(IV) in the positive electrode and for the reduction of V(III) in the negative electrode.

The mean linear electrolyte flow rate appears to strongly affect the volume of gas in the electrodes during charge, by virtue of the rate of bubble removal through the outlet. A large electrolyte flow rate, combined with regulation of the external temperature, could be used to avoid the hot spots by keeping the temperature distribution uniform. Moreover, such high flow rates increase the coulombic efficiency of the cell and lower the rates of hydrogen and oxygen evolution.

The equivalent diameter of the bubbles was shown to exert a strong influence on the gas volume fraction. As the bubble diameter is increased, the gas velocity is enhanced by increased buoyancy, leading to a reduction in the gas volume fraction in the electrodes. The differences in the gas velocities and gas volume fractions between the smallest and largest reported values of the bubble diameter were found to be appreciable.

For an increasing applied current density it was found that the gas volume fraction inside the electrode increases, at a given state of charge. The results suggest that a high flow rate could be used to minimise this increase in gas volume. The value of the applied current for charge and discharge plays a crucial role in heat generation. The amount of heat generated and the timescale of the temperature rise do not increase linearly with the current. Regions of high temperature can form rapidly in the current collectors and electrodes due to large gradients in the electronic potential.

Heat loss can have a significant effect on the charge/discharge behaviour and temperature distribution of the cell. The results further highlight the need for an effective heat management strategy to maintain the desired cell temperature, particularly in environments where the temperature is not optimal.

7.2 Recommendations for Further Work

Considerable progress has been made in this thesis on modelling the complex process in VRFB. The framework developed can be extended to other flow battery systems with some modifications. Some specific extensions to the present work are:

- To develop the current work for modelling of the VRFB stacks, which are of commercial interest.

- To determine experimentally the values of the redox and gas evolution reactions constants, as well as the physical properties of the electrolyte as function of temperature. Moreover, to investigate the shape and size of the gas bubbles in each electrode.

- To include the time delay of flow rate of solution in the connecting pipes and the mixing time at the electrodes and reservoir in the model for practical design of the battery.

- Including the pH dependence for reaction (1) in Nernst equation will improve the trend matching of the simulated OCV curves with experimental curves.

More general extensions are:

- Multiscale modelling to investigate the behaviour (mass, charge, momentum, energy transport) and the performance for different pore geometries (*i.e.* different materials/constituents) and also to determine the effective material properties, which depend on phenomena at several length and time scales from atomic to macroscopic.

- Corrosion of the bipolar plates. Metal ions generated from the corrosion process can migrate to the membrane and other components of the cell, lowering their ionic conductivity values and engendering other side reactions such as chemical membrane degradation by promoting the production of the radicals ·OH and ·OOH.

- The modelling of other divided systems such as the vanadium chloride/polyhalide redox flow battery and the zinc-cerium redox flow battery, which involves a half-cell reaction requiring the efficient deposition and stripping of zinc metal. Moreover, the modelling of undivided (no membrane) redox flow batteries such as the dynamic lead-acid and cadmium-chloranil (tetrachloro-ρ-benzoquinone) cells. The systems may invoke the deposition/dissolution of metal ions on electrode surfaces, which is a challenging field of investigation.

  The phase-field technique can be applied to predict the morphology of the electrodeposits by employing a phase field variable (function of time and position) to describe the phase (liquid or solid) of a material at a certain location [168]. This variable takes two distinct values (for instant +1 and -1) in each of the phases. The smooth changes in these values at a location describes the interface between the two phases. In contrast, the level-set method can be applied to track the electrode-electrolyte interface location and shape and the spatially varying concentration profiles of the different components in the electrolyte by employing a scalar variable (function of time and position), which is continuous, smooth and monotonic in the direction normal to the interface [169]. The zero level set defines the position of the interface.

8 Appendices

8.1 Appendix A

Parameter Values Used in the Simulations

Symbol	Quantity	Size
h	Electrode height	10 cm
L_t	Carbon electrode thickness	4 mm
L_w	Carbon electrode width	10 cm
L_m	Membrane thickness	180 μm
L_c	Current collector thickness	6 mm
ϵ	Carbon electrode porosity	$^{\dagger}0.68$
d_f	Carbon electrode fibre diameter	172 μm [163]
d_g	Oxygen gas bubble diameter	50 μm
V_T	Electrolyte volume (half cell)	250 mL
a	Specific surface area: electrode	$^{\P}3 \times 10^6$ m^{-1}

Table 6: Default values of the constants related to structure. (†Measured, ¶Estimated).

Symbol	Quantity	Value
T_{ref}	reference temperature	25 ^{o}C
c_3^0	V(III) concentration at inlet	1053 mol m^{-3}
c_2^0	V(II) concentration at inlet	27 mol m^{-3}
c_4^0	V(IV) concentration at inlet	1053 mol m^{-3}
c_5^0	V(V) concentration at inlet	27 mol m^{-3}
c_d^0	Water concentration at inlets	4.2×10^3 mol m^{-3}
$p_{\text{out},c}$	Negative Electrode outlet pressure	300 kPa
$p_{\text{out},a}$	Positive Electrode outlet pressure	300 kPa
ω_c	Negative Electrode volumetric flow rate	1 mL s^{-1}
ω_a	Positive Electrode volumetric flow rate	1 mL s^{-1}
I_{app}	Applied current	10 A

Table 7: Default initial and boundary values.

Symbol	Quantity	Size
$k_{\mathrm{ref},1}$	Standard rate constant: reaction (1)	3×10^{-9} m s^{-1} [34]
$k_{\mathrm{ref},2}$	Standard rate constant: reaction (2)	1.75×10^{-7} m s^{-1} [37]
$j_{0,(\mathrm{O_2,ref})}$	Oxygen evolution exchange current density	$^{\ddagger}1 \times 10^{-9}$ A m^{-2}
$j_{0,\mathrm{H_2}}$	Hydrogen evolution exchange current density	$^{\ddagger}1.4 \times 10^{-9}$ A m^{-2}
$\alpha_{c,+}$	Cathodic transfer coefficient: reaction (1)	$^{\S}0.5$
$\alpha_{c,-}$	Cathodic transfer coefficient: reaction (2)	$^{\S}0.5$
$\alpha_{a,+}$	Anodic transfer coefficient: reaction (1)	$^{\S}0.5$
$\alpha_{a,-}$	Anodic transfer coefficient: reaction (2)	$^{\S}0.5$
$\alpha_{\mathrm{O_2}}$	Transfer coefficient: reaction (3)	0.3 [35]
$\alpha_{\mathrm{H_2}}$	Transfer coefficient: reaction (4)	0.35 [36]
$E'_{0,+}$	Formal potential: V(IV)/V(V)	1.004 V *vs.* SHE [170]
$E'_{0,-}$	Formal potential: V(II)/V(III)	-0.255 V *vs.* SHE [170]
$E'_{\mathrm{O_2}}$	Formal potential: $\mathrm{H_2O/O_2}$	1.23 V *vs.* SHE [170]
c_f	Fixed charge site (sulfonate) concentration	1200 mol m^{-3} [99]
z_f	Charge of fixed (sulfonate) sites	-1

Table 8: Default values of the constants related to electrochemistry. (‡Fitted parameter, §Assumed value).

Symbol	Quantity	Size
D_2	V(II) diffusion coefficient in electrolyte	2.4×10^{-10} m^2 s^{-1} [164]
D_3	V(III) diffusion coefficient in electrolyte	2.4×10^{-10} m^2 s^{-1} [164]
D_4	V(IV) diffusion coefficient in electrolyte	3.9×10^{-10} m^2 s^{-1} [164]
D_5	V(V) diffusion coefficient in electrolyte	3.9×10^{-10} m^2 s^{-1} [164]
D_{H_2O}	Water diffusion coefficient in electrolyte	2.3×10^{-9} m^2 s^{-1} [171]
D_w	Water diffusion coefficient in the membrane	5.75×10^{-10} m^2 s^{-1} [98]
D_{H^+}	Proton diffusion coefficient in the membrane	1.4×10^{-9} m^2 s^{-1} [172]
$D_{HSO_4^-}$	HSO_4^- diffusion coefficient in the membrane	1.4×10^{-9} m^2 s^{-1} [173]
$D_{SO_4^{2-}}$	SO_4^{2-}diffusion coefficient in the membrane	1.4×10^{-9} m^2 s^{-1} [173]
K	Kozeny-Carman constant: porous electrode	5.55 [174]
κ_ϕ	Electrokinetic permeability: membrane	1.13×10^{-19} m^2 [172]
κ_p	Hydraulic permeability: membrane	1.58×10^{-18} m^2 [175]
μ_{H_2O}	Water viscosity	10^{-3} Pa s
σ_f	Electronic conductivity of carbon porous electrode	363 S m^{-1}
σ_{coll}	Electronic conductivity of current collectors	†1000 S m^{-1}

Table 9: Default values for constants related to the transport of charge and mass. (†Estimated)

Symbol	Quantity	Size
λ_l	Electrolyte thermal conductivity	0.67 W m^{-1} K^{-1}
λ_{elec}	Electrode thermal conductivity	0.15 W m^{-1} K^{-1}
λ_{mem}	Membrane thermal conductivity [176]	0.67 W m^{-1} K^{-1}
λ_{coll}	Current collector thermal conductivity	16 W m^{-1} K^{-1}
λ_{air}	Thermal conductivity of air at 293 K	0.0257 W m^{-1} K^{-1}
$\rho_l C_l$	Liquid thermal capacitance (water)	4.187×10^6 J m^{-3} K^{-1}
$\rho_{\text{elec}} C_{\text{elec}}$	Porous electrode thermal capacitance‡	3.33×10^5 J m^{-3} K^{-1}
$\rho_{\text{mem}} C_{\text{mem}}$	Membrane thermal capacitance†	2.18×10^6 J m^{-3} K^{-1}
$\rho_{\text{coll}} C_{\text{coll}}$	Current collector thermal capacitance	4.03×10^6J m^{-3} K^{-1}
$-\Delta S_1$	Entropy associated with reaction (1) [177]	-21.65 J mol^{-1} K^{-1}
$-\Delta S_2$	Entropy associated with reaction (2) [177]	-100 J mol^{-1} K^{-1}
$-\Delta S_3$	Entropy associated with reaction (3) [177]	-65.25 J mol^{-1} K^{-1}

Table 10: Default parameter values for the heat equation (91).

†Estimate based on a specific heat capacity for water and a typical dry density of Nafion®, 1500 kg m^{-3}.

‡Estimate based on a specific heat capacity for graphite of 710 J kg K^{-1} and a Sigratherm® GFA5 density of 469 kg m^{-3} (68% porous).

Species	ΔH_f^0 / kJ mol^{-1}	ΔG_r^0 / kJ mol^{-1}	ΔS_f^0 / J mol^{-1} K^{-1}
V(II)	-226	-218	-130
V(III)	-259	-251.3	-230
V(IV)	-486.6	-446.4	-133.9
V(V)	-649.8	-587	-42.3
H_2O	-285.8	-237.2	69.95
O_2	0	0	205.152
H_2	0	0	130.68
H^+	0	0	0

Table 11: Standard thermodynamic values of the aqueous species involved in the VRB reaction at 25^{o}C [177].

8.2 Appendix B

Publications

1. H. Al-Fetlawi, A.A. Shah, F.C. Walsh, "Non-Isothermal Modelling of the All-Vanadium Redox Flow Battery", *Electrochim. Acta*, vol. (55) issue (1) pp. 78−89 (2009).

2. A.A. Shah, H. Al-Fetlawi, F.C. Walsh, "Dynamic Modelling of Hydrogen Evolution Effects in the All-vanadium Redox Flow Battery", *Electrochim. Acta*, vol. (55) issue (3) pp. 1125−1139 (2010).

3. H. Al-Fetlawi, A.A. Shah, F.C. Walsh, "Modelling the effects of Oxygen Evolution in the All-vanadium Redox Flow Battery", *Electrochim. Acta*, vol. (55) issue (9) pp. 3192−3205 (2010).

4. H. Al-Fetlawi, A.A. Shah, F.C. Walsh, "A Dynamic Modelling of the All-vanadium Redox Flow Battery", In, *The 217th ECS Meeting, Vancouver, Canada*, April 25−30, 2010, B3−00890.

5. H. Al-Fetlawi, A.A. Shah, F.C. Walsh, "Modelling All-Vanadium Redox Flow Battery", In, *61st Annual Meeting of the International Society of Electrochemistry,Nice, France*,September 26th - October 1st, 2010, s04−P-001.

6. R. Tangirala, M.J. Watt-Smith, H. Al-Fetlawi, P. Ridley, R.G.A. Wills, A.A. Shah, F.C. Walsh, " The effects of mass transfer on the performance of Vanadium Redox Flow Battery", *J. Electrochem. Soc.*, in preparation.

References

[1] A. Ter gazarian, *Energy Storage For Power Systems*, The Institution Of Engineering And Technology (1994).

[2] D. Linden, T. B. Reddy, *Handbook Of Batteries*, 3rd Edition, McGraw-Hill, New York (2002).

[3] A. Schneuwly, R. Gallay, *Properties and applications of supercapacitors from the state-of-the-art to future trends, PCIM* (2000).

[4] B.Destraz, P. Barrade, A. Rufer, *Supercapacitive energy storage for diesel-electric locomotives*, In *Symposium on Power Electronics, Electrical Drives, Automation Motion, SPEEDAM* (2004).

[5] P.Barrade, A. Rufer, *The use of supercapacitors for energy storage in traction systems*, In *Vehicular Power and Propulsion Symposium, IEEE-VPP* (2004).

[6] L. Chen, Y. Liu, A. Arsoy, P. Ribeiro, M. Steurer, M. Iravani, *Detailed modeling of superconducting magnetic energy storage system, IEEE Transactions on Power Delivery* (2006).

[7] S. Lemofouet, A. Rufer, *Hybrid energy storage system based on compressed air and super capacitors with Maximum Efficiency Point Tracking*,In *International Power Electronics Conference, IPEC* (2005).

[8] A. Hiratsuka, T. Arai, T. Yoshimura, *Seawater pumped-storage power plant in Okinawa island, Japan*, *Engineering geology* **35** (1993) 237-246.

[9] M. MacCracken, *Thermal Energy Storage*, ASHRAE Journal, September (2003).

[10] UNIFLEX-PM, 019794 (SES6), *Advanced power converters for universal and flexible power management in future electricity network*, February, (2007).

[11] A. Gonzalez, B.Ó. Gallachóir, E. McKeogh, *Sustainable Energy Research Group, University College Cork, 2004, Final Report*, http://www.sei.ie, accessed on 30 March 2009.

[12] M. Bartolozzi, *J. Power Sources* **27** (1989) 219-234.

[13] J. Newman, K.E. Thomas-Alyea, *Electrochemical Systems*, 3ed, John Wiley Sons, Inc., Hoboken, New Jersey (2004).

[14] M. Bartolozzi, *J. Nucl. Sci. Tech.* **37** (2000) 253-256.

[15] L.H. Cutler, *E.I. du Pont de Nemours and Co.,US Patent* 3607420 (1969).

[16] J.T. Kummer, D.G. Oei, *J. Appl. Electrochem* **12** (1982) 87-100.

[17] M. Skyllas-Kazacos, C. Menictas, vanadium redox battery for emergency back-up applications, In *Proceedings, Intelec, Melbourne*, (1997).

[18] C. Ponce de Léon, A. Frías-Ferrer, J. González-Garcia, D.A. Szánto, F.C. Walsh, *J. Power Sources* **160** (2006) 716.

[19] *The VRB energy storage system: The multiple benefits of integrating the VRB-ESS with wind energy, Case studies in MWH applications, Technical report, VRB Power Systems Inc*, (2007).

[20] EESAT, *Proceeding International Conference, Electrical Energy Storage Systems Applications and Technologies*, $16^{th} - 18^{th} June(1998), Chester, UK$.

[21] R.E. White, C.W. Walton, H.S. Burney, R.N. Beaver, *J. Electrochem. Soc.* **133** (1986) 485.

[22] R.E.W. Jansson, R.J. Marshall, *Electrochim. Acta* **25** (1982) 823.

[23] P.A. Pissoort, *GB Patent* 2030349, (1978).

[24] A. Pellegri, P.M. Spaziante, *FR Patent* 754 065, (1933).

[25] M. Skyllas-Kazacos, R.G. Robins, *US Patent* 849 094, (1986).

[26] M. Rychcik, M. Skyllas-Kazacos, *J. Power Sources* **22** (1988) 59-67.

[27] E. Sum, M. Skyllas-Kazacos, *J. Power Sources* **16** (1985) 179.

[28] M. Skyllas-Kazacos, F. Grossmith, *J. Electrochem. Soc.* **134** (1987) 2950.

[29] A. Pellegri, P.M. Spaziante, *UK Patent* GB **2** 030 349 A (July 1978).

[30] I.M. Ritchie, O.T. Siira, *Redox Batteries- an Overview*,In *The 8th Biennial Congress of the International Solar Energy Society Proceedings* **3** (1983) 1732-1737.

[31] Sumitomo Electric Industries, Ltd., *Vanadium redox-flow battery VRB for a variety of applications*, http://www.electricitystorage.org, accessed July 12 (2008).

[32] *Winafrique energy solutions for tomorrow*, http://www.winafrique.com/, accessed July 14 (2010).

[33] E. Sum, M. Rychcik, M. Skyllas-Kazacos, *J. Power Sources* **15** (1985) 85-95.

[34] M. Gattrell, J. Park, B. MacDougall, J. Apte, S. McCarthy, C. W. Wu, *J. Electrochem. Soc* **151** (2004) 123.

[35] M.M. Saleh, M.H. El-Ankily, M.S. El-Deab, and B.E. El-Anadouli, *Bull. Chem. Soc. Jpn.* **79** (2006) 1711-1718.

[36] M.M. Saleh, *Solid State Electrochemistry* **11** (2007) 811-820.

[37] A.A. Shah, M.J. Watt-Smith, F.C. Walsh, *Electrochim. Acta* **53** (2008) 8087-8100.

[38] Izumi Tsuda, Ken Nozaki, Koichi Sakuta, Kosuke Kurokawa, *Improvement of Performance in Redox Flow Batteries for PV Systems*, *J. Solar Energy Materials and Solar Cells* **47** (1997) 101-107.

[39] N. Tokuda, T. Kanno, T. Hara, T. Shigematsu, Y. Tsutsui, A. Ikeuchi, T. Itou, T. Kumamoto, *Development of a Redox Flow Batter System*, *SEI Technical Review* **50** (2000) 88-94.

[40] M. Li, T. Hikihara, *IEICE Trans. Fundamentals* **E91-A(7)** (2008) 1741-1747.

[41] M. Vynnycky, *Energy* **55** (2010) 1-15.

[42] D.P. Scamman, G.W. Reade, E.P.L. Roberts, *J. Power Sources* **189** (2009) 1220-1230.

[43] D.P. Scamman, G.W. Reade, E.P.L. Roberts, *J. Power Sources* **189** (2009) 1231-1239.

[44] D. Pletcher, *A First Course in Electrode Processes* The Electrochemical Consultancy, Romsey, (1991).

[45] Frank C. Walsh, *A First Course in Electrochemical Engineering* The Electrochemical Consultancy, Romsey, (1993).

[46] A.J. Bard, L.R. Faulkner, *Electrochemical Methods*, second ed., John Wiley Sons, Inc., New York (2001).

[47] Steven S. Zumdahli, *Chemical Principles*, Fifth edition, Houghton Mifflin, New York, (2005).

[48] G.G. Botte, R.V. Subramanian, R.E. White, *Electrochim. Acta* **45** (2000), 2595-2609.

[49] T. Doherty, J.G. Sunderland, E.P.L. Roberts, D.J. Pickett, *Electrochim. Acta* **12** (1996), 519-526.

[50] J. Heikonen, T. Noponen, M. Lampinen, *J. Power Sources* **62** (1996) 27-39.

[51] A. Lasia, *Journal of Electroanalytical Chemistry* **428** (1997) 155-164.

[52] C.J. van Duijn, J.D. Fehribach, *Electronic Journal of Differential Equations* **6** (1993) 125.

[53] V.S. Bogotsky, *Fundamentals of Electrochemistry*,Wiley-Interscience, 2nd Edition (December 2005).

[54] P. Delahay, *Double layer and electrode kinetics*, second ed., John Wiley Sons, Inc., New York, (1965).

[55] G.W. Corder, *Virginia Journal of Science Education* **1** (2008) 33-36.

[56] T.F. Fuller, M. Doyle, J. Newman, *J. Electrochem. Soc.* **141** (1994) 1-10.

[57] D. Fan, R. White, *J. Electrochem. Soc.* **138** (1991) 17-25.

[58] C.Y. Mak, H.Y. Cheh, G.S. Kelsey, P. Chalilpoyil, *J. Electrochem. Soc.* **138** (1991) 1607.

[59] N. Harb, R.M LaFollette, *J. Electrochem. Soc.* **146** (1999) 809.

[60] C.Y. Wang , W.B. Gu, B.Y. Liaw, *J. Electrochem. Soc.* **145** (1998) 3407-3417.

[61] W.B. Gu, C.Y. Wang, B.Y. Liaw, *J. Electrochem. Soc.* **145** (1998) 3418-3427.

[62] W.B. Gu, C.Y. Wang, S.M.Li, M.M.Geng, B.Y. Liaw, *Electrochim. Acta* **44** (1999) 4525-4541.

[63] W.B. Gu, C.Y. Wang, *J. Electrochem. Soc.* **147** (2000) 2910-2922.

[64] M. Doyle, T.F. Fuller, J. Newman, *J. Electrochem. Soc.* **140** (1993) 1526-1533.

[65] M. Doyle, J.P. Meyers, J. Newman, *J. Electrochem. Soc.* **147** (2000) 99-110.

[66] P.M. Gomadam, J.W. Weidner, R.A. Dougal, R.E. White, *J. Power Sources* **110** (2002) 267-284.

[67] Gi Heon Kim, A. Pesaran, R. Spotnitz, *J. Power Sources* **170** (2007) 476-489.

[68] C.W. Tobias, R. Wijsman, *ibid.* **100** (1953) 459.

[69] J. Newman, W.H. Tiedemann, *AIChE J* **21** (1975) 25-41.

[70] W.H. Tiedemann, J. Newman, *in Battery Design and Optimisation.* The Electrochemical Society Softbound Proceeding Series Pennington, NJ (1979).

[71] D.M. Bernardi, H. Gu, A.Y. Schoene, *J. Electrochem. Soc.* **140** (1993) 2250-2258.

[72] W.B. Gu, C.Y. Wang, B.Y. Liaw, *J. Electrochem. Soc.* **144** (1997) 2053-2061.

[73] W.B. Gu, G.Q. Wang, C.Y. Wang, *in Proc. 16th Annual Battery Conf. on Application and Advantages* (2001) 181-186.

[74] W.B. Gu, G.Q. Wang, C.Y. Wang, *J. Power Sources* **108** (2002) 174-184.

[75] H. Gu, T.V. Nguyen, R.E. White, *J. Electrochem. Soc.* **134** (1987) 2953-2960.

[76] E.C. Dimpault-Darcy, T.V. Nguyen, R.E. White, *J. Electrochem. Soc.* **135** (1988) 278-285.

[77] D. Simonsson, P. Ekdunge, M. Lindgren, *J. Electrochem. Soc.* **135** (1988) 1613-1618.

[78] P. Ekdunge, D. Simonsson, *J. Applied Electrochemistry* **19** (1989) 127-135.

[79] P. Ekdunge, D. Simonsson, *J. Applied Electrochemistry* **19** (1989) 136-141.

[80] J. Landfors, D. Simonsson, A. Sokirko, *J. Power Sources* **55** (1995) 217-230.

[81] B.Y. Liaw, K. Bethune, In *Proc. 16th Annual Battery Conf. on Application and Advantages* (2001) 187-192.

[82] D.M. Bernardi, M. K. Carpenter, *J. Electrochem. Soc.* **142** (1995) 2631-2642.

[83] J. Newman, W.H. Tiedemann, *J. Electrochem.Soc.* **144** (1997) 3081-3091.

[84] H. Huang, T.V. Ngyen, *J. Electrochem. Soc.* **144** (1997) 2062-2068.

[85] J.N. Harb, V.H. Johnson, D. Rausen, In *Annual Electrochemical Society Conference*, Seattle, Washington, (1999).

[86] V. Boovaragavan, R.N. Methakar, V. Ramadesigan, V.R. Subramanian, *J. Electrochem. Soc.* **156** (2009) A854-A862.

[87] J.A. Trainham, J. Newman, *Electrochim. Acta* **26** (1981) 455-469.

[88] P.S. Fedkiw, R.W. Watts, *J. Electrochem. Soc.* **131** (1984) 701-709.

[89] T.I. Evans, R.E. White, *J. Electrochem. Soc.* **134** (1987) 866-874.

[90] T.I. Evans, R.E. White, *J. Electrochem. Soc.* **134** (1987) 2725-2733.

[91] G.D. Simpson, R.E. White, *J. Electrochem. Soc.* **136** (1989) 2137-2144.

[92] G.D. Simpson, R.E. White, *J. Electrochem. Soc.* **137** (1990) 1843-1846.

[93] M. Li, T. Hikihara, *IEICE Trans. Fundamentals* **E91-A** (2008) 1741-1747.

[94] D. You, H. Zhang, J. Chen, *Electrochim. Acta* **54** (2009) 6827-6836.

[95] H. Al-Fetlawi, A.A. Shah, F.C. Walsh, *Electrochim. Acta* **55** (2009) 78-89.

[96] A.A. Shah, H. Al-Fetlawi, F.C. Walsh, *Electrochim. Acta* **55** (2010) 1125-1139.

[97] H. Al-Fetlawi, A.A. Shah, F.C. Walsh, *Electrochim. Acta* **55** (2010) 3192-3205.

[98] T.E. Springer, T.A. Zawodinski, S. Gottesfeld, *J. Electrochem. Soc.* **138** (1991) 2334-2342.

[99] D.M. Bernadi, M.W. Verbrugge, *AIChE Journal* **37** (1991) 1151-1163.

[100] D.M. Bernadi, M.W. Verbrugge, *J. Electrochem. Soc.* **139** (1992) 2477-2490.

[101] T.F. Fuller, J. Newman, *J. Electrochem. Soc.* **140** (1993) 1218-1225.

[102] Z.H. Wang, C.Y. Wang, K.S. Chen, *J. Power Sources* **94** (2001) 40-50.

[103] A.Z. Weber, J. Newman, *Chem. Rev.* **104** (2004) 4679-4726.

[104] C-Y. Wang, *Chem. Rev.* **104** (2004) 4727-4766.

[105] A.A. Shah, K.H. Luo, T.R. Ralph, F.C. Walsh, *Electrochim. Acta*, doi:10.1016/j.electacta.2010.10.046.

[106] R. Schlögl, *Z. Phys. Chem.* (Frankfurt) **5** (1955) 372.

[107] J. Appelbaum, J. Farrell, J. Du, M. Barth, *in Proc. IEEE INTELEC82*, Washington DC, USA, (1982) 304-307.

[108] Z.M. Salameh, M.A. Casacca, W.A. Lynch, *IEEE Transactions of Energy Conversion* **7** (1992) 93-98.

[109] J.P. Cun, J.N. Fiorina, M. Fraisse, H. Mabouxx, *MGE UPS Systems, Grenoble, France*, Available online: http://www- merlin-gerin.eunet.fr/news/techpap/tp02us.ht.

[110] D. Sutanto, H.L. Chang, *IEEE Trans. on Energy Conversion* **4** (1995).

[111] J.R. Miller, *in Proc. IEEE INTELEC99* (1999) 107-109.

[112] S. Pang, *in Proc. of the American Control Conference*, (2001) 1644-1649.

[113] P.R. Pathapati, X. Xue, J. Tang, *Renew. Energy* **30** (2005) 1.

[114] D. Berndt, R. Brutigam, U. Teutsch, *in Proc. IEEE INTELEC95* (1995) 1-12.

[115] D. Berndt, *Maintenance-Free Batteries*, Research Studies Press Ltd., John Wiley Sons Inc. (1997).

[116] D. Berndt, W.E.N Jones, *in Proc. IEEE INTELEC98* (1998) 443-451.

[117] D. Berndt, *J. Power Sources* **95** (2001) 2-12.

[118] D. Berndt, *J. Power Sources* **100** (2001) 29-46.

[119] R.C. Kroeze, P.T. Krein, *in Proc. IEEE INTELEC08* (2008) 1336-1342.

[120] B. Gou, W.K. Na, B. Diong, *Fuel cells: modelling, control and applications*, Taylor Francis, Florida. (2010).

[121] M.Y. Christi, *Airlift Bioreactors, Elsevier Science Publications* (1989).

[122] L.J.J. Janssen, J.G. Hoogland, *Electrochim. Acta* **15** (1970) 1013-1023.

[123] F. Hine, M. Yasuda, R. Nakamura, T. Noda, *J. Elecrochem. Soc.* **122** (1975) 1185-1190.

[124] F. Hine, K. Murakami, *J. Elecrochem. Soc.* **127** (1980) 292-297.

[125] H. Vogt, *Electrochim. Acta* **25** (1980) 527-531.

[126] D. Ziegler, J.W. Evans, *J. Electrochem. Soc.* **103** (1986) 567-576.

[127] H. Vogt, *J. Electrochem. Soc.* **137** (1990) 1179-1184.

[128] P. Boissonneau, P. Byrne, *J. Appl. Electrochem.* **30** (2000) 767-775.

[129] A.A. Dahlkild, *J. Fluid Mech.* **428** (2001) 249-272.

[130] R. Wedin, A.A. Dahlkild, *Ind. Eng. Chem. Res.* **40** (2001) 5228-5233.

[131] M.D. Mat, K. Aldas, *Int. J. Hydrogen Energy* **30** (2005) 411-420.

[132] M. Ishii, N. Zuber, *AIChE J* **25** (1979) 834-855.

[133] M. Manninen, V. Taivassalo, S. Kallio, *On the mixture model for multiphase flow*, Technical Report, VTT Pulications 288, Technical Research Centre of Finland (1996).

[134] C. Fabjan, J. Garche, B. Harrer, L. Jőrissen, C. Kolbeck, F. Philippi, G. Tomazic, F. Wagner, *Electrochim. Acta* **47** (2001) 825.

[135] L.J.J. Janssen, *Electrochim. Acta* **23** (1978) 81-86.

[136] G. Marrucci and L. Nicodemo, *Chem. Eng. Sci.* **22** (1967) 1257.

[137] G. Ahmadi, D. Ma, *Int. J. Multiphase Flow* **16** (1990) 323-340.

[138] D.A. Drew, *Ann. Rev. Fluid Mech.* **15** (1980) 261-291.

[139] J.O. Hirschfelder, C.F. Curtiss, R.B. Bird, *Molecular Theory of Gases and Liquids*, Wiley, New York (1954).

[140] R.A. Freeze, J.A. Cherry, *Groundwater*, Prentice-Hall, New Jersey (1979).

[141] C. Crowe, M. Sommerfeld, Y. Tsuji, *Multiphase Flows with Particles and Droplets*, CRC Press, Boca Raton, FL (1998).

[142] R. Clift, J.R. Grace, M.E. Weber, *Bubbles, Drops and Particles*, Academic Press, London (1978).

[143] R.F. Probstein, *Physicochemical Hydrodynamics.* Butterworth Publishers, MA, 1989.

[144] B. Bird, W. Stewart, E. Lightfoot, *Transport Phenomena*, John Wiley and Sons, NY (second ed.) (2002).

[145] A.A. Shah, P.C. Sui, G.S. Kim, S. Ye, *J. Power Sources* **166** (2007) 1.

[146] A.A. Shah, F.C. Walsh, *J. Power Sources* **185** (2008) 287.

[147] A.A. Shah, T.R. Ralph, F.C. Walsh, *J. Electrochem. Soc.* **156** (2009) B465.

[148] A.A. Shah, G.S. Kim, P.C. Sui, D. Harvey, *J. Power Sources* **163** (2007) 793.

[149] S. Church, *The New Journal*, (January 2006) P.B7.

[150] C. Heitner-Wirguin, *J. Membrane Sciences* **120** (1996) 1-3.

[151] K.A. Mauritz, R.B. Moore, *Chemical Reviews* **104** (2004) 4535-4585.

[152] D.J. Connolly, Longwood, W.F. Gresham, *US Patent* 3,282,875 (1966).

[153] M. Schuster, M. Ise, A. Fuchs, K.D. Kreuer, J. Maier, *Germany:Max-Planck Institute fur Festkorpperforschung n.d* (2005).

[154] G. Gelbard, *Industrial Engineering Chemistry Research* **44** (2005) 8468-8498.

[155] S. Paddison, *J. New Mater. Electrochem. Syst.* **4** (2001).

[156] R. Jinnouchi, K. Okazakik, *Microscale Thermodynamics Eng.* **7** (2001).

[157] S. Koter, *J. Membrane Science* **206** (2002).

[158] A.Z. Weber, J. Newman, *J. Electrochem. Soc.* **151** (2004) A311-A325.

[159] S.G. Bratsch, *J. Phys. Chem. Ref. Data* **18** (1989) 1.

[160] I. Rubenstein, *Physical Electrochemistry.* Marcel Dekker, (1995).

[161] J. González-Garciá, P. Bonete, E. Expósito, V. Montiel, A. Aldaz, R. Torregrosa-Maciá, *J. Mater. Chem.* **9** (1999) 419-426.

[162] N. Vatistas, P.F. Marconi, M. Bartolozzi, *Electrochim. Acta* **36** (1991) 339-343.

[163] R. Carta, S. Palmas, A.M. Polcaro, G. Tola, *J. Appl. Electrochem.* **21** (1991) 793-798.

[164] T. Yamamura, M. Watanabe, T. Yano, Y. Shiokawa, *J. Electrochem. Soc.* **152** (2005) A830.

[165] S. Motupally, A.J. Becker, J.W. Weidner, *J. Electrochem. Soc.* **147** (2000) A3171-A3177.

[166] J. Healy, C. Hayden, T. Xie, K. Olson, R. Waldo, M. Brundage, H. Gasteiger, J. Abbot, *Fuel Cells* **5** (2005) 302.

[167] A.B. LaConti, M. Hamdan, R.C. McDonald, *Mechanisms of chemical degradation (polymer electrolyte membrane fuel cells and systems, PEMFC)*' In *A. Lamm W. Vielstich and H. Gasteiger, editors, Handbook of Fuel Cells - Fundamentals, Technology and Applications*, volume 3: pp. 647-662. John Wiley & Sons Inc., (2003).

[168] G.B. McFadden, A. A. Wheeler, D. M. Anderson, *Physica* **D144** (2000) 154-168.

[169] J.A. Sethian, *Cambridge University Press.* ISBN 0-521-64557-3 (1999).

[170] M. Pourbaix, *Atlas of Electrochemical Equilibria in Aqueous Solutions (Second ed.)*, *NACE International, Houston*, (1974).

[171] R. Mills, *Phys. Chem.* **77** (1973) 685.

[172] M.W. Verbrugge, F. Hill, *J. Electrochem. Soc.* **137** (1990) 886.

[173] G.E. Zaikov, A.P. Iordanskii, S. Markin, *Diffusion of Electrolytes in Polymers.* VSP, Utrecht, Netherlands, (1988).

[174] J.C. Brown, *Tappi Journal* **33** (1950) 130.

[175] J.L. Fales, E. Vandeborough, *Electrochem. Soc. Proceedings* **86** (1986) 179.

[176] C. Ziegler, A. Schmitz, M. Tranitz, E. Fontes, O. Schumacher, *J. Electrochem. Soc.* **151** (2004) A2028.

[177] A. Bard, R. Parsons, J. Jordan, *Standard Potentials in Aqueous Solution*, Marcel Dekker, New York, (1985).